UNVERSITY OF CAPE COAST

SPECTROSCOPIC STUDIES OF SOME SELECTED ANTI-MALARIAL HERBAL PLANTS SAMPLE COMBINED WITH MULTIVARIATE DATA ANALYSIS

CHARLES LLOYD YEBOAH AMUAH

2019

UNIVERSITY OF CAPE COAST

SPECTROSCOPIC STUDIES OF SOME SELECTED ANTI-MALARIAL HERBAL PLANTS SAMPLE COMBINED WITH MULTIVARIATE DATA ANALYSIS

BY

CHARLES LLOYD YEBOAH AMUAH

Thesis submitted to the Department of Physics of the School of Physical Sciences, College of Agriculture and Natural Sciences, University of Cape Coast, in partial fulfilment of the requirements for the award of Doctor of Philosophy Degree in Physics

JUNE 2020

DECLARATION

Candidate's Declaration

I hereby declare that this thesis is the result of my own original research and that no part of this has been presented for another degree in this university or elsewhere.

…… Date……..

Charles Lloyd Yeboah Amuah

(Candidate)

Supervisors' Declaration

We hereby declare that the preparation and presentation of this thesis we supervised in accordance with the guidelines on supervision of thesis laid down by the University of Cape Coast.

…….. Date……..

Prof. Moses Jojo Eghan

(Principal supervisor)

…… Date……

Dr. Benjamin Anderson

(Co-Supervisor)

ABSTRACT

Two spectroscopic techniques: Laser-Induced Fluorescence (LIF) and Attenuated Total Reflectance Fourier-Transform Infrared (ATR-FTIR) spectroscopy and soil analysis were used to study and classify Anti-Malarial Herbal plants (AMHPs) from four locations (Abrafo, Jukwa, Nfuom and Akotokyere) in the Cape Coast metropolis. Deconvoluted peaks from the LIF spectra of the AMHPs samples showed compounds such as berberine, quercetin, flavanols presents in all the AMHPs samples. Principal component analysis (PCA) showed the AMHPs samples were similar in chemical composition to each other. The classification results (CR) obtained from the PCA models of the LIF spectra was used to identify the AMHPs samples according to their locations. The CR for the training sets was 100.00 % for Support Vector Machine (SVM), 99.95 for K-Nearest Neighbour (KNN) and 99.23 % for Linear Discriminant Analysis (LDA). For verification sets SVM and KNN were 100.00 % respectively while LDA was 98.23 %. The ATR-FTIR spectra of the AMHPs samples were characterized by the O-H and N-H stretching vibrations (3200 cm^{-1}) as a result of carbohydrates and proteins while C-H stretching vibrations (3000 cm^{-1}) as a result of lipids and carbohydrates. Lipids membranes and cell wall pectin absorbed around 1732 cm^{-1}. Similarity analysis showed that the AMHPs samples were similar irrespective of their locations. Results from the soil analysis shows that soil properties from the four locations are similar and therefore confirms the results obtained from the two spectroscopic techniques.

KEY WORDS

Anti-Malarial Herbal Plants

Macronutrients

Metabolites

Micronutrients

Multivariate data analysis

Spectroscopic techniques

ACKNOWLEDGEMENTS

Firstly, I would like to acknowledge the tremendous assistance of Prof. Moses Jojo Eghan, my principle supervisor, who has been an inspiring source of encouragement throughout this entire research work. His tireless dedication and patience in reading every bit of this work has led to the achievement of this ultimate and perfect goal. My gratitude also goes to Dr. Benjamin Anderson, my co-supervisor, for his encouragement and reading thoroughly through this work.

I wish also to express my deep appreciation and gratitude to Dr. Samuel Sonko Sackey, the coordinator for Laser and Fibre Optics Centre (LAFOC) for his motivation, encouragements and support during this period in the work. My sincere thanks also go to the head, Prof. George Amoako and all the lecturers of the Departments of Physics for their contribution to the successful completion of this work.

I thank the Office of External Activities (OEA) of the International Centre for Theoretical Physics (ICTP), Italy, and the School of Graduate Studies (SGS), University of Cape Coast for the financial support and the International Science Programme (ISP) of Uppsala University, Sweden which provided equipment. I also thank Laser and Fibre Optics Centre (LAFOC) of the University of Cape Coast and all members of the African Spectral Imaging Network (AFSIN).

Finally, l would like to acknowledge my family members and friends for the love and support they shared with me during this period of work.

DEDICATION

This thesis is dedicated to my wife Mrs Lucy Amuah, my sons Nathan Nana Yeboah Amuah and Cyril Yaw Opong Amuah.

TABLE OF CONTENTS

LIST OF TABLES

LIST OF FIGURES

LIST OF PLATES

LIST OF ACRONYMS

A	Abrafo
AS	Absorption Spectroscopy
A-SS	Abrafo-Sub Soil
A-TS	Abrafo-Top Soil
AAS	Atomic Absorption Spectroscopy
AB	Alstonia Boonei De Wild
AH	Acanthospermum Hispidum DC
AI	Azadirachta Indica A. Juss
Ak	Akotokyere
Ak-SS	Akotokyere-Sub Soil
Ak-TS	Akotokyere-Top Soil
AMHPs	Anti-Malarial Herbal Plants
ATR	Attenuated Total Reflectance
ATR-FTIR	Attenuated Total Reflectance-Fourier Transform Infrared
CO	Cassia Occidentalis Linn
DOAS	Differential Optical Absorption Spectroscopy
DP	Depth of Penetration
DRIFTS	Diffuse Reflectance Fourier Transform Spectroscopy
EBT	Evichrom Black T
EM	Electromagnetic
FS	Fluorescence Spectroscopy
GASMAS	Gas in Scattering Media Absorption Spectroscopy
HCA	Hierarchical Clustering Analysis
IR	Infrared
J	Jukwa
J-SS	Jukwa-Sub Soil
J-TS	Jukwa – Top Soil
KNN	K-Nearest Neighbour
LDA	Linear Discriminant Analysis

LEDs	Light Emitting Diodes
LIDAR	Light Detection and Ranging
LIF	Laser-Induced Fluorescence
MATLAB	MATrix LABoratory
MI	Mangifera Indica Linn
ML	Morinda Pinnata Linn
N	Nfuom
NMRS	Nuclear Magnetic Resonance Spectroscopy
N-SS	Nfuom-Sub Soil
N-TS	Nfuom-Top Soil
PC1	Principal Component 1
PC2	Principal Component 2
PC3	Principal Component 3
PCA	Principal Component Analysis
PCCs	Principal Component Coefficients
PCs	Principal Components
pH	Potential of Hydrogen
PTFE	Polytetrafluoroethylene
RC	Ricinus Communis Linn
RS	Raman Spectroscopy
RV	Rauvolfia vomitoria Afz
SVM	Support Vector Machine
TDLAS	Tunable Diode Absorption Spectroscopy
TEA	Triethanolamine
UATR	Universal Attenuated Total Reflectance
USDA	United State Department of Agriculture
UV	Ultraviolet
UV-VIS	Ultraviolet-Visible Spectroscopy
VA	Vernonia Amygdalina Linn
WMS	Wavelength Modulation Spectroscopy

XES	X-Ray Emission Spectroscopy

CHAPTER ONE

INTRODUCTION

Background to the Study

Spectroscopy techniques are methods used for probing samples using electromagnetic radiation to obtain useful information out of the samples. These spectroscopic techniques require the use of excitation light sources from the optical regions, that is ultraviolent (UV), visible and infrared (IR) regions of the electromagnetic (EM) spectrum (figure 1) (Chalmers & Griffiths, 2002; Demtröder, 2013; Svanberg, 2012). The excitations from the optical region bring about electronic, vibrational and rotational transitions. Spectroscopic techniques tend to provide useful information from the sample under investigation. The fingerprints derived from the spectroscopic techniques allow for different molecular samples to be differentiated (Anderson, Buah-Bassuah, & Tetteh, 2004; Bashkatov, Genina, & Tuchin, 2011; Jacques & Pogue, 2008; Svanberg, 2012; Tuchin & Tuchin, 2007). Spectroscopic techniques involve the transfer of photons, which start with the measurement of reflection, transmission, absorption, scattering or fluorescence properties of the sample. These processes result in unearthing features such as the absorption coefficient, scattering coefficient, molecular compositions, and the crystal structure of the sample.

Spectroscopic techniques are promising multidisciplinary and valuable techniques applied in a wide range of research fields ranging from medicine, zoology, astronomy, food science, agriculture, etc, due to their unique characteristics such as non-invasiveness and non-destructiveness (Brydegaard, Haj-Hosseini, Wardell, & Andersson-Engels, 2011; Svanberg, 2012). They

provide cellular or molecular level information. They have been utilized as tools for environmental monitoring, air quality monitoring, water and vegetation assessment, as well as insect identification through remote sensing. Besides these techniques, they have been used remotely for quantifying agricultural and epidemiological importance (Anderson et al., 2004; Svanberg, 2012; Winefordner, 1994). They are used to identify and quantify compounds and complex mixtures. The usefulness of these techniques results from the characteristic and distinctive interaction of each sample with the EM radiation.

With respect to applications to spectroscopic techniques, instrumentations for Nuclear magnetic resonance spectroscopy (NMRS), X-ray emission spectroscopy (XES), Ultraviolet (UV)-visible (VIS) (UV-VIS) spectroscopy, Fourier transform-infrared (FT-IR) spectroscopy, Absorption spectroscopy (AS) and Raman spectroscopy (RS) represents some common measurement techniques for both atomic and molecular studies of samples. For instance, XES is a surface-sensitive technique that measures the elemental composition at part per thousand range. The XES spectra are obtained by irradiating the sample with X-rays and simultaneously measuring the kinetic energy of the sample being studied. FT-IR uses excitation from a lower frequency to provide vibrational information of molecules present within a sample (Chalmers & Griffiths, 2002; Colthup, 2012; Lord, 1965; Nakamoto, 2006; Pavia, Lampman, Kriz, & Vyvyan, 2014; Smith, 2011; Socrates, 2001; Stuart, 2005). To avoid interference from water, detection in the IR region requires that the sample preparation are done with either Potassium bromide (KBr) or Nujol oil (Moody & Harwood, 1989; Smith, 1998, 2011). RS technique is based on an inelastic scattering of monochromatic light source and

observing a change in the frequency of scattered light originating from the sample (Colthup, 2012; Lord, 1965; Raman & Krishnan, 1928). The inelastic scattered photons are observed as spectral peaks and based on the amplitude of these peaks the chemical composition of the sample can be identified (Lewis & Edwards, 2001; McCreery, 2005).

Absorption measurements can also be used to investigate the presence of molecular species having energies which are in resonance with the spectra line(s) of the radiation source (Bernath, 2015). Some examples of AS techniques include tunable diode laser absorption spectroscopy (TDLAS), differential optical absorption spectroscopy (DOAS), wavelength modulation spectroscopy (WMS), differential absorption light detection and ranging (LIDAR) and gas in scattering media absorption spectroscopy (GASMAS) (Platt & Stutz, 2008; Winefordner, 1994). Using WMS technique, even in the presence of large background, an implanted gas produces minute but thin signal that can be detected by the GASMAS (Sjöholm, Somesfalean, Alnis, Andersson-Engels, & Svanberg, 2001; Somesfalean et al., 2002). The GASMAS technique provides new opportunities for studying gases enclosed in their natural environment. This technique is useful for characterizing and quantifying of free gases in the scattering media.

Fluorescence spectroscopy (FS) is also a common technique in which emissions due to the absorption of a photon is studied (Sauer, Hofkens, & Enderlein, 2010). Fluorescence emission occurs as a result of an electronic transition of atoms and this occurs in the optical region of the EM spectrum. This method is appropriate for analysing molecules because of its sensitivity and specificity (Lakowicz, 2013; Lakowicz & Masters, 2008). Fluorescence

emission depends on the excitation wavelength. This makes FS a frequency dependent phenomenon. For a typical FS system, three basic elements are considered: a source, sample and a detector. The source of light can be lasers, light emitting diodes (LEDs) and lamps. These light sources have spectral output either as a continuum of energy over a wide range or series of discrete lines. Majority of the light sources in FS instrumentation lack stability over long periods. Currently, lasers are commonly used as sources in FS to overcome this challenge (Al-Salhi, Masilamani, Vijmasi, Al-Nachawati, & VijayaRaghavan, 2011; de Oliveira Silva et al., 2010; Kalnina et al., 2010; Masilamani et al., 2014).

A type of FS that uses a laser as an excitation source is called Laser-Induced Fluorescence (LIF). This process involves transitions between electronic and vibrational states of polyatomic molecules. Quantities such as fluorescent decay time, anisotropy, polarization conditions, quantum yields and stokes shifts which can be accessible for analysis, are also associated with the LIF. These parameters for the detection of samples allow alleviating some difficulties which may occur when applying LIF, in this case, other parameters may be used. However, there are substances which show extremely low fluorescence yield or even no fluorescence at all due to the fast decay pathways such as intersystem crossing. When using LIF, the characteristics such as high spectral intensity and well-defined wavelength of the lasers are specifically utilized. These allow for selective excitation of samples. By using LIF, it is possible to record both the excitation and emission spectra (Anderson et al., 2004; Barócsi et al., 2000; Gustafsson, Somesfalean, Alnis, & Svanberg, 2000).

LIF is a photon emission process that occurs during molecular relaxation from electronic excited states. In this process, the excitation source (laser) collide with the sample. The sample absorbs part of the incident light and the detector is used to record the emission (fluorescence from the sample). LIF has been applied several fields (Bazracharza, Rana, Roy, Tiwari, & Tripathi, 2015; Edner et al., 1992; Gouveia-Neto et al., 2011; Stewart et al., 2005; J. Yang et al., 2016).

Scope of the Study

This study aims at applying two (2) spectroscopic techniques: Laser-Induced Fluorescence (LIF) and Attenuated Total Reflectance-Fourier Transform Infrared (ATR-FTIR) spectroscopy to study and characterize/discriminate/identify Anti-Malarial Herbal Plants (AMHPs) from four locations (Abrafo, Jukwa, Nfuom and Akotokyere) in the Cape Coast metropolis. Also, the properties of the soil where the AMHPs samples were sampled in relation to the soil potential of hydrogen (pH), soil texture, primary, secondary and micro nutrients is studied.

Objectives

The objectives of this work were to determine the spectra fingerprint of the AMHPs samples using the two spectroscopic techniques: LIF and ATR-FTIR. Also, combine the LIF spectra fingerprint and multivariate analysis (Principal Component Analysis (PCA), Support Vector Machine (SVM), K-Nearest Neighbour (KNN) and Linear Discriminant Analysis (LDA)) to characterize, discriminate and identify the locations (Abrafo, Jukwa, Nfuom and

Akotokyere) of the AMHP samples. Moreover, the Phyto-constituents present within the AMHPs samples will be determined. Furthermore, the work seeks to determine the similarities of the AMHPs samples and their locations. Finally, the soil characteristics will be determined in relation to their locations collected.

Organization of the study

This thesis is organized into five main chapters. Chapter one gives an overview of the different spectroscopic techniques and its associated application to biological samples / medicinal plants (Anti-Malarial Herbal Plants, AMHPs). The scope of the work and the organization of the thesis is included within this chapter. Chapter two reviews the literature on spectroscopy with much emphasis on fluorescence and infrared spectroscopy. Also, Phyto/bioactive constituents found in medicinal plants are mentioned. Finally, the theory behind the multivariate data analysis is also mentioned. Chapter three is divided into three sections. The first section describes how the AMHPs samples were obtained and prepared for measurement. In the second section, two optical spectroscopic techniques, Laser-Induced Fluorescence (LIF) and Attenuated Total Reflectance-Fourier Transform Infrared (ATR-FTIR) applied to the AMHPs samples are described. The last section describes the procedures used in determining the primary, secondary and micro nutrients for each of the soil samples. Chapter four reports and discusses the results obtained from the two spectroscopic techniques and also presents the results and discussion on the potential of hydrogen (pH), the primary, secondary and micro nutrients of the soil samples. Finally, in chapter five, the summary of the work, the conclusions and relevant recommendations for future work are presented.

Chapter Summary

The chapter gave an overview of the different spectroscopic techniques and its associated application to biological samples / medicinal plants (Anti-Malarial Herbal Plants, AMHPs). The scope of the work and the organization of the study was included within the chapter.

CHAPTER TWO

LITERATURE REVIEW

Introduction

This chapter reviews the literature on spectroscopy with emphasis on fluorescence and infrared spectroscopy. The Phyto-constituents found in medicinal plants are outlined and finally the theories involved in the multivariate data analysis discussed.

Spectroscopy

The study of the interaction of light with matter is called spectroscopy (Gauglitz, Moore, & Vo-Dinh, 2014; Pavia et al., 2014). Several types of spectroscopy exist depending on the interaction of light with matter. The different collection of lights is grouped under what is called the electromagnetic (EM) spectrum (figure 1). The EM spectrum is a seemingly diverse collection of light energy, from the cosmic rays to X-rays to the visible light to the microwaves, each of which is considered as a wave or a particle traveling at the speed of light (Gauglitz et al., 2014; Pavia et al., 2014).

In considering light as a wave, the light beams are composed of both electric and magnetic waves which propagate in planes perpendicular to each other (Smith, 1998, 2011). This property is properly called electromagnetic radiation because it contains electric and magnetic waves. The light waves propagate through space in the direction defined by the line where the two planes containing the waves intersect.

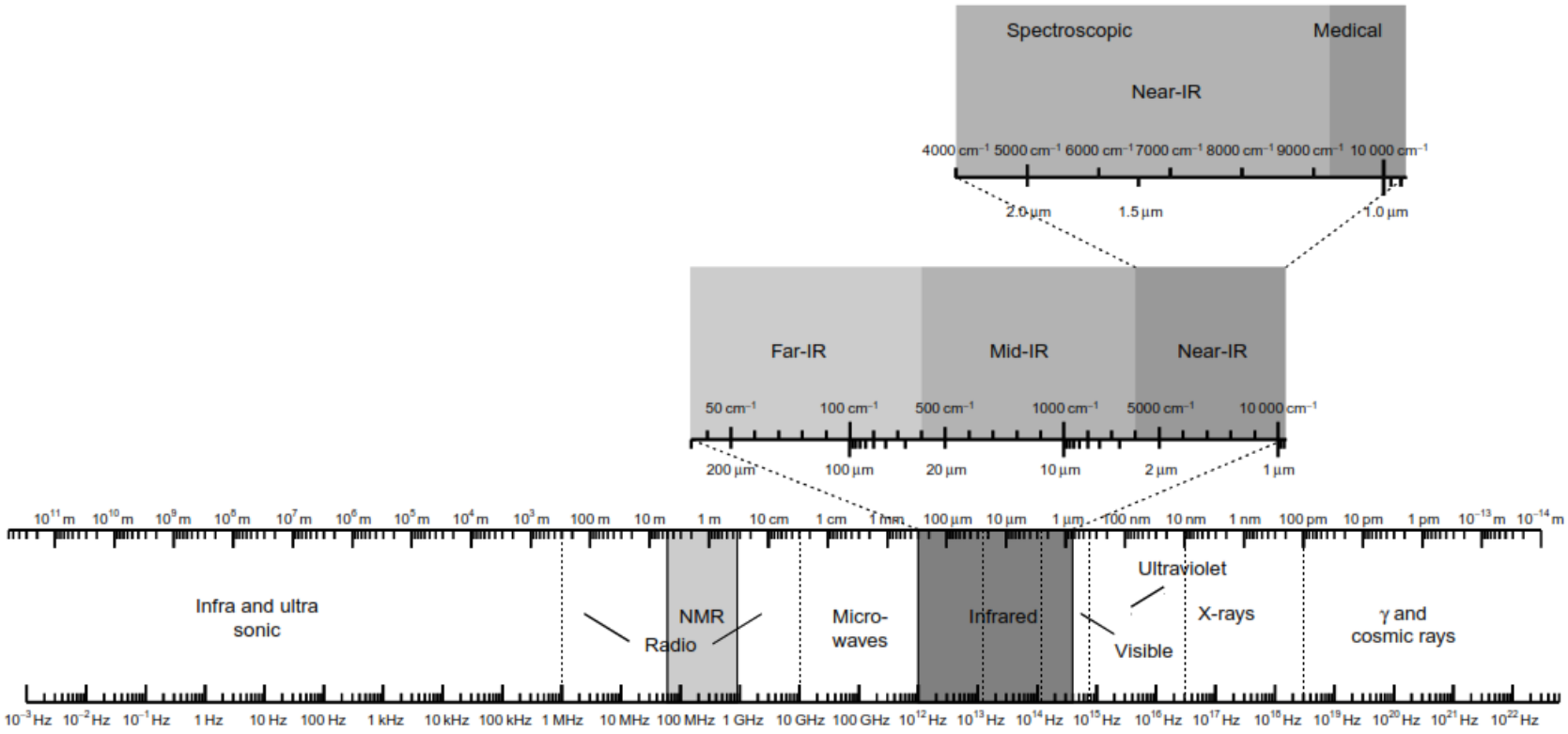

Figure 1: The Electromagnetic Spectrum showing Spectra ranges for Far, Mid and Near Infrared Regions (Chalmers & Griffiths, 2002)

It is the interaction of the electric wave vector with matter that give rise to absorbance phenomena (Smith, 1998, 2011). The electric vector amplitude changes with time and has a form of a sine wave as shown in figure 2.

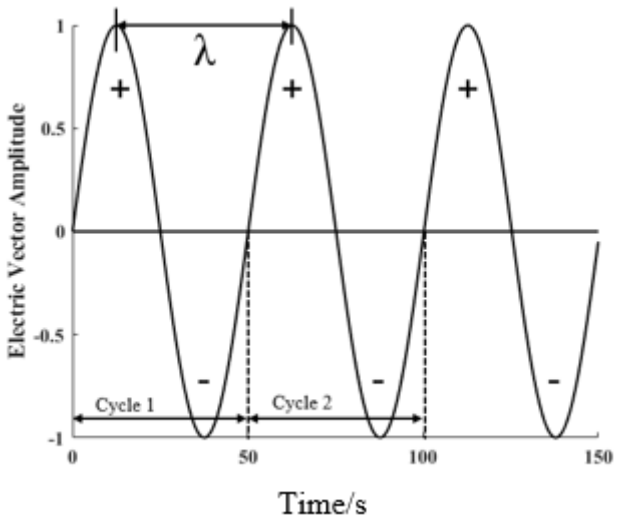

Figure 2: A Graph of Electric Vector Amplitude of a Light Wave against Time (Smith, 1998, 2011)

The properties that distinguishes different types of light are the wavelength, frequency, and wavenumber. The distance between two successive crests or troughs of a wave as seen in figure 2 is called wavelength which is denoted by the symbol λ. The frequency, denoted by nu (ν), equals the number of cycles a wave undergoes per second. Frequency is measured in cycles/s or Hertz (Hz). The frequency (ν), wavelength (λ), and the speed of light (*c*) beam are related to each other through equation 1.

$$c = \nu\lambda \tag{1}$$

This shows that the product of frequency and wavelength for a light wave is constant called the speed of light. The wavenumber is the reciprocal of the wavelength as shown in equation 2.

$$W = \frac{1}{\lambda} \tag{2}$$

If λ is measured in cm, then W is reported in cm^{-1} or reciprocal centimetres. A wavenumber measures the number of cycles in a light beam per unit length.

$$c = \frac{\nu}{W} \tag{3}$$

$$\nu = cW \tag{4}$$

Equations 3 and 4 shows that, light waves can be described by their frequency, wavelength, or wavenumber.

Light can also be thought of as a particle. A particle of light is known as a photon. Photons has no mass, but it has energy (E) as defined by equation 5. Equation 5 is known as the Planck-Einstein relation where h is the Planck's constant.

$$E = h\nu \tag{5}$$

Substituting equation 4 and 5, we obtain

$$E = hcW \tag{6}$$

Equation 6 shows that the photon energy also depend on the wavenumber. The higher the wavenumber the more the energy of the photon.

The waves differ from each other as illustrated from figure 1. The interaction of matter with X-Ray, ultraviolet (UV) and visible, infrared, microwave and radiofrequency form the basis for X-Ray spectroscopy, UV-visible spectroscopy, infrared spectroscopy, microwave spectroscopy, and

radiofrequency spectroscopy. The use of UV-visible light as a source can also be used for fluorescence spectroscopy. In this thesis, fluorescence and infrared spectroscopy technique is applied to study and characterized Anti-malarial Herbal Plants (AMHPs) samples.

X-Ray Spectroscopy

X-Ray spectroscopy is a technique that detect and measure photons and have its wavelength in the X-Ray portion of the electromagnetic spectrum (figure 1). When an atom is bombarded with high-energy particles, its electrons transition from one energy level to another. As the electrons adjust, the element absorbs and releases high-energy X-Ray photons in a way that is characteristic of the atom that make up that particular chemical element. X-Ray spectroscopy measures these changes in energy, which helps to identify elements and understand how the atoms within various materials interact (Bertuccio & Casiraghi, 2003; Hofmann, 2012; Van Grieken & Markowicz, 2001).

Microwave Spectroscopy

Microwave spectroscopy is the interaction of matter and electromagnetic radiation in the microwave region. The interaction of microwaves with matter is detected by observing the attenuation or phase shift of the microwave transition. Microwave spectroscopy has been used for the precision of spins and moments of inertia of nuclei. It has also contributed to the moment of inertia and the spin-rotation coupling mechanisms (Banwell & McCash, 1994; Townes & Schawlow, 2013).

Fluorescence Spectroscopy

The emission of light from any substance that occurs as a result of an electronically excited state is called luminescence. There are two (2) categories of luminescence: Fluorescence and phosphorescence. Fluorescence occurs in an excited singlet state where the electron in the excited orbital is paired to the second electron in the ground-state orbital. Phosphorescence, on the other hand, is the emission of light from the triplet excited states, in which the electron in the excited orbital has the same spin orientation as the ground-state electron. Transitions to the ground state are forbidden and the emission rates are low (10^3 or 10^0 s^{-1}). Hence phosphorescence lifetimes are typically in milliseconds or seconds. Longer lifetimes are possible, as seen from "glow-in-the-dark" toys (Lakowicz, 2013; Lakowicz & Masters, 2008).

Fluorescence normally occurs from aromatic organic molecules. An example of fluorescence material is quinine, which is present in tonic water. Fluorescence spectra is presented as an emission spectrum. The emission spectra is a graph of the fluorescence intensity versus wavelength (nanometres) or wavenumber (cm^{-1}). A typical fluorescence emission spectrum of a green leaf is shown in figure 3.

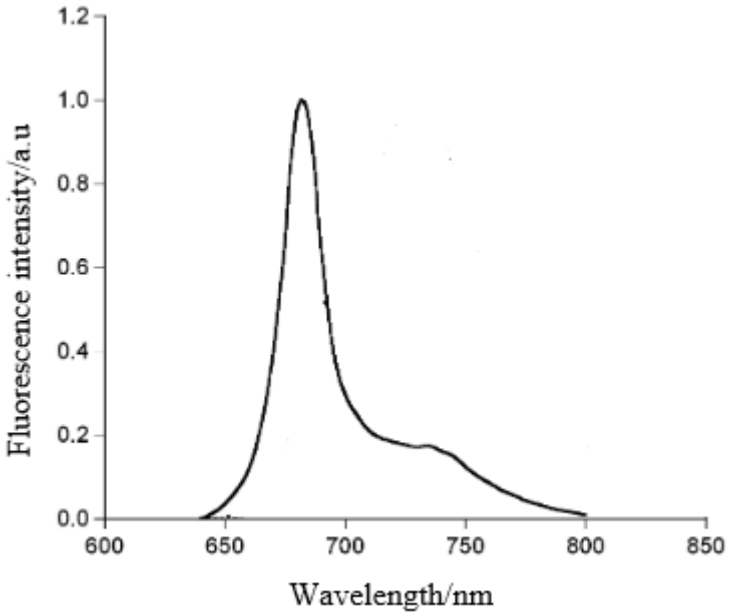

Figure 3: Fluorescence Emission Spectra of a Green Leaf

Fluorescence is better explained using the Jablonski diagram (figure 4). Figure 4 shows the singlet ground, first and second electronic states (energy levels) depicted by S_o, S_1 and S_2, respectively. For each of the electronic energy levels, a fluorophore can exist in a number of vibrational energy levels, depicted by 0, 1, 2, etc. The energy spacing between the various vibrational energy levels is illustrated by the emission spectrum of perylene (figure 5). The transitions between states are depicted as vertical lines which illustrate the instantaneous nature of light absorption. Molecules mostly occupy the lowest vibrational energy level of the ground electronic state at room temperature. In an event of light absorption, they are elevated to the excited states (figure 4). Since the energy is absorbed as discrete quanta, this results in distinct absorption bands. Having absorbed energy and reached one of the higher vibrational levels of an excited state, the molecule rapidly loses its excess vibrational energy by collision and falls to the lowest vibrational level of the excited state. In addition,

almost all molecules occupying an electronic state higher than the second, undergo internal conversion and pass from the lowest vibrational level of the upper state to a higher vibrational level of a lower excited state which has the same energy. From there, the molecules again lose energy until the lowest vibrational level of the first excited state is reached. From this level, the molecule returns to any of the vibrational levels of the ground state, emitting its energy in the form of fluorescence (Albani, 2007; Lakowicz, 1992, 2013; Svanberg, 1990, 2003).

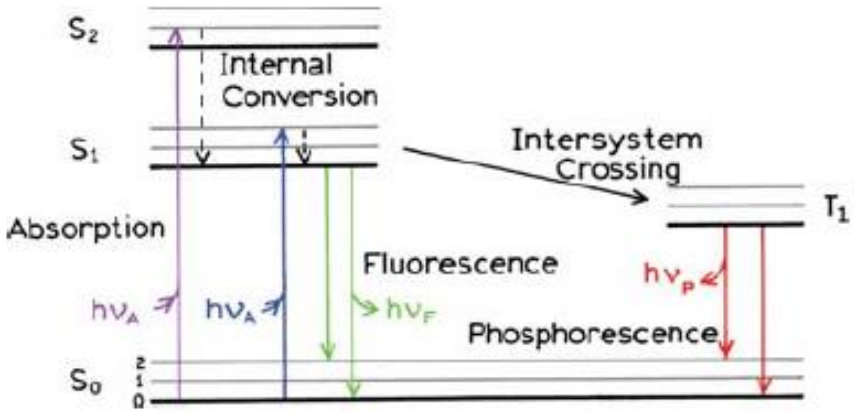

Figure 4: Jablonski Diagram Describing the Electronic Energy Levels or Organic Molecules. $h\nu_A$ is the Energy used in Absorption whereas $h\nu_F$ and $h\nu_P$ are the Energy released in Fluorescence and Phosphorescence (Lakowicz, 2013; Lakowicz & Masters, 2008)

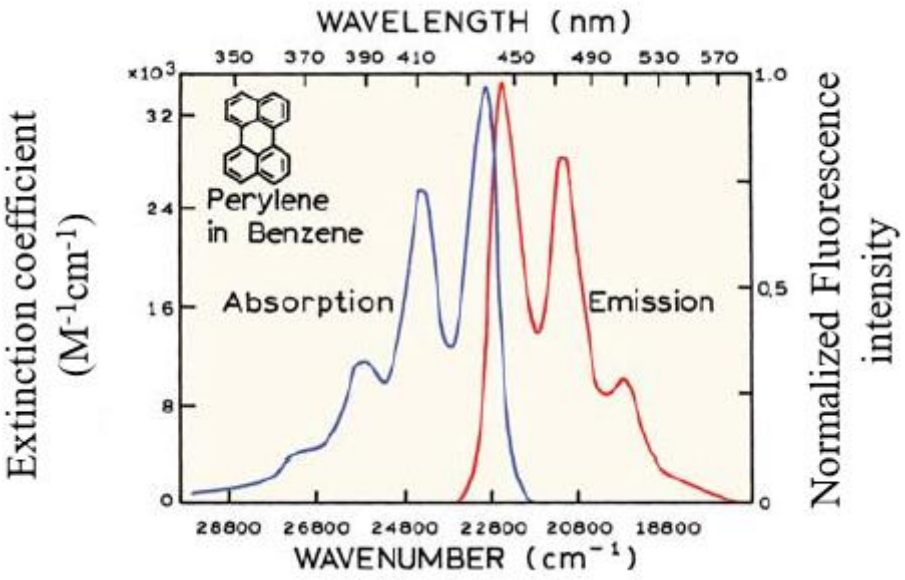

Figure 5: Absorption and Fluorescence Emission Spectra of Perylene

(Lakowicz, 2013; Lakowicz & Masters, 2008)

Laser-Induced Fluorescence (LIF)

Laser-Induced Fluorescence (LIF) is the fluorescence emission from atoms or molecules that have been excited to a higher energy level by the absorption of a laser radiation. In LIF technique, a laser is tuned to an allowed dipole transition from a ground state to a higher state of a fluorophore under consideration, and the fluorescence that is emitted during the decay is observed. Pulsed or continuous lasers can be used for both steady state and dynamic processes.

UV and visible lasers have been used in both laboratory and field fluorosensors or fluorometers (Svanberg, 2012). With the advent of diode lasers, these fluorosensors have become small and compact and have been used in several emerging areas such as environmental, agricultural, and medical (Anderson et al., 2004; Barócsi et al., 2000; Gustafsson et al., 2000; Lang et al.,

1995). Fluorometers using diode lasers have now become relatively inexpensive compared with the conventional ones, which use excitation sources like Nd: YAG lasers and nitrogen lasers. LIF measurements can either be performed by point measurements or in an imaging geometry. Point measurements involve the collection of spectroscopic information in a small fluorophore area, using an optical fibre to guide the excitation to the sample whilst in the imaging geometry, cameras are used to take snapshots of the sample under investigation.

Infrared Spectroscopy

The study of the interaction of infrared (IR) light with matter is called IR spectroscopy (Gauglitz et al., 2014; Pavia et al., 2014). IR spectroscopy is a versatile and useful technique used for quantitative and qualitative characterization of several types of materials in any form such as solids, liquids, or in the gaseous state (Gauglitz et al., 2014; Pavia et al., 2014). The IR region of the electromagnetic spectrum can be categorized into three (3) regions: near, mid, and far-IR (figure 1). An infrared spectrum is the fundamental measurement obtained in spectroscopy. This is a plot of measured intensity of light versus some property of light. An infrared spectrum can be obtained by passing an IR radiation through a sample, determining what fraction of the incident radiation is absorbed by that particular energy. This kind of spectroscopy can also be called absorption spectroscopy.

One way to think about how molecules absorb light is to consider the interaction as a collision between two particles. Consider photons of light and molecules as simple particles shaped like spheres. When two particles collide (molecules of billiard balls), three (3) different types of collision can occur

(Smith, 1998). There can be elastic collisions, inelastic collision and totally inelastic collision. Elastic collision is illustrated in figure 6. Before collision, the photon has energy $E = hcW$ and imagine the methane molecule has no kinetic or vibrational energy and therefore can be considered to be at rest.

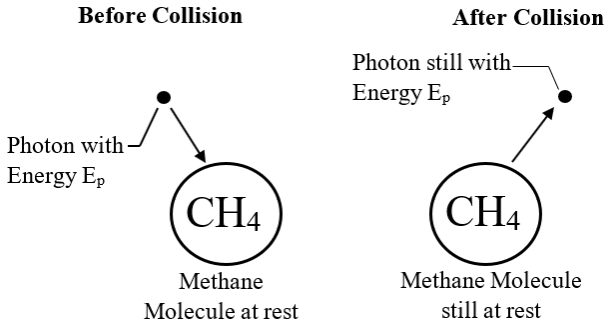

Figure 6: An Elastic Collision between a Photon and a Methane Molecule. E_p is the Energy of the Photon (Smith, 1998)

After collision, the photon still has energy hcW and the methane molecule is still at rest. The only thing that has changed is the direction of travel of the photon. Elastic collision between photons and molecules results in a phenomenon called Rayleigh scattering in which the direction but not the energy of the photon is changed. The intensity of Rayleigh scattering is proportional to the fourth power of the wavenumber of the photon, W, involved in the scattering. The second kind of collision that occurs is inelastic collision. In this type of collision, energy is exchanged between the particle and the molecule, and they leave the collision with different energy than before collision. In figure 7, before collision, the incoming photon has energy E_p, and the methane molecule is at rest. After collision, some of the photon's energy is deposited into the molecule as vibrational energy E_v. The photons energy after

collision is E_i. Inelastic collision between molecules and photons give rise to a phenomenon called Raman scattering.

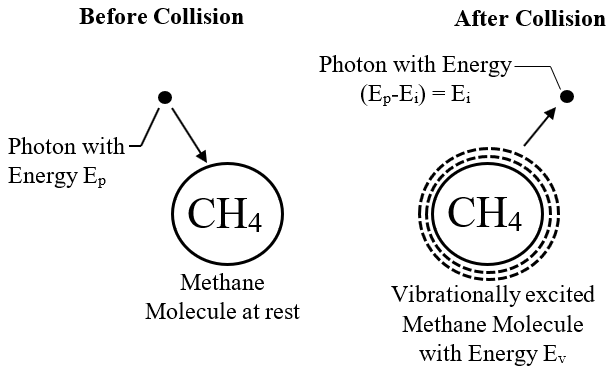

Figure 7: An Inelastic Collision between a Photon and a Methane Molecule. Energy from the Photon is Deposited into the Molecule as Vibrational Energy, E_v. The Photon leaves the Collision with Energy E_i (Smith, 1998)

In totally inelastic collision (figure 8), the photon disappears and all its energy is absorbed by the molecule leaving it excited. This phenomenon is known as absorbance. The wavenumber of the light absorbed depends upon the molecule involved in the collision. Thus, the chemical information derived from a plot of intensity versus wavenumber, is called an absorbance spectrum. Figure 9 shows a plot of absorbance spectrum of benzyl alcohol.

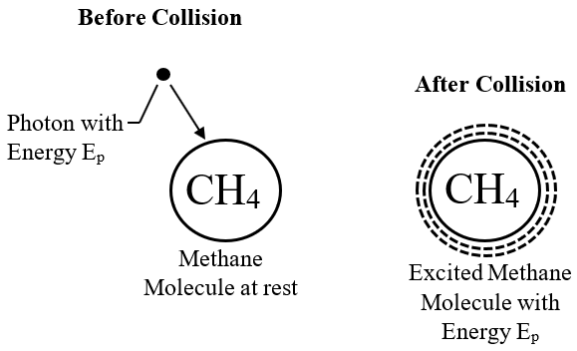

Figure 8: A Totally Inelastic Collision between a Photon and a Methane molecule, known as Absorbance (Smith, 1998)

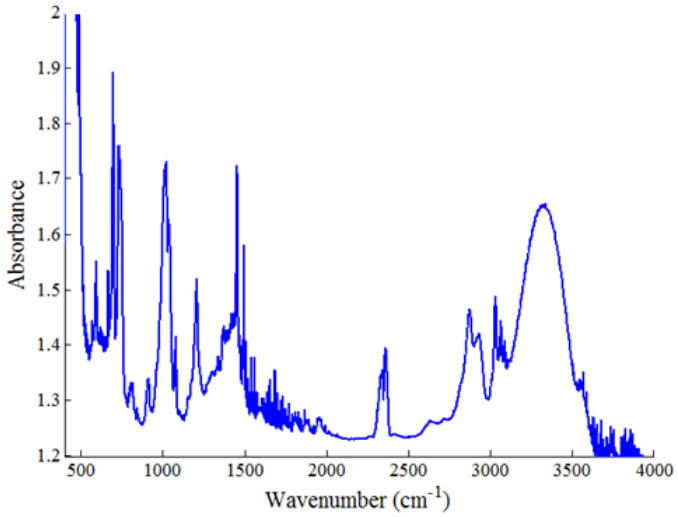

Figure 9: The IR Spectrum of Benzyl Alcohol plotted as Absorbance against Wavenumber

Molecular Vibrations

To determine the frequency of a vibrational mode of a molecule say HCl, for a simplified model, the assumption is that, the HCl molecule vibrate and the two atoms H and Cl move in phase with each other with the same amplitude. This phenomenon is likened to the harmonic oscillator as seen in figure 10.

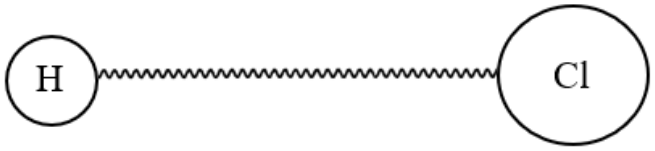

Figure 10: H-Cl Molecule Vibrationally Excited by a Photon with Energy hc$W$

(Smith, 1998)

The molecule's mass also called the reduced mass is related to the masses of the individual atoms as in equation 8.

$$\mu = \frac{M_1 M_2}{M_1 + M_2} \tag{8}$$

where μ is the reduced mass in kg, M_1 is the mass of atom 1 in kg, M_2 is the mass of atom 2 in kg.

From Hooke's law, when a spring is stretched

$$F = -kx \tag{9}$$

where F is the restoring force of the springs in N, k is the force constant of the spring in N/m, x is the displacement of the spring from its equilibrium position in m.

Equation 9 depends on two conditions. The first condition is the force constant (k) of the spring, which is the measure of the spring's stiffness. The second is how far the spring is pulled (x). In terms of molecules, x is the change in the bond length from the equilibrium position, and the force constant is the measure of the chemical bond's strength.

From Newton's second law,

$$F = ma \tag{10}$$

$$-kx = m\frac{d^2x}{dt^2} \tag{11}$$

where F is the force in newtons (N), m is the mass in kilogram (Kg), a is the acceleration in metre per second squared (m/s^2), $\frac{d^2x}{dt^2}$ is the second derivative of displacement (x) with respect to time (t)

The equation relating the force constant (k), the reduced mass (μ), and the frequency (ν) of absorption is given by

$$\nu = 1/2\pi\sqrt{\frac{k}{\mu}} \tag{12}$$

Equation 12 gives the frequency of light that a molecule will absorb, and the frequency of vibration of the normal mode excited by that light. Equation 12 can be modified to obtain equation 13.

$$W = 1/2\pi c\sqrt{\frac{k}{\mu}} \tag{13}$$

where the parameters have their usual meanings.

Conditions Necessary for Infrared Absorption to Occur

Infrared absorption involves the interaction of the electric field vector with matter. Absorption occurs when there is a change in the dipole moment after absorption of infrared radiation by the sample. The dipole moment is a measure of the charge asymmetry of a molecule. The magnitude of the dipole moment is calculated from equation 14.

$$\Omega = qr \tag{14}$$

where Ω is the magnitude of the dipole moment, q is the charge of the atom, r is the bond distance.

The first necessary condition for a molecule to absorb infrared radiation is that, the change in dipole moment with respect to distance should be non-zero. That is;

$$\frac{\partial \Omega}{\partial r} \neq 0 \qquad (15)$$

where $\partial\Omega$ is the change in the dipole moment, ∂r is the change in bond distance. The second condition necessary for infrared absorption to take place is the energy of the light impinging on the molecule must be equal to the vibrational energy level difference within the molecule.

Transmission Methods

Transmission infrared spectroscopy is the most straightforward method. The technique is based upon the absorption of an infrared radiation at specific wavelengths as it transmits through a sample. It is possible to analyse samples in solid, liquid or gaseous state (Chalmers & Griffiths, 2002; Ozaki, McClure, & Christy, 2006).

Solid Samples

The general methods used for examining solid samples in transmission infrared spectroscopy are the alkali halide discs, mulls and films. Alkali halide disc involves mixing the solid sample with dry alkali halide powder using an agate mortar and pestle and subjecting it to a pressure of about 1.575×10^{5} Kgm^{-2} in an evacuated die. This sinters the mixture and produces a clear transparent disc. Commonly used alkali halide is potassium bromide (KBr), which is completely transparent in the mid-infrared region. Two major

disadvantage of the alkali halide disc are, they are hygroscopic and takes longer time to produce clear transparent disc.

The mull method involves grinding the sample to reduce the particle size and suspending it in one or two drops of mulling agent. The most commonly used mulling agent is Nujol (liquid paraffin).

Films are produced by either solvent casting or by melt cooling. In solvent casting, the sample is dissolved in an appropriate solvent. The solvent does not only dissolve the sample, but also produce a uniform film. The solution is poured onto a levelled glass plate, e.g. Microscope slide or a metal plate and spread to a uniform thickness. The solvent is evaporated in an oven and, once dried, the film is stripe off.

Liquid and Solution Samples

Several different types of transmission solution cells are available. Fixed path-lengths sealed cells are useful for volatile liquids but cannot be taken apart for cleaning. A semi-permanent cell as seen in figure 11. The spacer is usually made of polytetrafluoroethylene (PTFE, known as ‘Teflon’) and is available in various pathlengths.

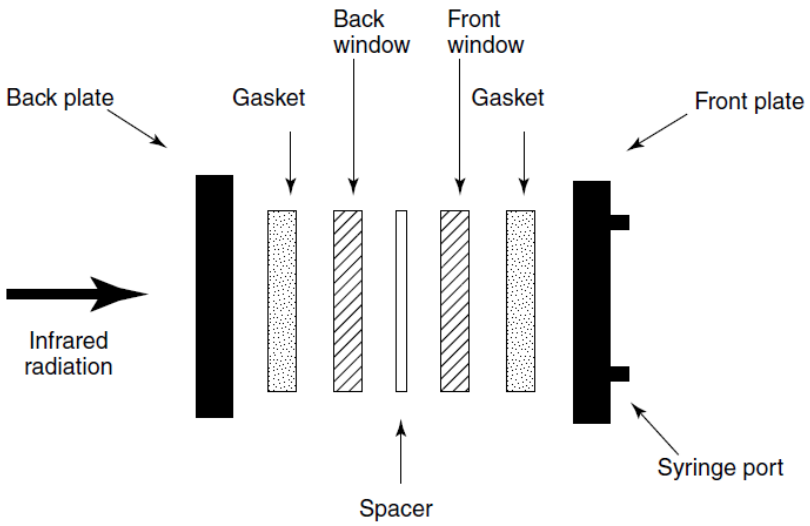

Figure 11: A schematic Diagram of a Typical Semi-Permanent Liquid Cell (Smith, 1998)

Infrared cells must be transparent to the incident infrared radiation and alkali halides are usually used in transmission methods. The cheapest material is sodium chloride (NaCl), but other commonly used materials are listed in Table 1.

Gaseous Sample

Gases on the other hand have densities which are several orders of magnitudes less than liquids and hence, path-lengths are correspondingly greater, usually 10 cm or longer. A typical gas cell is shown in figure 12. The walls are made of glass or brass with the usual choice of windows. The gas cell can be filled by flushing of from a gas line.

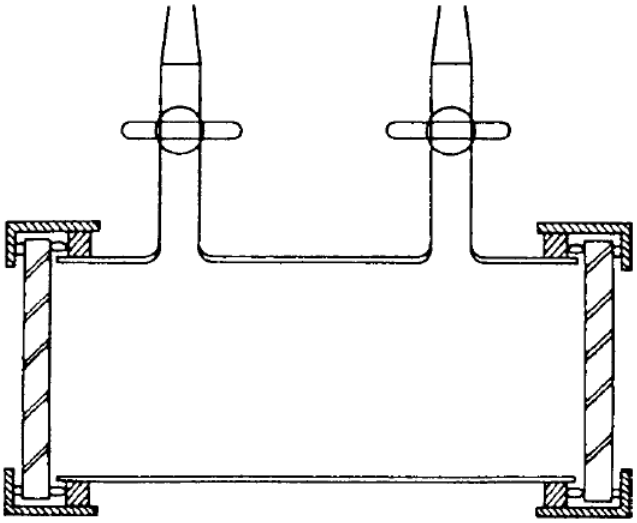

Figure 12: A Schematic Diagram of a Typical Infrared Gas Cell (Smith, 1998).

Table 1: Summary of some Optical Materials used in Transmission Spectroscopy

Window material	Useful range (cm^{-1})	Refractive index	Properties
NaCl	40,000 – 600	1.5	Soluble in water, slightly soluble in alcohol, low cost, fair resistance to mechanical and thermal shock, easily polished
KBr	43,500 – 400	1.5	Soluble in water and alcohol, slightly soluble in ether, hygroscopic, good resistance to mechanical and thermal shock
CaF_2	77,000 – 900	1.4	Insoluble in water, resists most acids and bases, does not fog, useful for high-pressure work
BaF_2	66,666 – 800	1.5	Insoluble in water, soluble in acids and NH_4Cl, does not fog, sensitive to thermal and mechanical shock
KCl	33,000 – 400	1.5	Similar properties to NaCl but less soluble, hygroscopic
CsBr	42,000 – 250	1.7	Soluble in water and acids, hygroscopic
CsI	42,000 – 200	1.7	Soluble in water and alcohol, hygroscopic

Source: (Smith, 1998; Stuart, 2005)

Reflectance Methods

Reflectance sampling is the second major family of infrared sample preparation methods. There are two categories of reflectance measurements. Internal reflectance measurements using an attenuated total reflectance cell in contact with the sample. The external reflectance measurements which involves an infrared beam reflected directly from the sample surface.

Attenuated Total Reflectance (ATR)

Figure 13 shows a simplified diagram for Attenuated Total Reflectance (ATR) that operates on the principle of internal reflectance. Figure 13 shows an IR beam travelling through a crystal of high refractive index n_c, which encounters a boundary with a sample with lower refractive index n_s. The dotted line (NN') in figure 13 is the surface normal to the ATR crystal and the angle the incoming IR beam makes with the surface normal is called the angle of incidence, θ_i. What happens to the infrared beam when it reaches the boundary of the two media depends upon θ_i. If the angle of incidence is small, some of the beam will be reflected off the internal surface of the crystal and some of the beam will be refracted out of the crystal into the sample given the refracted beam (figure 13). The angle of refraction, θ_R, is the angle the refracted beam makes with the surface normal. From the laws of refraction, as θ_i increases θ_R increases. At some angle of incidence, the angle of refraction becomes 90^o and the IR beam no longer leave the crystal, but remain within it. In this case, all the IR beam reflects off the internal surface of the crystal and this is called total internal reflection.

The minimum angle of incidence at which total internal reflection occurs in a material is called its critical angle, θ_c. The critical angle depends upon the refractive indices of the crystal and the sample based on Equation 16.

$$\theta_C = \sin^{-1}(n_S / n_C) \quad (16)$$

where θ_C is the Critical angle, n_S is the Refractive index of sample and n_C is the Refractive index of crystal.

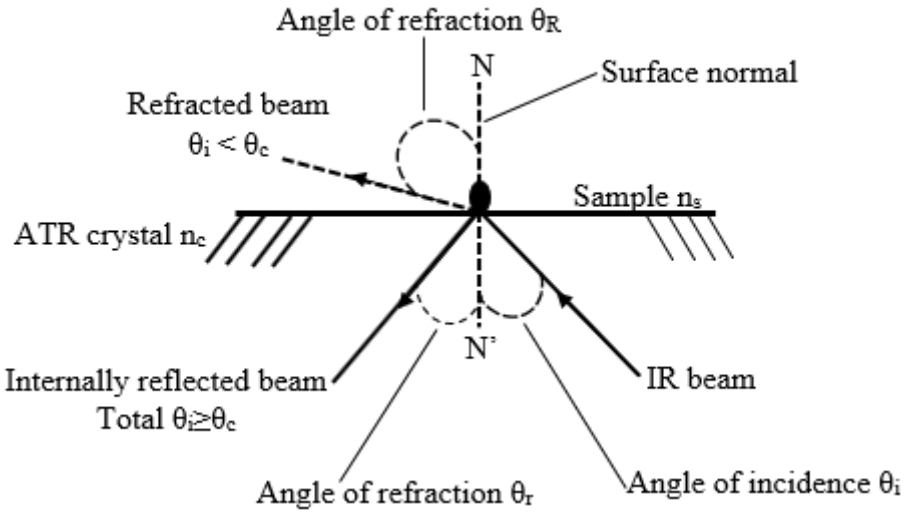

Figure 13: Optical Processes that occur when an Infrared Beam in a Crystal of High Refractive Index, n_c, Encounter a Sample of Lower Refractive Index n_s (Smith, 1998)

If the sample is a typical organic material with n = 1.5 and the crystal is diamond with n = 2.42, the critical angle is 38.3°. Equation 16 has a physical meaning of $n_s < n_c$, and by definition the sine of the angle cannot be greater than unity. At the point of internal reflectance, the incoming and outgoing infrared beams occupy the same volume. Under the right conditions ($\theta_i \geq \theta_c$) these two beams undergo constructive interference. The IR beam amplitude at the point

of internal reflection will be greater than the amplitude on either side. The enhanced amplitude has nowhere to go but build up, which results in the in infrared light sticking up the space above the crystal surface, which is called an evanescent wave as shown in figure 14. Evanescent wave is sometimes called "hot spot".

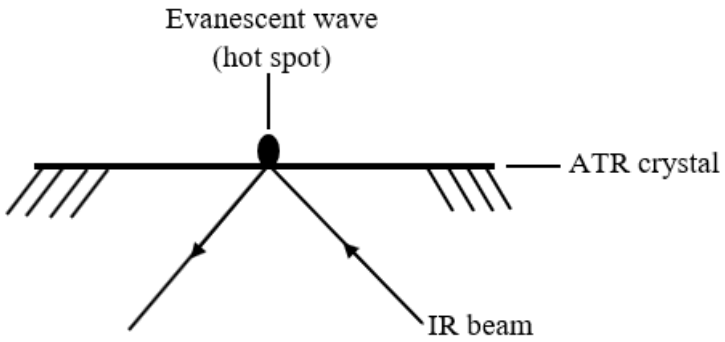

Figure 14: Evanescent Wave, or "hot spot" that forms when an Infrared Beam Undergoes Total Internal Reflectance (Smith, 1998)

The evanescent wave sticks up the surface of the crystal by less than a micron to up to 20 microns. To measure the spectrum of a sample, the sample is brought into contact with the hot spot, some of the beam is absorbed by the sample and the beam is focused onto the detector. Since the sample absorbances attenuates the intensity of the totally reflected infrared beam, the term attenuated total reflectance (ATR) is used. Figure 15 shows how an ATR crystal is used to record the spectrum of the sample. This technique allows for any sample brought in contact with the hot spot will have its spectrum measured. For solids; polymers and powders, a clamp is used to apply pressure to the sample to obtain a good sample / hot spot contact.

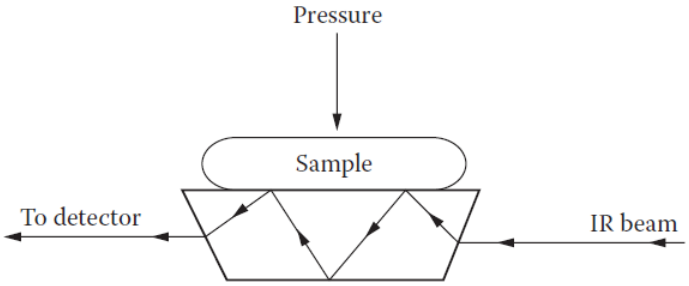

Figure 15: ATR Crystal with two hot spots on its Top Surface. Pressure is applied to some Solid Samples using a clamp to facilitate Sample/hot spot Contact (Smith, 1998)

Depth of Penetration

The depth of penetration (DP) determines how far the infrared beam penetrates into the sample. The intensity of the evanescent wave decreases exponentially with distance above the surface of the ATR crystal. The DP is the depth at which the evanescent wave intensity decreases to 36.8 % (= 1/e, where e is the base of natural logarithms) of its initial value. The *DP* for an ATR experiment is given in equation 17.

$$DP = \frac{1}{2\pi W n_C [\sin^2 \theta_i - n_{SC}^2]} \tag{17}$$

where DP = Depth of penetration, W = Wavenumber, n_C = Refractive index of ATR crystal, θ_i = Angle of incidence and $n_{SC} = \frac{n_{Sample}}{n_{Crystal}}$.

In equation 17, all of the parameters are in the denominator, so if any of them increases, *DP* decreases and vice versa. At 1000 cm^{-1} a diamond crystal with n_c = 2.42, angle of incidence of 45^o and sample refractive index of 1.4 (typical of many organic materials) gives DP of 1.6 cm.

Effects of *W* on the ATR Technique

Since wavenumber *W* is in the denominator of equation 17, as *W* increases, DP decreases. Thus, 1000 cm^{-1} light penetrates three times farther into the sample than 3000 cm^{-1} light. When a spectrum is plotted with low wavenumber to the right, DP decreases as you read the spectrum from right to left, so does the peak height decrease as well. The interpretation of ATR spectra is dependent on the wavenumber. It is difficult to compare ATR spectra to the spectra measured using other sampling techniques because the spectra of the sample will look different, as seen in figure 16.

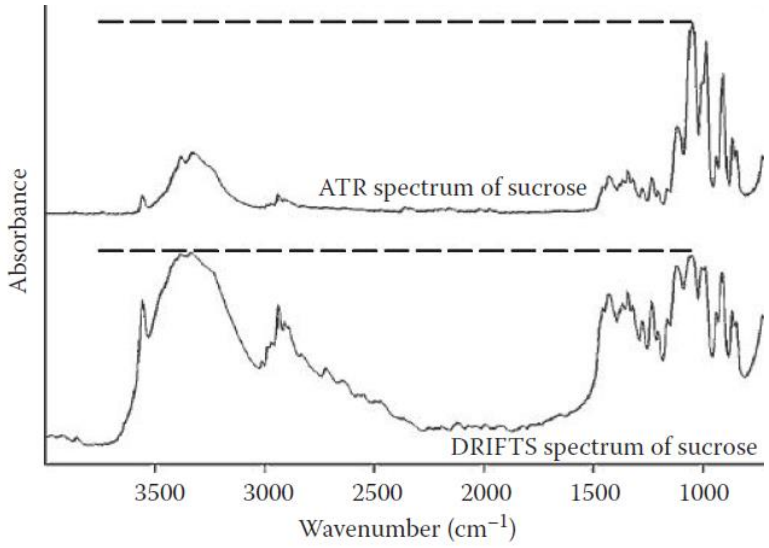

Figure 16: Bottom: Diffuse Reflectance Fourier Transform Spectroscopy (DRIFTS) Spectrum of Sucrose (table sugar). The dashed line shows that the Peaks at high and low Wavenumber are about the same Intensity. Top: The ATR Spectrum of Sucrose. The dashed line shows that the Peaks at high Wavenumber are less intense than the Peaks at low Wavenumber (Smith, 1998)

The second parameter of interest in equation 17 is the refractive index of the ATR crystal, n_c, which means as n_c increases, the DP decreases. The infrared beam will penetrate to different depth for ATR crystals of different refractive indices. There are available ATR accessories that make it easy to switch between crystals with different values of n_c. This allows spectra of a sample to be measured at different depths non-destructively. Table 2 shows the properties of common ATR crystals (Albani, 2007; Gauglitz et al., 2014; Smith, 1998, 2011; Stuart, 2005).

Table 2: Common ATR Crystals and their Properties

Crystal Material	Refractive Index	Wavenumber Ranges (cm^{-1})	Colour	pH Range	Comments
KRS-5	2.37	20,000 – 250	Red	5 – 8	Soft, highly toxic, rarely used today
ZnSe	2.42	15,000 – 600	Yellow	5 – 9	Once very common, brittle, attacked by strong acids and bases
Si	3.42	8910 – 660	Grey	1 – 12	
Ge	4.0	5500 – 600	Grey	1 – 14	Shallow DP, durable
Diamond	2.42	30,000 – 2200 2000 – 400			Tough, durable, absorbs in mid-infrared

Source: (Albani, 2007; Gauglitz et al., 2014; Smith, 1998, 2011; Stuart, 2005)

The Phyto-Constituents found in Medicinal Plants

Medicinal plants play an important role to the health of individuals and communities. The medicinal value of these plants lies in the chemical substances that produces a definite physiological action on the health of an individual. Some of the most important of these Phyto/bioactive constituents of medicinal plants are phenol, polyphenols, glycosides, terpenes, triterpenoids and saponins, polysaccharides, alkaloids, etc. These Phyto-constituents are also called secondary metabolites and are responsible for the medicinal properties of medicinal plants (Pengelly, 2004).

Phenols

Phenols are one of the largest groups of secondary metabolites. They are considered to be aromatic alcohols because the functional hydroxyl group is always attached to a benzene ring as seen in figure 17.

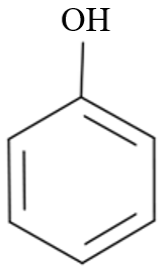

Figure 17: Chemical Structure of Phenol

For all alcohols, the names of phenols always end in the letters ‘ol’. Furthermore, the ring system sometimes bear other substitutes, especially, methyl groups. Phenols are distributed among all classes of plants. Some properties of phenols are bactericidal, antiseptic and anthelmintic. Phenol is

standard for other antimicrobial agents (Bruneton, 1995; Iwu, 2014; Khare, 2008; Pengelly, 2004; Rios & Recio, 2005).

Polyphenols

Tannins and Flavonoids are two classes for polyphenols, with tannins being the largest group of polyphenols. They are widely isolated from the back of trees, leaves, stems and fruit. The first tannins were first isolated from the bark of oak tree and are responsible for astringency. Tannins are non-crystalline compounds and their ingestion give rise to a puckering, astringent sensation in the mouth and the taste is sour. They occur as glycosides and precipitate proteins into insoluble complexes which enables tanning of animal hides in leather making. Tannins are classified as either hydrolysable tannins or condensed tannins.

Simple phenolic acids, particularly, gallic acid is obtained from hydrolysable tannins. Some actions of hydrolysable tannins include: protecting inflamed mucous membranes, prevent bleeding from small wounds, reduce uterine bleeding, for example menorrhagia, metrorrhagia, binding effect in the gut thus relieves diarrhoea, dysentery and also used externally ad douches, snuffs, eyewash. Condensed tannins or phlobotannins are polymers of flava-3-ol (catechins) and flava-3,4-diols (leucoanthocyanins). They are only partially soluble in water and alcohol.

Flavonoids on the hand occur as yellow and white plant pigments. They both occur in free states and as glycosides. The structure is based on a C_{15} skeleton consisting of two benzene rings connected by a three-carbon chain, that is C_6-C_3-C_6. Flavonoids are generally found in the plant kingdom and are the

most common plant pigments next to chlorophyll and carotenoids. They protect plant tissues from the damaging UV radiation, acts as antioxidants, enzyme inhibitors, plant and light screens. In humans, experiments have shown flavonoids affect the heart and circulatory system and strengthen the capillaries. They are also known to have synergetic effects with ascorbic acid. Therapeutic effects of flavonoids have been observed as antioxidants, antiviral, hepatoprotective, antiatheromatous, anti-inflammatory and anti-hypertensive. Some flavonoids include quercetin, kaempferol and myricitin as well as the catechin-type condensed tannins found in black tea (Bruneton, 1995; Iwu, 2014; Khare, 2008; Pengelly, 2004; Rios & Recio, 2005).

Glycosides

Glycosides are groups of compounds characterised by a sugar portion (or moiety) attached by a special bond to one or more non-sugar portions. They are widely distributed among the plant kingdom and can be found in seeds of pulses, in swollen underground roots or shoots (yams, sweet potatoes), flowers and leaves. Some are toxic especially cyanogenic and cardiac glycosides. Cooking may render them non-toxic. An amygdalin-containing drug known as laetrile has been used as a cytotoxic agent in cancer, though its use is now restricted. In small quantities, these glycosides do exhibit expectorant, sedative and digestive properties. White cherry bark, from Prunus serotine, is an excellent cough remedy and tonic, as well as a flowering agent used in cough syrups (Bruneton, 1995; Iwu, 2014; Khare, 2008; Pengelly, 2004; Rios & Recio, 2005).

Terpenes

Terpenoids or terpenes are one of the most important groups of active compounds in plants with over 2,000 known structures. Their structures are divided into isoprene (five carbon) units containing two unsaturated bonds. They are synthesised from acetate via the mevalonic acid pathway. Figure 18 shows the chemical structure of isoprene.

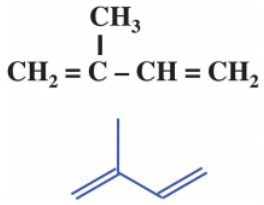

Figure 18: Chemical Structure of Isoprene

In the formation of terpenes, the isoprene units are linked in the head to tail fashion. The number of units incorporated into a particular terpene serves as a basis for the classification of these compounds. Table 3 shows the classification for terpenes. Therapeutic uses of terpenes include antimicrobial, antifungal, antiviral, antihyperglycemic, anti-inflammatory, antioxidants, antiparasitic and immunomodulatory (Brahmkshatriya & Brahmkshatriya, 2013).

Table 3: Classification of Isoprene

Class	Chemical formulae	Remarks
Isoprene	C_5H_8	
Terpene	$(C_5H_8)n$	
Monoterpene	$C_{10}H_{16}$	Essential oils, e.g. menthol, iridoids
Sesquiterpene	$C_{15}H_{24}$	Bitter principles, especially sesquiterpene lactones
Diterpene	$C_{20}H_{32}$	Resin acids, bitter principles
Triterpene	$C_{30}H_{48}$	Saponins, steroids
Tetraterpene	$C_{40}H_{64}$	Carotenoids
Polyterpene	(C_5H_8)n	Rubber

Source: (Pengelly, 2004)

Triterpenoids and Saponins

Triterpenoid compounds are derived from C_{30} precursor, squalene, which was first isolated from shark liver (Bruneton, 1995). They have similar configurations to steroids (found in plants and animals), whose C_{27} skeletons are also derived from squalene. Triterpenoid are a large and diverse group made up of several subclasses:

- Free triterpenes
- Triterpenoid saponins
- Steroidal saponins
- Cardiac glycosides
- Phytosterols
- Curcurbitacins

- Quassinoids

The systematic effects for the various saponins are listed as follows:

- Anti-cancer: cytotoxic, anti-tumour, anti-mutagenic
- Anti-inflammatory, anti-allergic
- Immunomodulatory, anti-viral
- Anti-hepatotoxic
- Anti-diabetic: hypoglycaemic
- Anti-fungal
- Molluscicidal
- Cardiac activity: haemolytic, anti-thrombotic, hypocholesterolemic

Polysaccharides

High-molecular-weight polymers consisting of chains of sugars (monosaccharides or oligosaccharides) with chemical linkages are called Polysaccharides of glycans. The simplest polysaccharides are cellulose and starch, which are polymers of glucose only. Polysaccharides are difficult to represent in the usual structural formulas as they are so big and often the identity and the number of all the structures are represented by a section of the molecule, or by a series of named sugars with indications of the bonding arrangement and branching patterns. Polysaccharides are widely distributed in the plant kingdom. Also, they can occur in algae or fungi. Their functions include food storage, protection of membranes, and also maintaining rigidity of cell walls in plants (Bruneton, 1995; Iwu, 2014; Khare, 2008; Pengelly, 2004; Rios & Recio, 2005).

Alkaloids

Alkaloids are alkaline organic compounds containing one or more nitrogen atoms, each connected to at least two carbon atoms within a heterocyclic ring system. Alkaloids are found in 15-30 % of all flowering plants and are particularly common in certain families, such as Fabaceae, Liliaceae, Ranunculaceae, Apocynaceae, Solanaceae and Papaveraceae. The most widely occurring alkaloids are Berberine and caffeine. More than 10,000 different alkaloids have been isolated from over 300 plant families. Alkaloids are usually found in roots, rhizomes, leaves, bark, fruit or seeds. Alkaloids are generally white or colourless crystalline solids containing oxygen. Most alkaloids are soluble in organic solvents such as chloroform, ether or alcohol but water insoluble.

Plants alkaloids have profound physiological actions in humans with nervous system effects being the most prominent. Examples of some of the more dramatic actions of alkaloids are enumerated as follows:

- Analgesics/ narcotics-morphine
- Mydriatics-atropine
- Miotics-pilocarpine
- Hypertensive-ephedrine
- Hypotensives-reserpine
- Bronchodilator-lobeline
- Stimulants-strychnine
- Antimicrobials-berberine
- Antileukemic-vinblastine

Multivariate Data Analysis

Multivariate analysis refers to any statistical technique that is used to analyse data which arises from more than one variable. The goal of multivariate analysis is for simplification of data, and to reduce the dimensions of data. Such techniques can be termed as exploratory. Multivariate analysis is concerned generally with two areas, thus, descriptive and inferential statistics. The descriptive statistics obtain optical linear combinations of variables. The linear combination reveals two fundamental reasons: (1) mathematical tractability (2) often performs well in practice. In the inferential statistics, inference is made from sample data of a population or make judgement of the probability that an observed difference between groups is a dependable one or one that might have happened by chance.

Data Pre-Treatment Methods

Mathematical pre-treatment methods (Ozaki et al., 2006) mostly applied to spectroscopy data are noise reduction, baseline correction, normalization and resolution enhancement. These techniques are applied to spectroscopy because spectra often suffer from problems of unwanted spectral variations and baseline shifts as a result of light scattering from samples, poor reproducibility spectra caused by pathlength variations, variations from the environment (temperature, density, and particle size of samples) and noise from the detector (Ozaki et al., 2006).

Noise Reduction Techniques

Spectra data are characterized by several kinds of noise which arise from various interfering physical and chemical processes. These unwanted noises influence the outcome, therefore there is the need to reduce its effect. Smoothing methods are mostly applied to reduce the effect on noise to data (Ozaki et al., 2006). Smoothing is a moving average where for example the absorbance (A_i) at each variable $i = 1, 2, ...k$ is replaced by a weighted average of itself and its nearest neighbours. From $i - n$ to $i + n$;

$$A_i = \sum_{k=n}^{\infty} w_k A_{i+k} \tag{18}$$

where A_i is the Absorbance and w_k is the weights.

Baseline Correction

Baseline correction are used to adjust the spectral offset by either adjusting the data to the minimum point in the data, or by making a linear correction based on two user-defined variables. The two transformations used to correct the baseline of the samples are baseline offset correction and linear baseline correction.

Baseline Offset Correction

The baseline offset correction can be written as

$$f(x) = x - \min(X) \tag{19}$$

where x is a variable and X denotes all selected variables for the sample. For each sample, the value of the lowest point in the spectrum is subtracted from all

the variables. The result of this is that the minimum is set to zero (0) and the rest are positive values.

Linear Baseline Correction

This transformation transforms a sloped baseline into a horizontal baseline. The technique is to point out two variables which define the new baseline. It is calculated using the general linear equation of a straight line.

$$r = Mx + C \tag{20}$$

$$\text{where } M = \frac{r_2 - r_1}{r_2 - r_1} \text{ and } C = M * x$$

where r_2 and r_2 are two points on the line , x is the independent variable , C is the intercept and r the dependent variable.

Normalization

Normalization is a method of scaling samples in order to get all the data on the approximately the same scale (Ozaki et al., 2006). Some of the normalization methods are:

1. Area Normalization: This transformation normalizes an observation (i.e. spectrum) X_i by finding the area under the curve for the observation.

$$\overline{X_i} = \frac{X_i}{\sum_j X_{ij}} \tag{21}$$

2. Unit Normalization: This transformation normalizes sample-wise data X_i to unit vectors.

$$\overline{X_i} = \frac{X_i}{\sqrt{\sum_j X_{ij}}} \quad (22)$$

3. Mean Normalization: This type of normalization consists of dividing each row (each observation) of the data matrix by its average, thus neutralizing the influence of any hidden factor.

$$\overline{X_i} = \frac{X_i}{mean(X_i)} \quad (23)$$

4. Maximum Normalization: This normalization involves dividing each observation by its maximum value instead of its average.

$$\overline{X_i} = \frac{X_i}{\max(X_i)} \quad (24)$$

5. Range Normalization: This normalization involves dividing each observation by its range (i.e. “max value-min value”).

$$\overline{X_i} = \frac{X_i}{\max(X_i) - \min(X_i)} \quad (25)$$

Resolution Enhancement

Mean centering is a useful resolution enhancement method. It is the adjustment to a data set to reposition the centroid of the data to the origin of the coordinates system (Ozaki et al., 2006). Each mean centering spectrum can be regarded as a spectrum obtained by difference between a single spectrum and an average spectrum.

Principal Component Analysis (PCA)

Principal Component Analysis (PCA), introduced in 1933 by Hotelling (Hotelling, 1933), is an exploratory statistical technique used to reveal hidden structures within large data sets. It provides a visual representation of the relationships between sample and variables and provide insight into how measured variables cause some samples to be similar to or how they differ from each other.

Geometric Approach of Principal Components

PCA deals with a single sample of n observations vectors $y_1, y_2, ..., y_n$ that form a swarm of points in P dimensional space. It is important to visualize geometrically if the swarm of points is ellipsoidal even though PCA can be applied to any distribution of y.

If the variables $y_1, y_2, ..., y_n$ in y are correlated, the ellipsoid swarm of point is not oriented parallel to any of the axes represented by $y_1, y_2, ..., y_n$. We wish to find the natural axes of the swarm of points (the axes of the ellipsoid) with origin at $\overline{y}$, the mean vector of $y_1, y_2, ..., y_n$. This is performed by translating the origin to $\overline{y}$ and then rotating the axes. After rotation so that the axes become the natural axes of the ellipsoid. The new variable (principal components) will be uncorrelated. We shall write $y_i - \overline{y}$ when there is an explicit need, otherwise we assume that y_i has been centred.

The axes is rotated by multiplying each y_i by an orthogonal matrix B $(B'B = I)$

$$z_i = By_i \tag{26}$$

thus, the distance to the origin is unchanged.

$$z_i^{'} z_i = (By_i)^{'}(By_i) = y_i^{'} B^{'} By_i = y_i^{'} y_i \tag{27}$$

The orthogonal matrix transforms y_i to a point z_i that is the same distance from the origin from the origin and the axis effectively rotated. The new variables (principal components) $z_1, z_2, ..., z_p$ in $z = By$ are uncorrelated. Thus, the sample covariance matrix of z, $S_z = BSB^{'}$, which is diagonal

$$S_z = BSBs^{'} = \begin{pmatrix} S_{z_1}^2 & 0 & ... & 0 \\ 0 & S_{z_2}^2 & ... & 0 \\ \vdots & \vdots & \ddots & \vdots \\ 0 & 0 & ... & S_{z_p}^2 \end{pmatrix} \tag{28}$$

where S is the sample covariance matrix of $y_1, y_2, ..., y_n$.

From $D^{'}SD = E = diag(\phi_1, \phi_2, ..., \phi_n)$, where the ϕ_i's are eigenvalues of S and D is an orthogonal matrix whose are normalized eigenvectors of S. Thus, the orthogonal matrix B that diagonalizes S is the transpose of the matrix D:

$$B = D^{'} = \begin{pmatrix} a_1^{'} \\ a_2^{'} \\ \vdots \\ a_p^{'} \end{pmatrix} \tag{29}$$

Where a_i it the *ith* normalized $\left(a_i^{'} a_i = 1\right)$ eigenvector of S. The principal components are the transformed variables $z_i = a_1^{'} y$, $z_2 = a_2^{'} y, ...,$ $z_p = a_p^{'} y$ and $z = By$. The diagonal elements of $BSB^{'}$ on the right side of equation 28 are

eigenvalues of S. Hence the eigenvalues $\phi_1, \phi_2, ..., \phi_p$ of S are the (sample) variances of the principal components $z_i = a_i^{'} y$:

$$s_{z_i}^2 = \phi_i \tag{30}$$

Since the rotation lines up with the natural extensions of the swarm of points $z_p = a_p^{'} y$ has the smallest variance. This follows from equation 13, because the variance of z_i is ϕ_1, the largest eigenvalue, and the variance of z_p is ϕ_p, the smallest eigenvalue.

The eigenvalues are the variances of the principal components "the proportion of variance explained" by the first k components:

$$\text{Proportion of variance} = \frac{\phi_1 + \phi_2 + ... + \phi_k}{\phi_1 + \phi_2 + ... + \phi_p}$$

$$= \frac{\phi_1 + \phi_2 + ... + \phi_k}{\sum_{j=1}^{p} s_{jj}} \tag{31}$$

Since $\sum_{i=1}^{p} \phi_i = tr(S)$, then we represent p - dimensional points $\left(y_{i1}, y_{i2}, ..., y_{ip}\right)$ with few principal components $\left(z_{i1}, z_{i2}, ..., z_{ip}\right)$ that account for a large proportion of the total variance. If a few variables have relatively large variances, they will figure disproportionately in $\sum_j s_{jj}$ and in the principal components (Abdi & Williams, 2010; Brereton, 2003; Jackson, 1981; I. Jolliffe, 2011; Ian T Jolliffe, 1986; I. T. Jolliffe, 2002; Phaladiganon, Kim, Chen, & Jiang, 2013; Shlens, 2014; Wold, Esbensen, & Geladi, 1987; Yeomans & Golder, 1982).

Linear Discriminant Analysis (LDA)

Linear Discriminant Analysis (LDA) is classified as one of the traditional approaches for dimensionality reduction. It is also called Fisher's linear discriminant or mapping. The general goal of LDA is to reduce the dimensionality to one dimension, thus projecting it onto a line (Berrueta, Alonso-Salces, & Héberger, 2007; Chen, Cai, Wan, & Zhao, 2011; Coomans, Jonckheer, Massart, Broeckaert, & Blockx, 1978; Roggo et al., 2007).

Consider a set of $n \times p$ – dimensional observations $x_1, ..., x_n$, with n_1 samples labelled as belonging to class 1 (μ_1) and n_2 samples as belonging to class 2 (μ_2). Let denote a vector p with unit norm, we form a projection x_i onto a line in the direction of p using equation 32.

$$y = p^T x \tag{32}$$

p is chosen to provide a linear mapping that yields maximal separation of the two classes. We calculate the p - dimensional sample mean for each class using equation 33.

$$m_i = \frac{1}{n_i} \sum_{x \in \Lambda_i} x \tag{33}$$

The sample mean for the projected points is given by equation 34.

$$\begin{aligned} \overline{m_i} &= \frac{1}{n_i} \sum_{x \in \Lambda_i} y \\ &= \frac{1}{n_i} \sum_{x \in \Lambda_i} p^T x \end{aligned} \tag{34}$$

Combining equation 33 and 34 yields

$$\overline{m_i} = p^T m \tag{35}$$

Equation 35 measures the separation using the means of the two classes. To obtain good class separation and good classification performance, the separation of the means must be as large as possible relative to some measure of the standard deviation for the observations in each class. The scatter is used as a measure of the standard deviations. The scatter for the *i-th* class of projected data points given as

$$\overline{S_i} = \sum_{y \in \Lambda_i} (y - \overline{m_i})^2 \tag{36}$$

The total within – class scatter is $\overline{S_1}^2 + \overline{S_2}^2$. The LDA is defined as the vector p that maximises the function

$$J(p) = \frac{\left|\overline{m_1} - \overline{m_2}\right|^2}{\overline{S_1}^2 + \overline{S_2}^2} \tag{37}$$

A solution to maximize equation 37 is

$$Z = S_Z^{-1}(m_1 - m_2) \tag{38}$$

where S_Z is the within – class scatter matrix defined by

$$S_Z = S_1 + S_2$$

and

$$S_i = \sum_{x \in \Lambda_i} (x - m_i)(x - m_i)^T \tag{39}$$

The matrix S_Z is proportional to the sample covariance matrix for the pooled p - dimensional data. The LDA is the linear mapping with the maximum ratio of between – class, where

$$S_B = (m_1 - m_2)(m_1 - m_2)^T \tag{40}$$

K-Nearest Neighbour (KNN)

K-Nearest Neighbour (KNN) is a non-parametric classification method that assumes the number of observations within each class are similar. The steps for KNN are**:** 1) the calibration set is assigned to known classes 2) the distances (Euclidean) of unknown observations are calculated to all members of the training set 3) rank the distances as in 2) in ascending order 4) match the established classes to which the unknown is nearest to the smallest k distance 5) determine the robustness of the KNN models with varying K values eg. 3, 5, and so on. The identification rate from the KNN model is influenced by the parameter K, and it is determined through the KNN training process (Berrueta et al., 2007; D. Coomans & D. Massart, 1982; D. Coomans & D. L. Massart, 1982; Roggo et al., 2007).

Support Vector Machine (SVM)

Support Vector Machine (SVM) is a non-linear discriminative classifier based on statistical learning theory. SVM processes data by obtaining the optimal boundary of groups in a vector space independent on the probabilistic arrangements of vectors in the training set. Given the training set $T = \sum_{i-1}^{n}(x_i, y_i)$ with $x \in R^n$ and $y_i \in (-1,1)$, and a linear function $g(x) = w^T x + b$, the SVM requires the solution of the optimization problem to be:

$$\min \frac{1}{2} w^T w + C\sum_{i=1}^{n} \gamma_i$$

$$\text{s.t. } y_i(w^T x_i + b) \geq 1 - \gamma_i \qquad (41)$$

where γ_i is the slack variables allowing samples to violate constraints and C is the penalty parameter of the error term, w is the weight vector and b is the bias.

SVM creates a hyperplane that allows linear separation in the higher dimension feature space. However, the kernel function, $K(x_i, x_j) = x_i^T x_j$, is used when the classes are separated by a non-linear boundary. The boundaries are found by mapping the non-separable data into a higher dimensional space. This causes the classes to become linearly separated (Berrueta et al., 2007; Thissen, Pepers, Üstün, Melssen, & Buydens, 2004; V. Vapnik & Vapnik, 1998; V. N. Vapnik, 1999).

Chapter Summary

This chapter reviewed the literature on spectroscopy with emphasis on fluorescence and infrared spectroscopy. The Phyto-constituents found in medicinal plants are outlined and finally the theories involved in the multivariate data analysis discussed.

CHAPTER THREE

MATERIALS AND METHOD

Introduction

This chapter is divided into three sections. The first section describes how the Anti-Malarial Herbal Plants (AMHPs) samples were obtained and prepared for measurement. In the second section, two optical spectroscopic measurement techniques: Laser-Induced Fluorescence (LIF) and Attenuated Total Reflectance-Fourier Transform Infrared (ATR-FTIR) applied to the AMHPs samples are described. The procedures used in determining the primary, secondary, and micro-nutrients for each of the soil samples is described in the third section.

How the Anti-Malarial Herbal Plants (AMHPs) Sample were obtained and Prepared for Measurements

The Anti-Malarial Herbal Plants (AMHPs) samples were collected from four locations in the Cape Coast metropolis: Abrafo (A), Nfuom (N), and Jukwa (J), close to the Kakum National Park, and Akotokyere (Ak), a community close to the University of Cape Coast. Ten (10) selected AMHPs samples (Table 4) were hand-picked from each of the four (4) locations making a total of forty (40) AMHPs samples used in the study. These samples were collected in March 2016, and was authenticated by comparison with herbarium vouchers: Woody Plants of Ghana (Irvine, 1961), and Herbs of Ghana (Dokosi, 1998), by botanist at the herbarium section of the School of Biological Sciences, College of Agriculture and Natural Sciences, University of Cape Coast.

Table 4: The Authenticated AMHPs Sample and parts used for the Study

Botanical name	Specie ID	Family	Local name	Part used	Reference
Alstonia boonei De Wild	AB	Apocynaceae	Nyamedua	Stem bark	Adebayo and Krettli (2011); Asase, Hesse, and Simmonds (2012)
Acanthospermum hispidum DC	AH	Compositae	Patakoensai	Whole plant	Asase, Akwetey, and Achel (2010)
Azadirachta indica A. Juss	AI	Meliaceae	Abodua	Leaves	Asase et al. (2010)
Cassia occidentalis Linn	CO	Caesalpinaceae	Denkyenhwee	Leaves	Komlaga et al. (2015); Asase, Oteng-Yeboah, Odamtten, and Simmonds (2005)
Mangifera indica Linn	MI	Anacardiaceae	Mango	Leaves	Asase et al. (2010); Asase et al. (2012)
Morinda lucida Linn	ML	Rubiaceae	Konkroma	Leaves	Asase et al. (2010)
Paullinia pinnata Linn	PP	Sapindaceae	Akronkronduawa	Leaves	Asase et al. (2005)
Ricinus communis Linn	RC	Euphorbiaceae	Adendenkruma	Leaves	Nguta, Mbaria, Gakuya, Gathumbi, and Kiama (2010)
Rauvolfia vomitoria Afz	RV	Apocynaceae	Kakapenpen	Leaves	Zirihi, Mambu, Guédé-Guina, Bodo, and Grellier (2005); Asase et al. (2012)
Vernonia amygdalina Linn	VA	Compositae	Bonwene	Leaves	Asase et al. (2005); Adebayo and Krettli (2011)

The AMHPs samples were washed under running tap water to eliminate dust, dirt, and possible parasite. Herbarium specimen was prepared and a picture for each of the AMHPs was taken using TECNO Camon phone. Afterwards, it was dried for three weeks at room temperature in a well spacious ventilated room with no direct sunlight entering the room and then pulverised using a commercial blender (KINEMATICA M20 S). Each pulverised AMHPs samples were kept in a zip-lock bag and labelled.

Botanical Description of the AMHPs Sample

Alstonia Boonei De Wild

Alstonia boonei De wild is a tropical deciduous tree that belongs to the family Apocynaceae. The tree can reach a height of 45 *m* and 3 *m* in girth. It has straight bole, leaf shape oblanceolate, with apex rounded to accuminate. It has numerous lateral nerves. Influorescence corymbiform; flowers yellowish, fragrant. Fruits are paired with slender follicles up to 16 *cm* long (Irvine, 1961; Iwu, 2014; Mshana, 2000; Ross, 2003) (Plate 1).

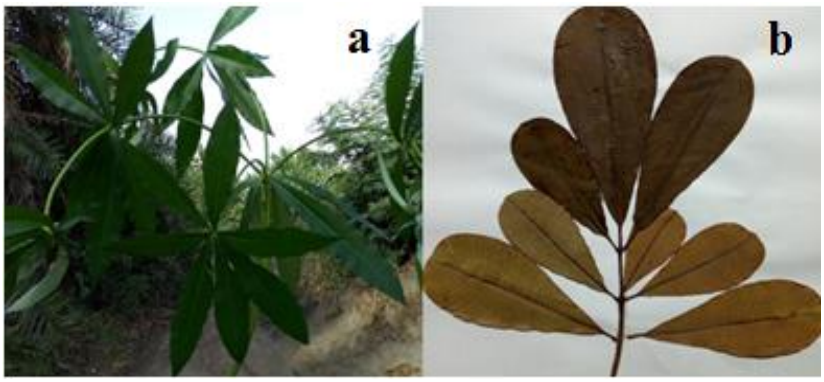

Plate 1: Alstonia Boonei de Wild (Nyamedua) (a) Fresh Leaves (b) Herbarium Specimen

Acanthospermum Hispidum DC.

Acanthospermum hispidum DC is an annual herbaceous plant with hairy stem; having many branches up to 80 *cm* high. The leaves are sessile, obovate, pubescent on both sides. Influorescence axillary, solitary; flowers yellow and the fruit are composed of 5 bright achenes (Dokosi, 1998; Mshana, 2000) (Plate 2)

Plate 2: Acanthospermum Hispidum DC (Patakoensai) (a) Fresh Leaves (b) Herbarium Specimen

Azadirachta Indica A. Juss

Azadirachta indica A. Juss is a tropical evergreen tree that belong to the family Meliaceae and can grows up to 25 *m* high. The tree has a rough dark brown bark with longitudinal fissures which is separated by flat ridges. Leaves are compound, imparipinnate, comprising each 5-15 leaflets. The tree bears many flowered panicles, mostly in the leaf-axils. The sepals are ovate and about 1 *cm* long with sweet scented white oblanceolate petals. The tree has a yellow drupe that are ellipsoid and glabrous (Irvine, 1961; Mshana, 2000; Ross, 2001) (Plate 3)

Plate 3: Azadirachta Indica A. Juss (Abodua) (a) Fresh Leaves (b) Herbarium Specimen

Cassia Occidentalis Linn

Cassia occidentalis Linn is a sub-shrub which grows at a height of 1 *cm*. They spread across all inter-tropical Africa, near dwelling locations. The leaves are composite, usually paripinnate with 5-8 pairs of ovate leaflets and the flowers are yellow, in axillary or terminal short clusters. The pods are narrow, flat, slightly arched, 15 *cm* long with 10-15 seeds (Irvine, 1961; Mshana, 2000) (Plate 4).

Plate 4: Cassia Occidentalis Linn (Denkyenhwee) (a) Fresh Leaves (b) herbarium Specimen

Mangifera Indica Linn

The tree belongs to the Anacardiaceae family varying in size according to the variety and can reach a height of 30 *m.* The tree has a heavy-branched stout trunk. The leaves are arranged spirally on the branches, lanceolate-elliptical, pointed at both ends and the blades are mostly about 25 *cm* long and 8 *cm* wide, with much larger, reddish, and thinly flaccid when first formed. Influorescences are large terminal panicles of small polygamous, fragrant, yellow to pinkish flowers. Fruit is an ovate drupe, slightly reniform with more or less fibrous pulp depending on the varieties (Irvine, 1961; Mshana, 2000; Ross, 2003) (Plate 5).

Plate 5: Mangifera Indica Linn (Mango) (a) Fresh Leaves (b) Herbarium Specimen

Morinda Lucida Benth

Morinda lucida is a medium-size tree up to 15 *m* high. The tree has a slender branchlets and a dense crown. The leaves are broadly elliptical to broadly ovate, acuminate, and entire, 10 × 15 high. The base is rounded to broadly cuneate and often dark purplish or black when dry. The tree produces

white flowers in January-July and September-October. It fruits in March-April (Irvine, 1961; Iwu, 2014; Mshana, 2000) (Plate 6).

Plate 6: Morinda Lucida Benth (Konkroma) (a) Fresh Leaves (b) Herbarium Specimen

Paullinia Pinnata Linn

Paullinia pinnata Linn is a woody climber with tendrils up to 3 *cm* high; branchlets softly pubescent to nealy glabrous, ribbed; leaves imparipinnate; rachis conspicuously winged. Leaflets opposite, oblong to obovate, rather coursely and remotely coursely and remotely toothed, glabrous to pubescence below and with hairy pits in the axil of the nerves; influorescence racemose, peduncle axillary, stout with one or two spirally coiled tendrils at the apex; capsules woody, turbinate, slightly 3 lobed at the top, shortly beaked, about 3 *cm* long, greenish at first, red when ripe (Irvine, 1961; Mshana, 2000) (Plate 7).

Ricinus Communis Linn

Ricinus communis Linn is a perennial shrub up to 3 *m* high, branchy at the base. The leaves are alternate, dark green or red, on long leafstalk, and

palmatilobate with 7 dentate glandular lobes. The male and female flowers are borne separately. The fruits occur as spiny capsules containing 3 arillated seeds. The seeds are rounded, oblong, and somewhat flattened surface from 8 to 12 *mm* long, 6 to 9 *mm* wide, and 4 to 8 *mm* tick (Iwu, 2014) (Plate 8).

Plate 7: Paullinia Pinnata Linn (Akronkronduawa) (a) Fresh Leaves
(b) Herbarium Specimen

Plate 8: Ricinus Communis Linn (Adendenkruma) (a) Fresh Leaves
(b) Herbarium Specimen

Rauvolfia Vomitoria Afz

Rauvolfia vomitoria Afz is shrub that can grow up to 15 *m* in height. It belongs to the Apocynaceae family. It has simple, whorled leaves in groups of

4 or 5. The leaves are widely lanceolate and acuminate, with petioles 8-25 *cm* long and shadowy prooved above. The margins are entire; the base is cuneate, with shiny green upper surface, and dull medium green below; the midrib is impressed above and are 8-16 pairs of major lateral veins. The flowers are small, white, fragrant; fruits spherical with 1 or 2 free carpels, 0.7-1 *cm* long, red or orange at maturity (Irvine, 1961; Iwu, 2014; Mshana, 2000) (Plate 9).

Plate 9: Rauvolfia Vomitoria Afz (Kakapenpen) (a) Fresh Leaves (b) Herbarium Specimen

Vernonia Amygdalina Del

Vernonia amygdalina Del is a small shrub 5 *m* high that grows in tropical Africa. The leaves (15 × 5 *cm*) are simple, obovate-oblanceolate, finely glandular below, and displaying few lateral nerves. The flowers occur in copious corymbose panicles and are white, fragrant, and usually bee infected (Irvine, 1961; Mshana, 2000) (Plate 10).

Plate 10: Vernonia Amygdalina Linn (Bonwene) (a) Fresh Leaves (b) Herbarium Specimen

Laser-Induced Fluorescence (LIF) Measurement Set-up

The Laser-Induced Fluorescence (LIF) measurement Set-up (Figure 19) is a system that consists of three major components. These components are the light source, the optical components, and the detecting system. The light source is made up of a 445 *nm* diode laser (Laser module, China). The optical components consist of a 2-*inch* plane mirror, microscope objective (040AS016 MELLES GRIOT, USA), fibre port micro-positioner (PAF-SMA-5-B, Thorlabs, USA), and bifurcated optical fibre (Ocean Optics, USA). The detecting system consist of a spectrometer (USB 2000, Ocean Optics, USA) and a 450 *nm* cut-off long pass filter. Other components in the LIF measurement Set-up in figure 19 are the sample holder (evaporating disc) and a laptop (ThinkPad T420, Intel (R) Core (TM) i5-250M CPU@ 2.50 GHz processor, 8.00 GB RAM) that is used to operate and visualize the fluorescence emission spectra. Plate 11 shows the picture of the LIF measurement Set-up.

A 445 *nm* continuous wave (CW) diode laser with a maximum power of 100 *m*W was incident on a 2-*inch* plane mirror place at 45^{o} to the incident beam.

This reflected the beam into a 40X microscope objective (NA=0.65). The bifurcated optical fibre with core diameter 600 µ*m* was connected to the fibre port micro-positioner which guided the beam out of the microscope objective. The bifurcated optical fibre consists of two fibres arranged side by side at one end labelled *a* and break out into two arms at the other end with one labelled as *b* which is connected to the fibre port micro-positioner and the other labelled *c* which is connected to the detecting system. The beam was transmitted through *b* to *a* and incident on the sample.

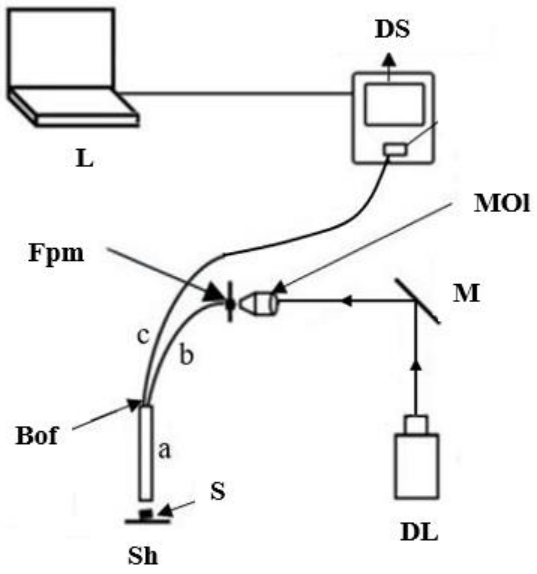

Figure 19**:** Schematic Diagram for the LIF Measurement Set-up of Pulverised AMHPs Sample. DL-445 nm Diode Laser, M-mirror, MOl-Microscope objective, Fpm-Fibre port micro-positioner, Sh-Sample holder**,** S-Sample**,** Bof-Bifurcated optical fibre, DS-Detecting system, L-Laptop.

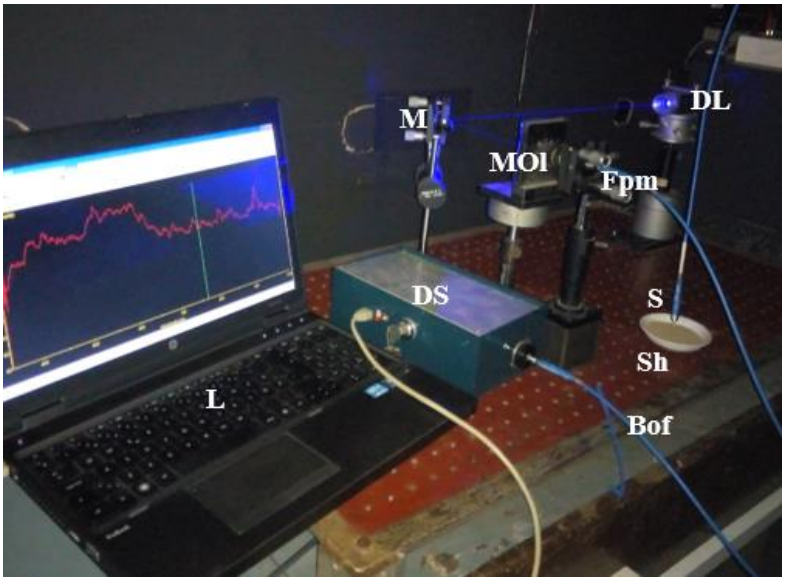

Plate 11: LIF Measurement Set-up. DL-445 nm Diode Laser, M-mirror, Mol-Microscope objective, Fpm-Fibre port micro-positioner, Bof-Bifurcated optical fibre, DS-Detecting system, L-Laptop.

The fluorescence emission spectra together with the excitation wavelength of the diode laser was collected by the fibre through *a* and transmitted through *c* which was connected to the detecting system. The excitation wavelength was cut off by the long pass filter in the detecting system and only the fluorescence emission spectra of the sample was measured and displayed on the laptop. The commercial OO1base software controlling the detecting system allows for fluorescence emission spectra to be saved.

Five (5) grams of Alstonia boonei from Abrafo (ABA(A)) was weighed with a digital precision scale (A&D Instruments (HR-250 AZ)) onto an evaporating disc. The fluorescence emission spectra were measured based on the path of the diode laser described above. The fluorescence measurements for each sample were performed three times in a so-called pseudo-replication procedure, where different sections of the sample were illuminated in each

recording. The process was repeated for all the AMHPs samples and in each case the fluorescence emission spectra measured and recorded.

Infrared Spectra (IR) Measurements of AMHPs Sample

The infrared (IR) spectra for the AMHPs samples were measured using a PerkinElmer Spectrum Two spectrometer (USA) equipped with a universal attenuated total reflectance (UATR) accessory (Plate 12). This instrument is a powerful, compact, easy to use, and robust instrument used for measuring the infrared spectra of compounds (solids, powders, pastes, gels, and liquids). This instrument consists of an optical system and a computer for instrument control and data visualization.

The spectrum two software was set to acquire the infrared spectra at a resolution of 1 cm^{-1} from an average of 32 scans. Measurement was taken first by taking the background spectrum of the diamond attenuated total reflection (ATR) (single reflection) plate (0.4 cm × 3.0 cm) and saved as the background spectrum. Five (5) milligram of Alstonia boonei (AB(A)) from Abrafo was placed on the diamond plate, and its spectrum also measured. This was saved as the sample spectrum. The spectrum two software generates the absorption spectrum of the AB(A) sample which gives a change in intensity at each frequency. The process was repeated for all the other AMHPs samples from the different locations.

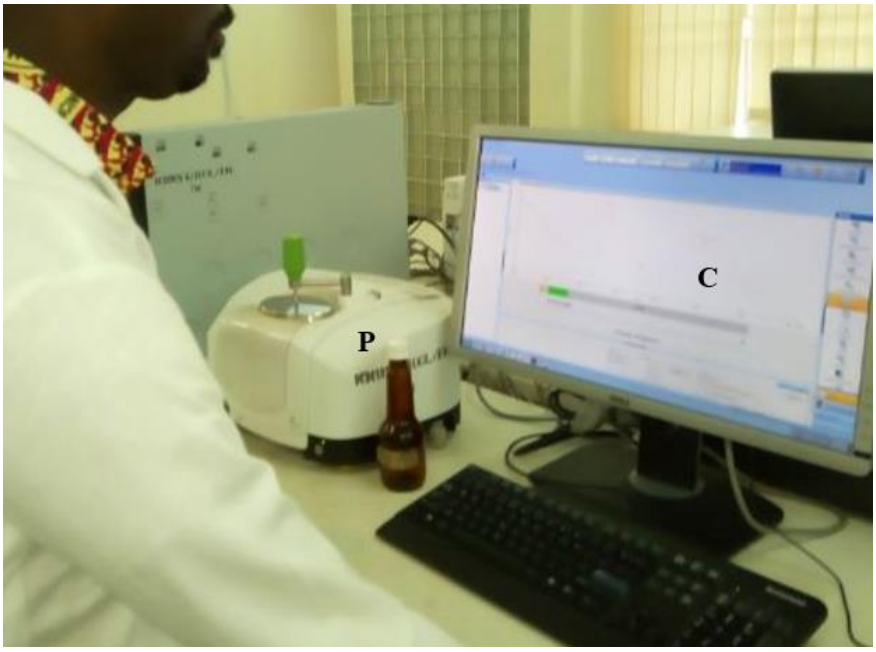

Plate 12: PerkinElmer Spectrum Two Spectrometer. P-Spectrometer, C-Computer.

Collection and Preparation of Soil Samples

The soil sampling design employed in this study was a systematic sampling using a 30 *cm* × 30 *cm* diamond grid (Gregorich & Carter, 2007). With the aid of an auger, a depth of 0-15 *cm*, representing Top soil and 15-30 *cm*, representing Sub soil (Table 5) were collected from the four (4) different locations and brought to the laboratory. Five (5) different diamond grid (30 *cm* × 30 *cm*) within a location was sampled for the soil. The same process was repeated for the other locations. The samples were dried at a room temperature. This was done to reduce the moisture content of the soil samples. To obtain a uniform soil particle size, the soil samples were sieved using a 2 *mm* mesh. They were placed in a zip-lock bag and labelled for later use.

Table 5: Soil Samples and Nomenclature used

Name	Nomenclature	No of replicates
Akotokyere-Top Soil	Ak-TS	5
Akotokyere -Sub Soil	Ak-SS	5
Jukwa-Top Soil	J-TS	5
Jukwa-Sub Soil	J-SS	5
Abrafo-Top Soil	A-TS	5
Abrafo-Sub Soil	A-SS	5
Nfuom-Top Soil	N-TS	5
Nfuom-Sub Soil	N-SS	5

Measurement of Soil Potential of Hydrogen (pH)

The potential of hydrogen (pH) of the soil samples were measured using a pH meter (Eutech PC450). The pH meter was first calibrated using two buffer solutions with pH readings of 4 and 7. Ten (10) grams of the soil sample collected from Akotokyere-Top soil (Ak-TS) was weighed with a digital precision scale (A&D Instruments (HR-250 AZ)) and placed into a 50 *ml* translucent bottle with a screw cap. 25 *ml* of distilled water was added to it and shaken for 15 min. using a laboratory oscillating shaker. The pH of the soil sample was measured and recorded by inserting the electrode of the pH meter into the translucent bottle. The process was repeated for the other soil samples from the other locations. The pH of each soil sample was measured five times and then averaged.

Soil Texture

In determining the soil texture of the soil, the following processes were followed: removal and dispersion of the organic matter of the soil, sampling the silt and clay, sampling the clay, and sampling the sand.

Removal and Dispersion of Organic Matter of the Soil

Ten (10) grams of the soil sample from Akotokyere-Top soil (Ak-TS) was weighed into a 500 *ml* beaker. 125 *ml* of distilled water was added and the mixture swirled thoroughly. 20 *ml* of 30 % hydrogen peroxide (H_2O_2) was added to the soil mixture, and gently swirled. This was done to destroy the organic matter that binds the mineral particles, and also hinders soil dispersion. Two drops of amyl alcohol ($C_2H_{11}OH$) was added to the mixture in order to reduce frothing. The mixture was allowed to stand for some time until frothing had ceased (Avery & Bascomb, 1974). When no reaction appears to occur, the mixture was heated with occasional stirring to break the froth. Finally, the mixture was allowed to boil for about fifteen to twenty minutes to complete the destruction of the organic matter and later allowed to cool.

The mixture was transferred into a heat-resistant screw lid bottle and 2 *g* of sodium hexametaphosphate $(Na_2PO_3)_6$ was added and topped to the 250 *ml* mark. It was shaken with the laboratory oscillatory shaker for 18 *hrs*. The content was transferred into a 500 *ml* sedimentation cylinder and topped up with distilled water to the 500 *ml* mark. The sedimentation cylinder was closed with a cork and shaken vigorously. Plate 13 shows the soil texture apparatus used.

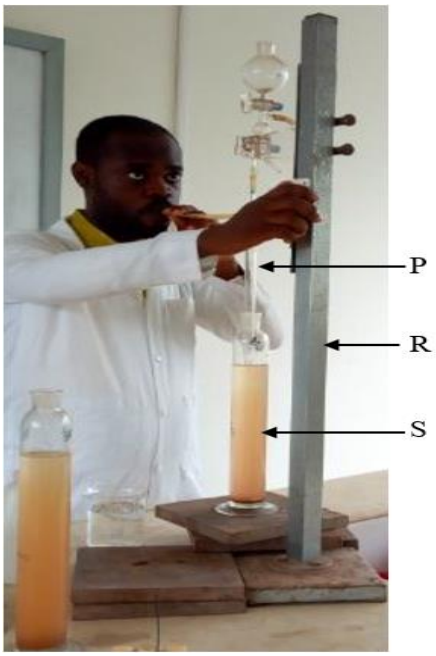

Plate 13: Soil Texture Apparatus. P-Pipette, R-Retort stand, S-Sample.

Sampling the Silt and Clay

The mixture in the sedimentation cylinder was stirred by placing the hand over the top and shaking it thoroughly for 30 *s*. The mixture was allowed to settle for 32 *s*. The assumption was that all the sand particles would have sank to the base of the sedimentation cylinder after the 32 *s*. The pipette was lowered gently into the soil mixture contained in the sedimentation cylinder at a depth of 10 *cm*. 20 *ml* of the soil suspension was drawn using the pipette and transferred into a weighed 25 *ml* beaker, dried at 105^{o}*C*, cooled in a desiccator, and reweighed. The mass of the silt and clay in 25 *ml* was calculated and labelled as *d*.

Sampling the Clay

The sedimentation cylinder was allowed to stand undisturbed for another 8 *hrs*. At this time, all the sand particles would have deposited at the base of the

sedimentation cylinder. The pipette was lowered into the sedimentation cylinder at a depth of 10 *cm*, and 20 *ml* of the soil suspension was pipetted into a weighed 25 *ml* beaker, dried at 105^{o}C, cooled in a desiccator, and reweighed. The mass of clay in 25 *ml* was calculated and labelled as *e*.

Sampling the Sand

In order to sample the sand content of the mixture, the sedimentation cylinder was left undisturbed for another 8 *hrs*. The solution portion was then poured away, and the remaining sediments transferred into a beaker. Distilled water was added, swirled, and decanted. The process was repeated several times by stirring, settling, and decanting until the supernatant became clear. This was done to remove the excess silt and clay in the sand. The sand was transferred into a weighed 25 *ml* beaker, dried at 105^{o}C, cooled in a desiccator and reweighed. The mass of sand in 500 *ml* calculated and labelled as *g*. The removal of organic matter and dispersion of soil mixture, sampling the silt and clay, sampling the clay, and sampling the sand was repeated for all the other soil samples from the different locations.

Calculations

The percentage mass of silt, clay, and sand was calculated from the sampling of silt and clay, sampling of clay, and sampling of sand as follows: $d =$ mass of silt and clay in $25\,ml$, $e =$ mass of clay in $25\,ml$, f (mass of silt in $25\,ml$) $= d - e$, and $g =$ mass of sand in $500\,ml$. Since e and f was pipetted into $25\,ml$ from the $500\,ml$ sedimentation cylinder, then, the mass of e and f had to be converted to h and i in $500\,ml$. Therefore,

$$h = \frac{(e \text{ in } 25\,ml \times 500\,ml)}{25\,ml} \tag{42}$$

$$i = \frac{(f \text{ in } 25\,ml \times 500\,ml)}{25\,ml} \tag{43}$$

Now, the mass of silt in $500\,ml$, the mass of clay in $500\,ml$, and the mass of sand in $500\,ml$ was converted to the percentage as shown in equations 44 – 46.

$$\% \text{ mass of silt} = \frac{i}{g+h+i} \times 100 \tag{44}$$

$$\% \text{ mass of clay} = \frac{h}{g+h+i} \times 100 \tag{45}$$

$$\% \text{ mass of sand} = \frac{g}{g+h+i} \times 100 \tag{46}$$

The different percentage masses obtained was compared with the United States Department of Agriculture (USDA) textual class to determine the soil texture for each of the soil samples.

Soil Texture Determination using the Textural Triangle

The textural triangle used to determine the textural classes of the soil samples is shown in figure 20. Each side of the triangle corresponds to a percentage of soil separates: clay, silt and sand. The textural triangle consists of twelve textural classes. Within the triangle are series of gridlines that helps to determine the textural class from the percentage of soil separate. The soil textural triangle is read by reading from figure 20 the soil separate, % from the

bottom of the triangle from left to right. The clay separate, % from the left side of the textural triangle from the bottom down to up, and finally, the silt separate, % from up to down. The intersection of the various soil separates as shown with the coloured arrows determines the texture of the soil. For example, if the soil is composed of 37 % of sand, 22 % of clay, and 41 % of silt (using the coloured arrows as a guide), then the soil is considered as a loam.

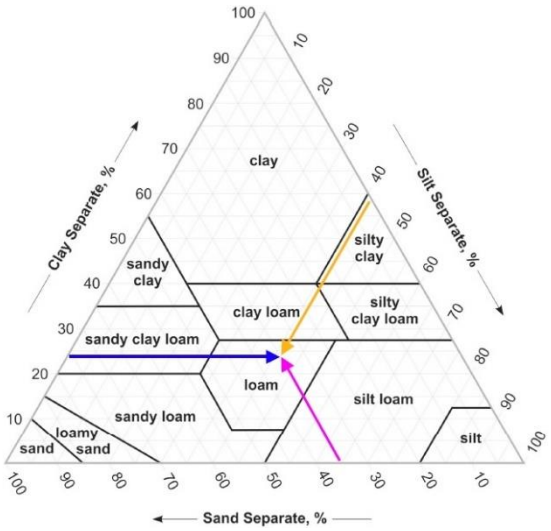

Figure 20: Soil Textural Triangle with each side corresponding to a percentage of Soil Separate. The pink arrow represents the direction in which one reads the Sand Separate, the blue arrow corresponds to the clay separate, and the orange arrow corresponds to the Silt Separate (USDA System)

Preparation of Sample Solution for the Determination of nitrogen N, potassium K, phosphorus P, calcium Ca, magnesium Mg, zinc Zn, copper Cu, iron Fe for the Soil Samples

The preparation of the sample solutions for the determination of nitrogen *N*, potassium *K*, phosphorus *P*, calcium *Ca*, magnesium *Mg*, zinc *Zn*, copper *Cu*, iron *Fe* for the soil samples were carried out first by the oxidation process. This ensured that the organic matter was destroyed through acid oxidation.

Sulphuric Acid-Hydrogen Peroxide Digestion

The digestion mixture comprised of 350 *ml* of hydrogen peroxide, 0.42 *g* of selenium powder, 14 *g* of lithium sulfate, and 420 *ml* of sulphuric acid. 0.5 *g* of the soil samples were weighed into a 100 *ml* Kjedahl flask and 4.4 *ml* of the digestion mixture was added. The soil samples were digested at 360 ^{o}C for 2 *hrs.* Blank digestion (digestion of the digestion mixture without the sample) were carried out the same as the soil samples (Allen, Grimshaw, Parkinson, & Quarmby, 1974). After the digestion, the digests (blank and soil sample) were transferred into a 50 *ml* volumetric flask and made up to the volume with distilled water. The blank and soil sample digest were used in the determination of the primary, secondary, and micro nutrients.

Determination of nitrogen N content in Soil using Micro-Kjedahl Method

The steam distillation apparatus (Plate 14) was flushed by passing steam through it for 20 min. 50 *ml* Erlenmeyer flask was placed under the condenser of the distillation apparatus. 20 *ml* of the aliquot was pipetted from a 50 *ml* soil

sample digest (solution volume) and transferred into the reaction chamber through the trap funnel.

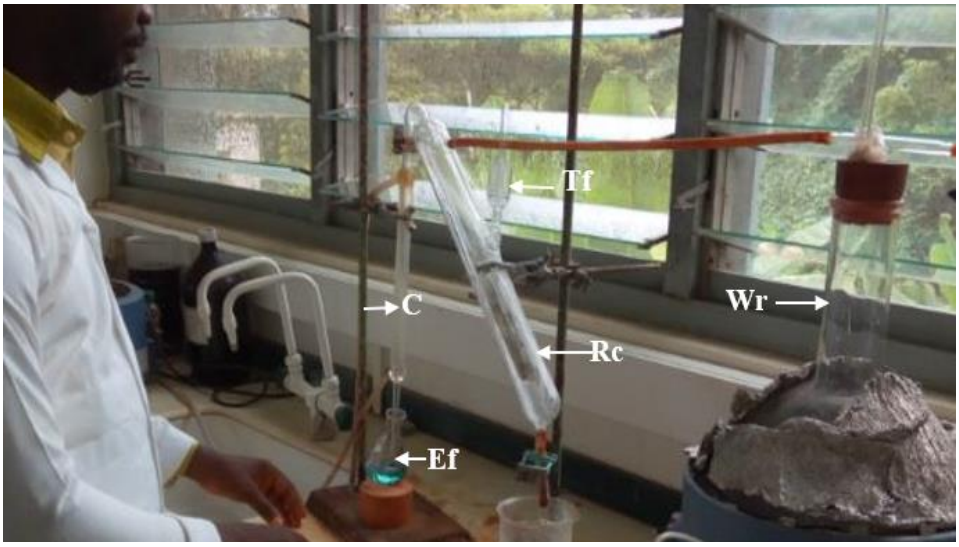

Plate 14: The Steam Distillation Apparatus. Tf-Trap funnel, Wr-Water reservoir, Rc-Reaction chamber, C-Condenser, Ef-Erlenmeyer flask.

5 *ml* of boric acid as an indicator was transferred into the reaction chamber containing the soil digest. The distillate was collected into a 50 *ml* Erlenmeyer flask and titrated against 1/140 *M HCl.* The titre value (S) was recorded when the colour of the distillate changed from wine-red to green. The blank was treated the same way, and its titre value (B) subtracted from the soil samples titre value. The percentage of nitrogen N was calculated using equation 47 for the soil samples (Allen et al., 1974).

$$N\ (\%) = \frac{(S - B) \times solution\ volume}{10^2 \times aliquot \times Sample\ weight} \qquad (47)$$

where *S* and *B* are the sample and blank titre values respectively.

Preparation of Reagent A and B used in the Determination of Available phosphorus P in the Soil Samples

The determination of available phosphorus *P* in the soil samples was determined first by preparing these two reagents (A and B). Reagent A was prepared by mixing three solutions. Solutions one was prepared by dissolving 12 *g* of ammonium molybdate in 250 *ml* of distilled water. Solution two was also prepared by dissolving 0.2908 *g* of potassium antimony tartarate in 100 *ml* of distilled water. Finally, 2.5 *M* H_2SO_4 was prepared by diluting approximately 148 *ml* of concentrated H_2SO_4 in about 1 *L* of distilled water making the third solution. The three solutions were mixed together in a 2 *L* volumetric flask and made up to the volume with distilled water. Reagent B was also prepared by dissolving 1.056 *g* of ascorbic acid in 200 *ml* of Reagent A.

Preparation of the Standard phosphorus P Solution from the Stock Solution

A stock solution of 100 *µg/ml* was prepared from reagent B. 5 *µg/ml* was prepared from the stock solution from which seven working standards of phosphorus *P* (0, 0.1, 0.2, 0.4, 0.6, 0.8, and 1.0 *µg/ml*) were prepared in 25 *ml* volumetric flasks.

Calorimetric Determination of Available phosphorus P Concentration in Soil Samples using Bray No. 1 Method and Ascorbic acid

2 *ml* aliquot of the soil sample digest was pipetted into a 25 *ml* volumetric flask. 10 *ml* of distilled water was added to the soil samples after which 4 *ml* of reagent B was added and their volumes made up to the 25 *ml* with distilled water

and mixed thoroughly. The flasks were allowed to stand for 15 min for colour development. The absorbances of the standards and soil samples solutions were determined using a visible spectrophotometer (model 721) at a wavelength of 882 *nm*. A calibration curve was plotted using the concentrations and absorbances of the standards solution. The concentrations *P* of the soil samples solutions were extrapolated from the standard curve and calculated using equations 48 and 49 (Allen et al., 1974).

$$P\ (\mu g / g) = \frac{C \times Dilution\ Factor}{Sample\ weight} \tag{48}$$

where

$$C = \frac{gradient\ \ from\ calibration\ curve}{Absorbance\ \ from\ the\ spectrometer} \tag{49}$$

Determination of potassium K Concentration in Soil Samples

Potassium *K* was determined using the flame photometer (Plate 15). The flame photometer was calibrated using six standard solutions (0, 2, 4, 6, 8, 10 µg/ml) of *K* in ammonium acetate solution. The soil samples digest was respectively aspirated into the flame photometer, and their corresponding emissions recorded. A calibration curve was plotted using the concentrations and the emissions of the standard solutions. The concentrations for the soil samples was calculated using equation 50 (Allen et al., 1974)

$$K(\mu g / g) = \frac{C \times 10}{Sample\ weight \times 39.1} \times 390 \tag{50}$$

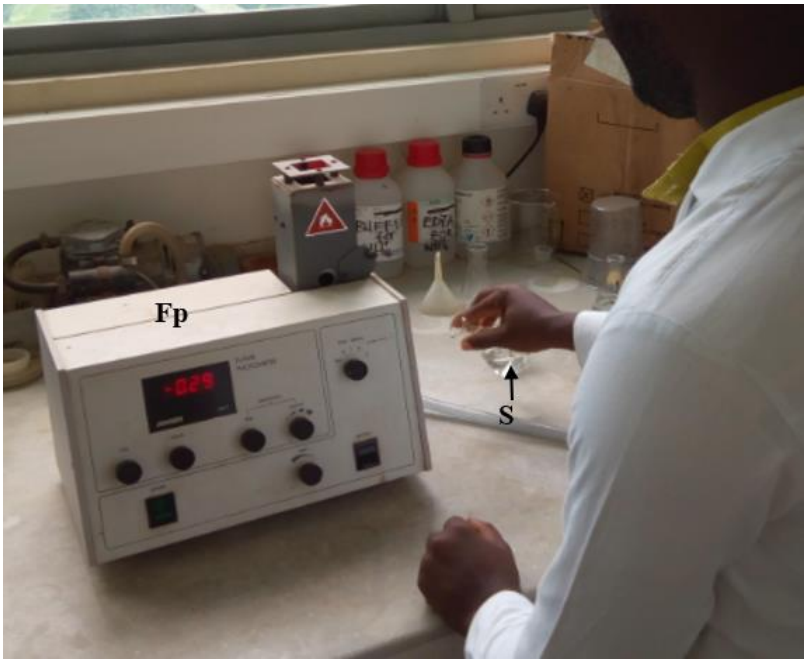

Plate 15: The flame photometer equipment. Fp-Flame photometer, S-Sample.

Determination of magnesium Mg and calcium Ca in Soil Samples by Ethylenediaminetetraacetic acid (EDTA) Titration

The method involved the chelation of cations with Ethylenediaminetetraacetic acid (EDTA). The procedure involved the determination of calcium *Ca* and Magnesium *Mg* together, and the determination of *Ca* alone. *Mg* concentration was found by the difference.

Ca and *Mg* together was determined by placing an aliquot of 10 *ml* of the sample in a 250 *ml* of Erlenmeyer flask, and the solution was diluted to 150 *ml* of distilled water. 15 *ml* of ammonia solution, and 1 *ml* each of potassium cyanide, hydroxylamine, potassium ferro-cyanide, and triethanolamine (TEA) were added to the solution. Five drops of Evichrom Black T (EBT) was added, and the solution was titrated against 0.005 *M v*EDTA. The concentrations of *Ca* and *Mg* was calculated using equations 51 and 52 for the soil samples (Allen et al., 1974).

$$Ca\ (\mu g / g) = \frac{4 \times Titre\ value}{Sample\ weight} \times 200 \quad (51)$$

$$Mg\ (\mu g / g) = \frac{4 \times Titre\ value}{Sample\ weight} \times 120 \quad (52)$$

Determination of iron Fe, copper Cu, and zinc Zn Concentration in the Soil Samples using Atomic Absorption Spectrophotometer (AAS)

Three standard solutions of iron *Fe*, copper *Cu*, and zinc *Zn* with concentrations 0, 1, 2, 5, 10, and 25 $\mu g/ml$ were respectively prepared. The standard solutions were aspirated into the atomic absorption spectrophotometer (AAS) and the concentrations determined. The concentrations were respective plotted as calibration curves on the screen of the AAS for *Fe, Cu,* and *Zn.* The digested soil samples were aspirated into the AAS and their respective concentrations measured and recorded. The concentrations in $\mu g/g$ of the soil samples was calculated using equations 53, 54, and 55 (Allen et al., 1974).

$$Fe\ (\mu g / g) = \frac{C \times solution\ volume}{Sample\ weight} \quad (53)$$

$$Cu\ (\mu g / g) = \frac{C \times solution\ volume}{Sample\ weight} \quad (54)$$

$$Zn\ (\mu g / g) = \frac{C \times solution\ volume}{Sample\ weight} \quad (55)$$

where C is the concentrations obtained from the AAS.

Chapter Summary

This chapter described the location, collection and preparation, the botanical description of the Anti-Malarial Herbal Plants (AMHPs) samples. It then focused on the optical spectroscopic techniques (Laser-Induced Fluorescence (LIF) and the Attenuated Total Reflectance-Fourier Transform Infrared (ATR-FTIR)). Finally, the procedures used in determining the primary, secondary, and micro nutrients of the soil samples was described.

CHAPTER FOUR

RESULTS AND DISCUSSION

Introduction

This chapter is divided into two sections. The first section reports and discusses the results obtained from the two spectroscopic measurements techniques (Laser-Induced Fluorescence (LIF) and the Attenuated Total Reflectance-Fourier Transform Infrared (ATR-FTIR)) of the Anti-Malarial Herbal Plants (AMHPs) samples from the four locations (Abrafo, Jukwa, Nfuom, and Akotokyere). The second section presents results and discussion of the soil texture analysis, potential of hydrogen (pH), the primary, secondary macro-nutrients and micro-nutrients of the soil samples from the same locations.

Results from the Laser-Induced Fluorescence (LIF) Measurements of the Anti-Malarial Herbal Plants (AMHPs) Sample

Plants tissue (leaf, stem bark, flower, roots, etc) contain various substances which are together grouped as primary and secondary metabolites. Primary metabolites are responsible for the nutritional needs of man. Examples are carbohydrates, proteins, vitamins, lipids, etc (Makkar, Siddhuraju, & Becker, 2007; Pengelly, 2004). Secondary metabolites on the other hand were ones regarded as simple waste products of plant's metabolism. They serve as defensive mechanisms to plants. Examples of the secondary metabolites are phenols, alkaloids, terpenes, oils and resins, glycosides, etc (Makkar et al., 2007; Pengelly, 2004). Secondary metabolites when extracted by the appropriate means (Soxhlet extraction, maceration, decoction, infusion, digestion, etc. (Dean, 2010; Pandey, Tripathi, & Phytochemistry, 2014; Ramsey, 2012)) and

purified provides us with the medicinal properties of plants. Irrespective of the part of the plant tissue under study, several of these secondary metabolites may be present. Anti-Malarial Herbal Plants (AMHPs) samples contain these secondary metabolites that are responsible for the Anti-malarial properties of plants.

Laser-induced fluorescence (LIF) emission spectra for six AMHPs samples: Vernonia amygdalina (VA), Acanthospermum hispidum (AH), Azadirachta indica (AI), Cassia occidentalis (CO), Morinda lucida (ML), and Ricinus communis (RC) from four locations: Abrafo (A), Jukwa (J), Nfuom (N), and Akotokyere (Ak) in the Cape Coast Metropolis is shown in figures 21-26. The rest of the AMHPs samples namely, Alstonia boonei (AB), Mangifera indica (MI), Paullinia pinnata (PP), and Rauvolfia vomitoria (RV) is shown in Appendix A. The LIF spectra for the AMHPs samples exhibited two major peak bands (figures 21-26). Peak 1 is within the spectra range of 450-650 *nm* and peak 2 is within the spectra range of 650-800 *nm*. Peak 1 is characterised by the green (490-575 *nm*) and yellow (575-650 *nm*) fluorescence while Peak 2 is characterised by the red to far-red (680-800 *nm*) fluorescence. The fluorescence intensity varied from location to location depending on the AMHPs samples (figures 21-26). For instance, the fluorescence intensity for VA for Akotokyere in figure 21 was high compared with the other locations (Abrafo, Jukwa and Nfuom).

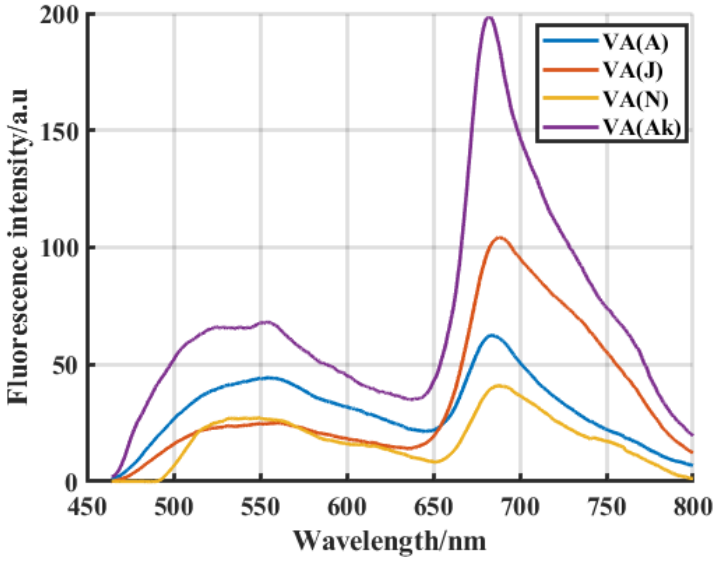

Figure 21: Average LIF Spectra of Pulverised Vernonia Amygdalina (VA) from four Locations: Abrafo (A), Jukwa (J), Nfuom (N), and Akotokyere (Ak)

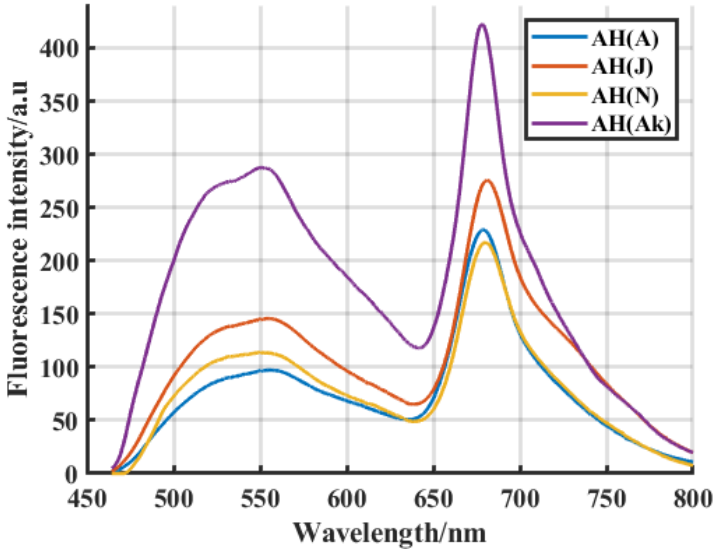

Figure 22: Average LIF Spectra of Pulverised Acanthospermum Hispidum (AH) from four Locations: Abrafo (A), Jukwa (J), Nfuom (N), and Akotokyere (Ak)

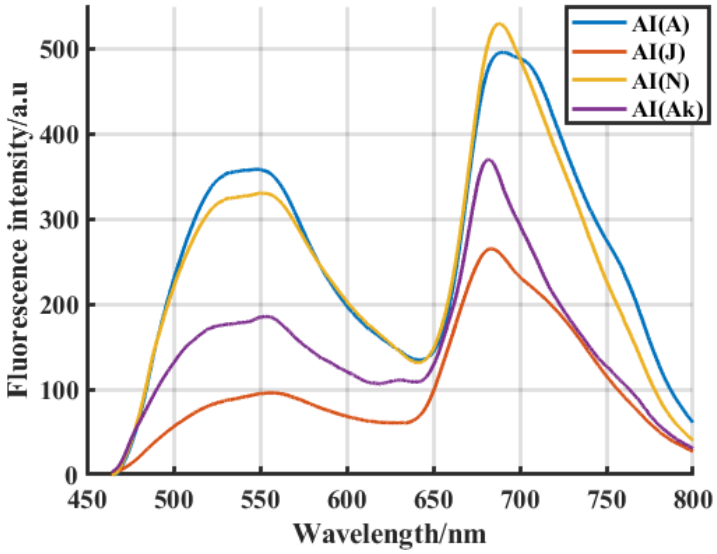

Figure 23: Average LIF Spectra of Pulverised Azadirachta Indica (AI) from four Locations: Abrafo (A), Jukwa (J), Nfuom (N), and Akotokyere (Ak)

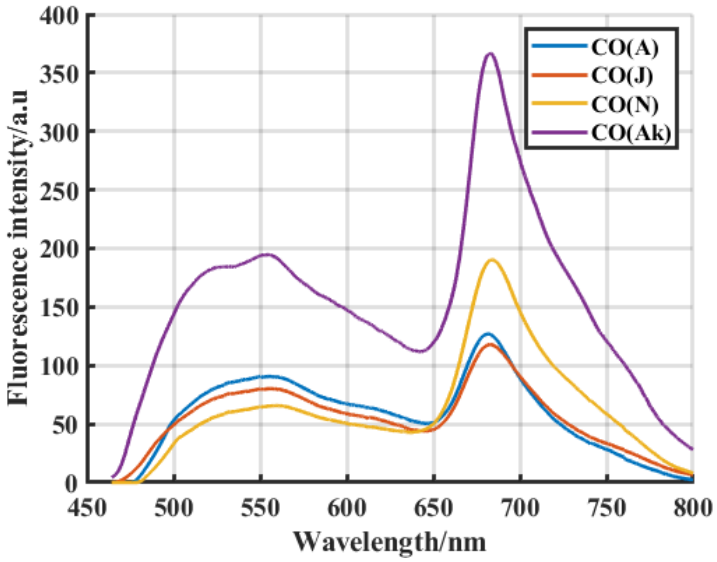

Figure 24: Average LIF Spectra of Pulverised Cassia occidentalis (CO) from four Locations: Abrafo (A), Jukwa (J), Nfuom (N), and Akotokyere (Ak)

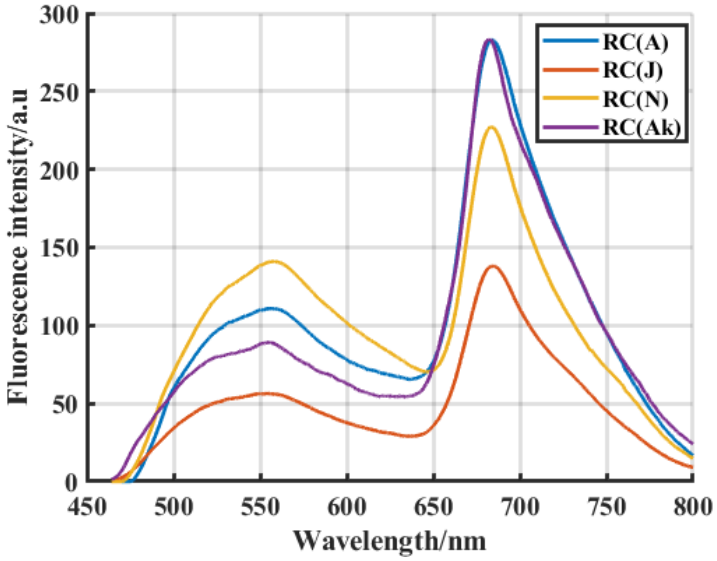

Figure 25: Average LIF spectra of pulverised Ricinus communis (RC) from four locations: Abrafo (A), Jukwa (J), Nfuom (N), and Akotokyere (Ak)

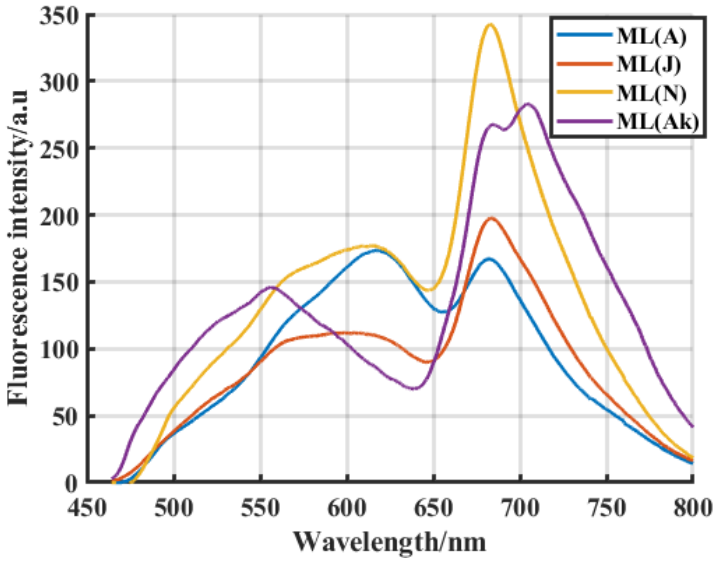

Figure 26: Average LIF spectra of pulverised Morinda lucida (ML) from four locations: Abrafo (A), Jukwa (J), Nfuom (N), and Akotokyere (Ak)

From figures 21-26, it is observed that there are hidden peaks within the LIF spectra for all the AMHPs samples for all the locations, therefore, the LIF spectra were deconvolved using the PeakFit software. Figures 27-32, show the

LIF spectra for 6 AMHPs samples. Superimposed in the respective graphs are the corresponding fitted spectra, the deconvoluted peaks and the coefficient of determination, R^2. The remaining four (4) AMHPs samples are shown in Appendix B. Figure 27 shows the LIF spectra for Vernonia amygdalina for the four locations: VA(A), VA(J), VA(N), and VA(Ak) with the goodness of the fit R^2, respectively as; 0.9983, 0.9994, 0.9928, and 0.9956. This R^2 determines how good the resolved peaks are. There were five (5) peaks hidden within the LIF spectra of VA. Each of the deconvoluted peaks corresponded to a Secondary metabolites or Phyto-constituents present within VA.

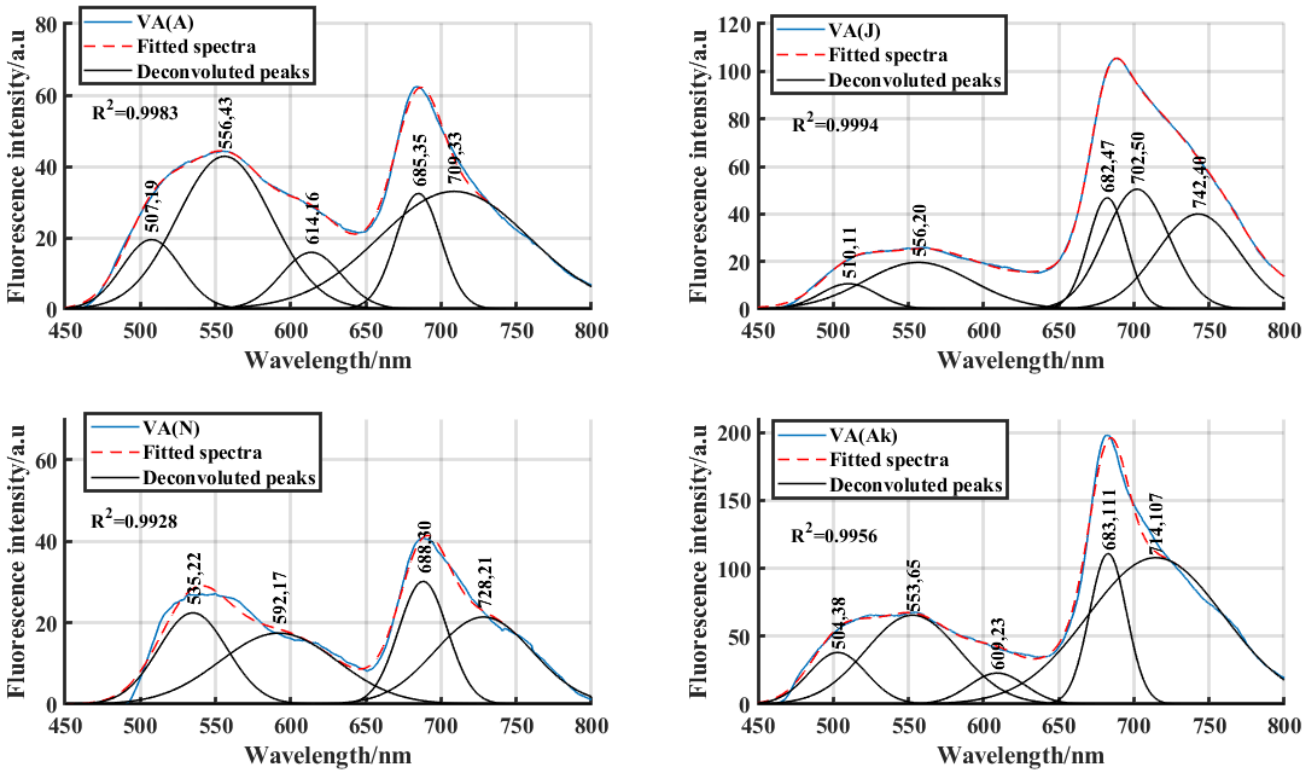

Figure 27: Deconvoluted Average LIF Spectra of Pulverised form of Vernonia Amygdalina (VA) from (a) Abrafo (A) (b) Jukwa (J) (c) Nfuom (N) (d) Akotokyere (Ak) Excited with a $445\,nm$ Diode Laser.

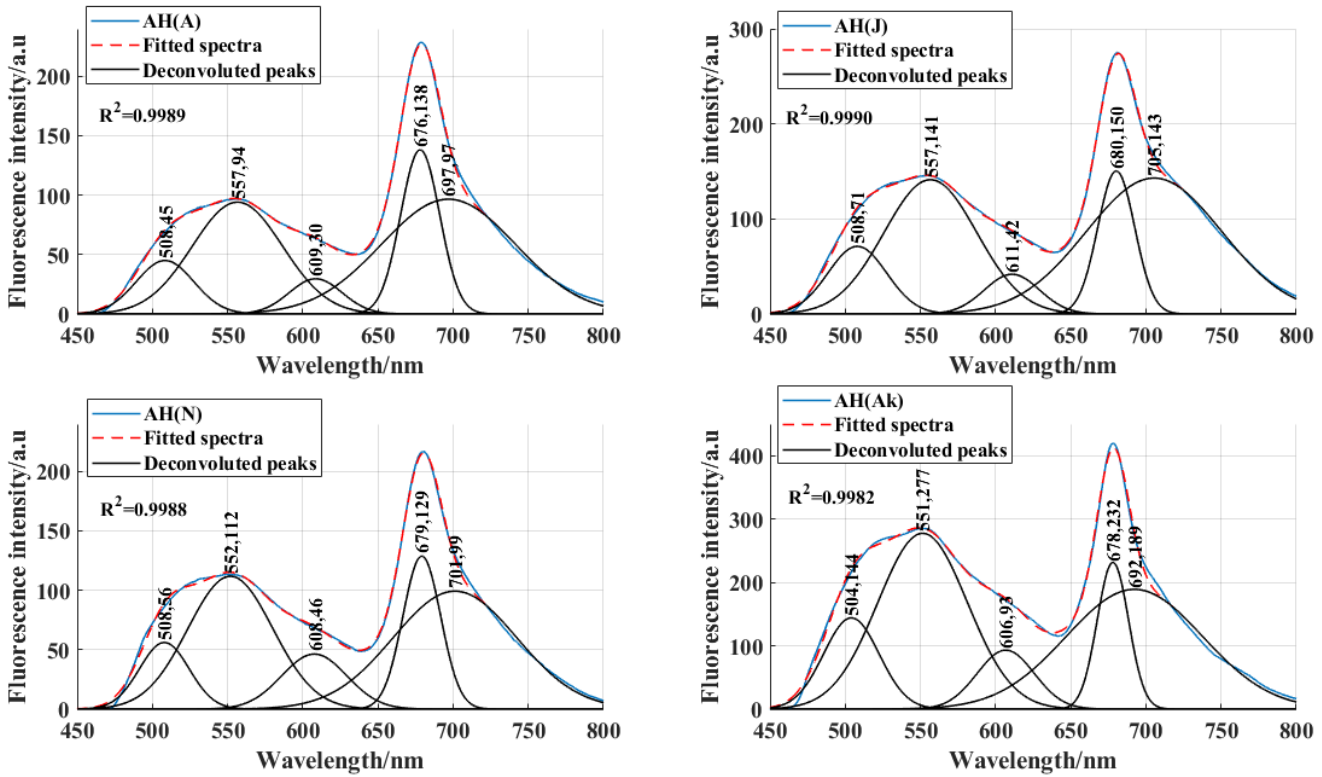

Figure 28: Deconvoluted Average LIF Spectra of pulverised form of Acanthospermum Hispidum (AH) from (a) Abrafo (A) (b) Jukwa (J) (c) Nfuom (N) (d) Akotokyere (Ak) Excited with a 445 *nm* Diode Laser.

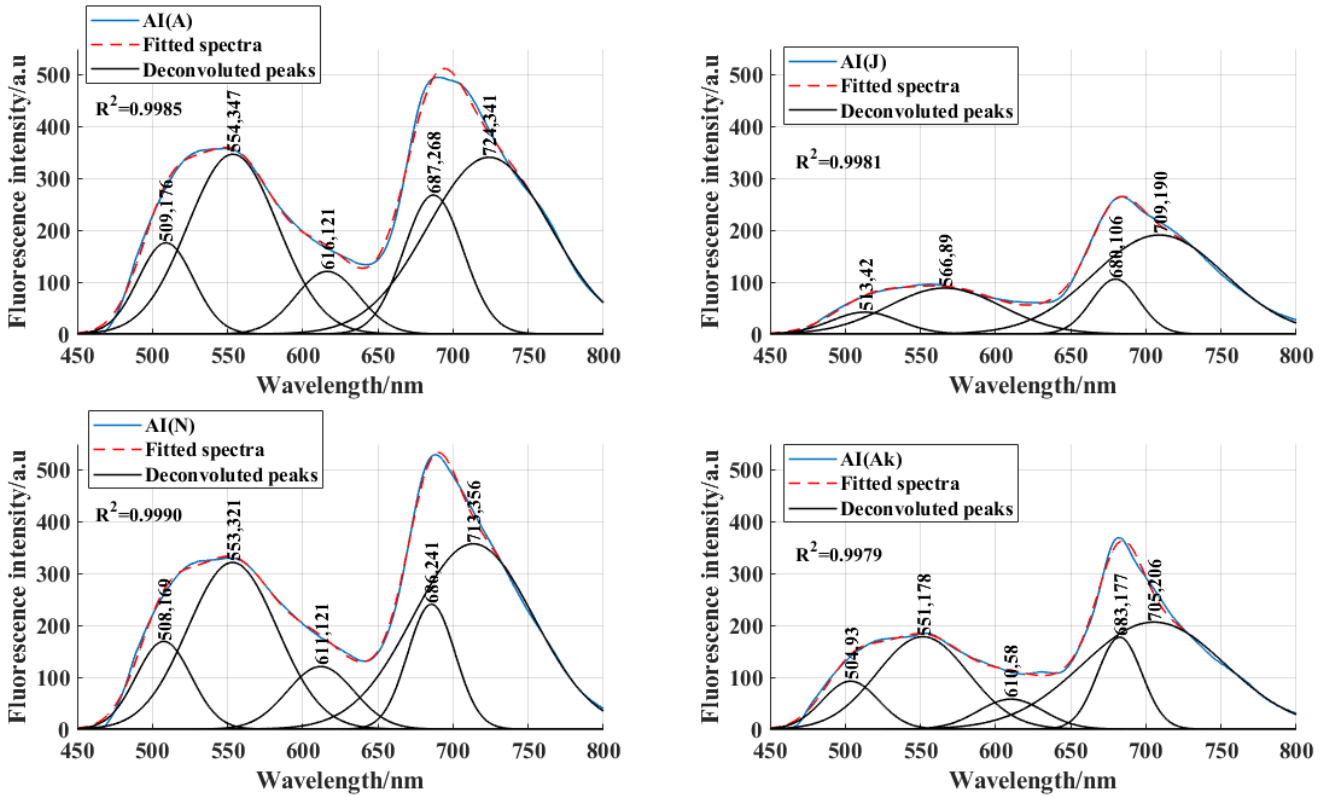

Figure 29: Deconvoluted Average LIF Spectra of Pulverised form of Azadirachta Indica (AI) from (a) Abrafo (A) (b) Jukwa (J) (c) Nfuom (N) (d) Akotokyere (Ak) Excited with a 445 *nm* Diode Laser.

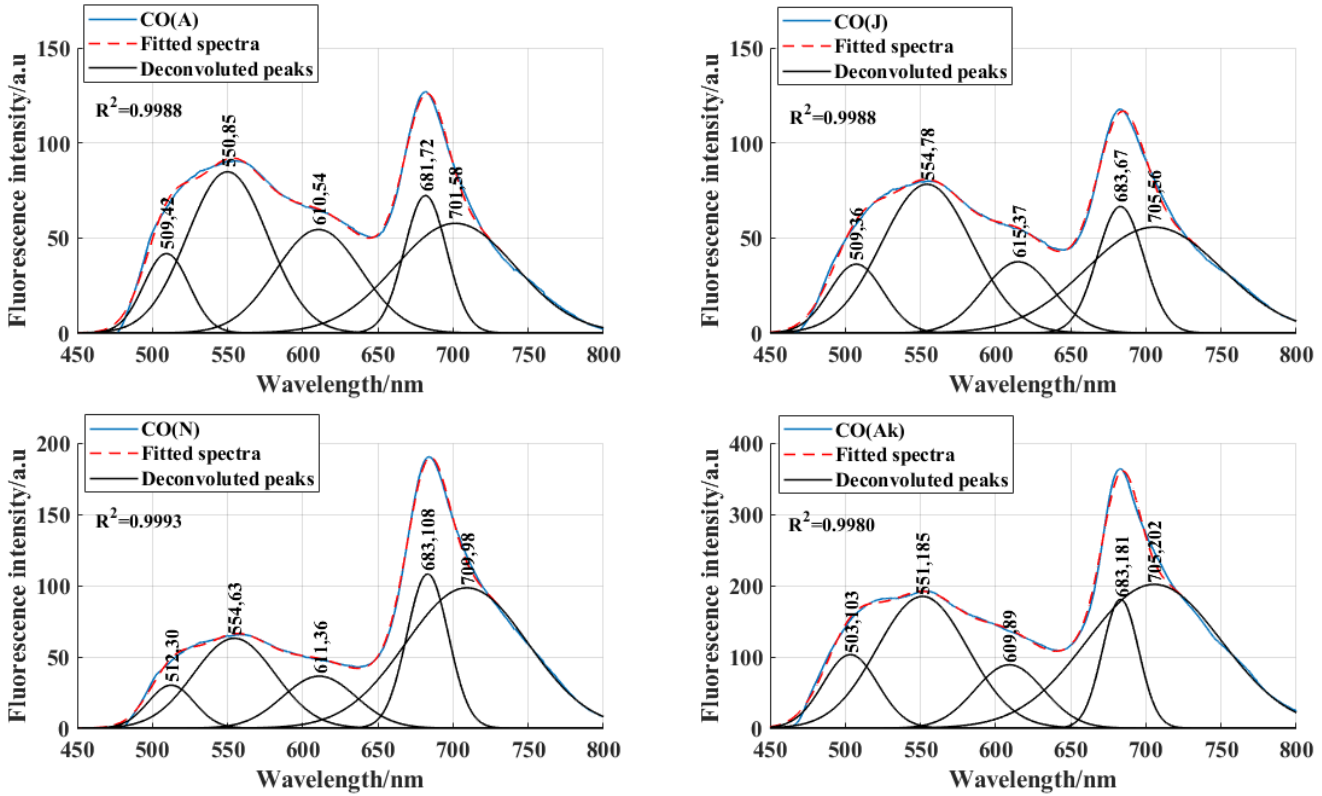

Figure 30: Deconvoluted Average LIF Spectra of Pulverised form of Cassia Occidentalis (CO) from (a) Abrafo (A) (b) Jukwa (J) (c) Nfuom (N) (d) Akotokyere (Ak) Excited with a 445 *nm* Diode Laser.

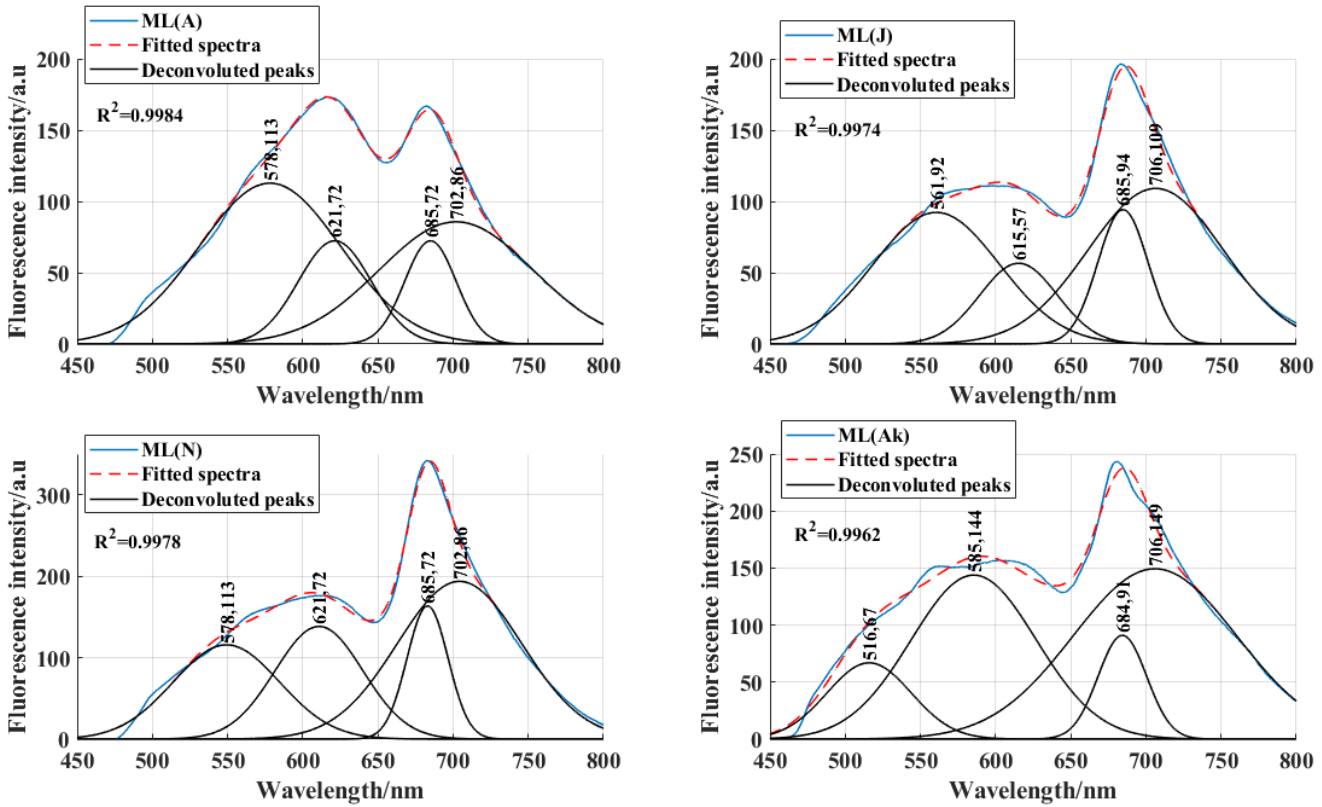

Figure 31: Deconvoluted Average LIF Spectra of Pulverised form of Morinda Lucida (ML) from (a) Abrafo (A) (b) Jukwa (J) (c) Nfuom (N) (d) Akotokyere (Ak) Excited with a 445 *nm* Diode Laser.

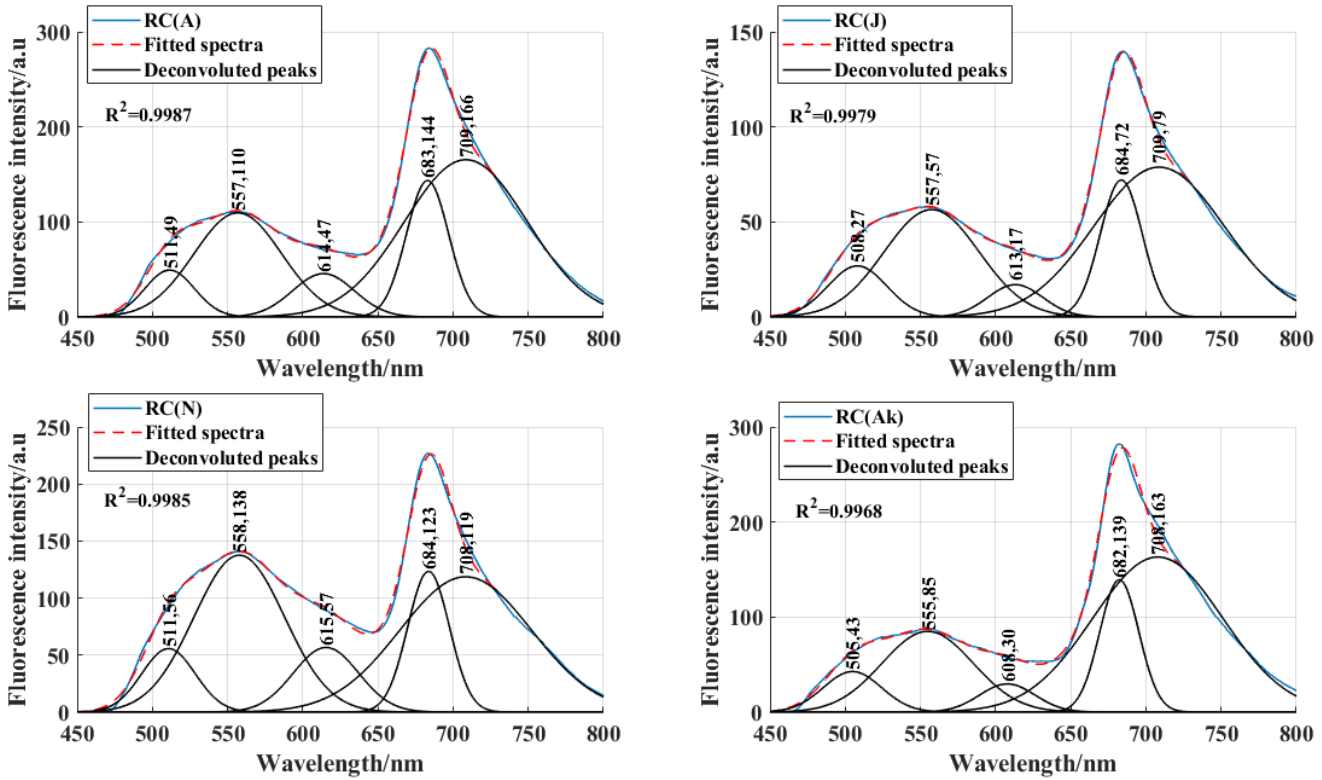

Figure 32: Deconvoluted Average LIF Spectra of Pulverised form of Ricinus Communis (RC) from (a) Abrafo (A) (b) Jukwa (J) (c) Nfuom (N) (d) Akotokyere (Ak) Excited with a 445 *nm* Diode Laser.

The peak observed at $556\,nm$ for VA(A) and VA(J), $535\,nm$ for VA(N), and $553\,nm$ for VA(Ak) may be attributed to the compounds quercetin, berberine, flavonoids, and flavins (Lang, Stober, & Lichtenthaler, 1991; Lichtenthaler, Stober, & Lang, 1992). Berberine and quercetin in combinations with certain compounds (pyrimethamine, chlorine) have proven to be more effective in malaria treatment (Brahmachari, 1944; Dkhil et al., 2015; Kayano et al., 2011; Sheng, Jiddawi, Hong, & Abdulla, 1997). The red fluorescence peak of VA occurred at $685\,nm$ for VA(A), $682\,nm$ for VA(J), and for VA(N) and VA(Ak); this occurred at $688\,nm$ and $683\,nm$, respectively. This can be attributed to the compounds allophycocyanin and phycobiliproteins (Seppälä, 2009; Sozer et al., 2010). Generally, the red fluorescence $(675-695\,nm)$ is attributed to the chlorophyll pigments in plants (Lakowicz & Masters, 2008; Papageorgiou & Govindee, 2007). This can also be due to anthocyanins and azulenes (Roshchina, 2012). The deconvoluted peak for VA(J) appeared to have the far-red fluorescence peak at $742\,nm$. Figure 28 shows the LIF spectra for Acanthospermum hispidum (AH) for the four locations. Superimposed in the plot are fitted spectra of the AH sample and the Gaussian fits. The fluorescence peak at $557\,nm$ for AH(A) and AH(J), $552\,nm$ for AH(N), and $551\,nm$ for AH(Ak) may be attributed to the same compounds quercetin, berberine, flavonoids, and flavins as described in figure 27 (Lang et al., 1991; Lichtenthaler et al., 1992). The red fluorescence was occurred at $676\,nm$ for AH(A), $680\,nm$ for AH(J), $679\,nm$ for AH(N), and $678\,nm$ for AH(Ak). Allophycocyanin and phycobiliproteins was assigned to the red fluorescence (Seppälä, 2009; Sozer et al., 2010).

The deconvoluted peaks for the AMHPs sample AH appeared not to exhibit the far-red fluorescence. Figures 29-32 and Appendix B shows the LIF spectra of the AMHPs samples from the four locations. Superimposed in the respective plots are the fitted spectra of the AMHPs samples and its corresponding Gaussian fits. In general, all the AMHPs samples exhibit characteristic fluorescence spectra. Alstonia boonei did not exhibit the double peak band as exhibited by the nine AMHPs samples. The same compounds: quercetin, berberine, flavonoids, and flavins (Lang et al., 1991; Lichtenthaler et al., 1992) attributed to the Gaussian fits in figures 27 and 28 can also be attributed to the Gaussian fits in figures 29 – 31. The green and the yellow to orange fluorescence emissions as seen in all the LIF spectra of the AMHPs samples can also be attributed to a large number of plant secondary metabolites, such as polyphenols (Lang et al., 1991; Roshchina, 2008) and acridone alkaloids (Roshchina, 2008).

There were additional peaks within the spectra of AMHPs samples based on the PeakFit analysis. These peaks were as a result of the varied secondary metabolites that might be present within the AMHPs samples (Lang et al., 1991; Lichtenthaler, 1987; Lichtenthaler & Buschmann, 1987; Lichtenthaler et al., 1992).

The AMHPs samples from the different locations bear similar fluorescence spectra signatures, and therefore, it was difficult to differentiate them (Figures 21-26). In determining the biophysical similarities and differences, if any, between the AMHPs samples from the four locations, unsupervised pattern recognition method (principal component analysis (PCA)) was employed. The fluorescence spectra within the range of 460-635 *nm* for the

AMHPs samples was used as the input data for the PCA analysis. The red fluorescence was not used in the PCA analysis. The fluorescence spectra for the AMHPs samples were converted into a data matrix $(P = M \times N)$ where M represented the number of rows (Observations: fluorescence intensity), and N represented the number of columns (Variables: wavelength).

PCA algorithm was developed and implemented in MATLAB software (MATLAB R2017a, MathWorks Inc.). The aim of the PCA algorithm was to transform the fluorescence spectra of the AMHPs samples from a high dimensional space to a low dimensional space called the principal components (PCs) thereby not altering any spectral information contained in it. This allowed for the detection of any patterns or outliers present in the LIF spectra data and subsequently the information was used in discriminating the AMHPs samples. The output generated from the PCA algorithm were the coefficient, score, latent, t-squared, explained variance and the mean.

The coefficient, also called the loadings, contains the principal component coefficients (PCCs). The columns of the PCCs contain the PCs, and they are ordered in descending order of component variance. The rows of the PCCs correspond to the wavelengths. Figure 33 represents the loading plot for the AMHPs sample VA. This plot revealed that the variables (Wavelength) was responsible for the separation of the AMHPs samples. The wavelength 460-635 *nm* was responsible for the separation of the AMHPs samples for the first principal component. It was realised that as the number of PCs increases, the weight becomes noisier. The PCs scores and PCs variance are respectively generated by the score and the latent. The PCs scores are the representation of the AMHPs sample in the principal component space. The latent contains the

eigenvalues of the covariance matrix of the AMHPs samples. The explained variance gives the percentage of the total variance explained by the PCs and the mean gives the estimated mean for each variable of the AMHPs samples. The eigenvalues contributing to the total variance in the AMHPs samples was plotted (figure 34) for the first 30 PCs. It was observed that the eigenvalues drop of so rapidly with increasing PCs and so the first two PCs was able to retain the maximum variance of the AMHPs sample VA. The percentage variability explained by each PCs was calculated in order to know the contribution of each PCs.

Using the Kaiser criterion (Yeomans & Golder, 1982), two principal components (PC1 and PC2) was retained constituting 99.32 %, of the cumulative variability of the LIF spectra of the AMHPs samples for VA.

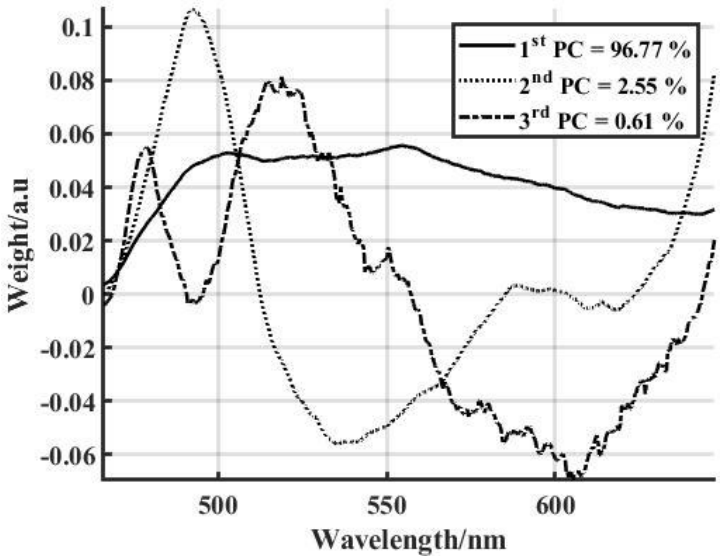

Figure 33: Loadings plot for the first three PCs obtained from PCA of the LIF Spectra of VA from the four Locations

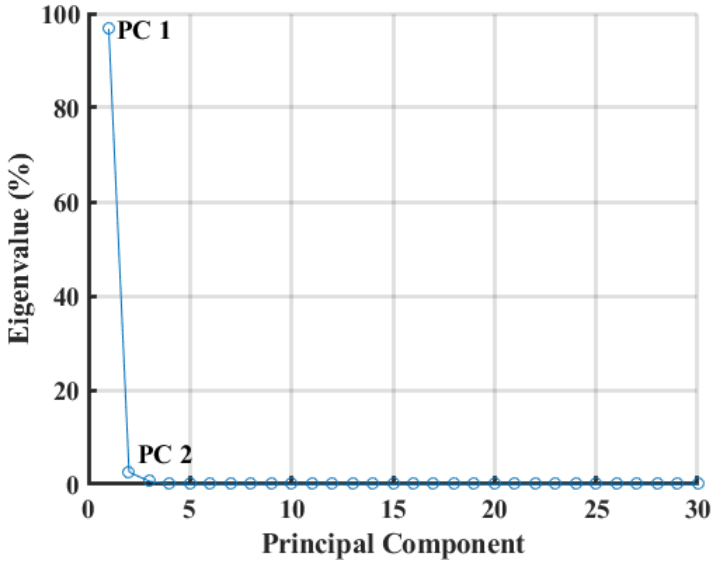

Figure 34: Eigenvalues (%) of the PCs which represent the Percentage Weight of each Principal Component

To visualize the cluster trends, a score plot was obtained by plotting two principal components (PC 1 and PC 2). Figure 35 shows the outcome from the PC analysis and it revealed that, there were separations in the locations of the AMHPs samples VA. All the AMHPs sample VA clustered well along the first two PCs plane where PC 1 and PC 2 could explain 96.77 % and 2.55 % of the variance respectively. The first two PCs contained the maximum information of the AMHPs sample VA and it provides the chemical compositional information in the LIF spectra. The AMHPs sample VA contain considerable differences in the chemical properties according to their locations, pre-harvest activities and post-harvest activities. Similarly, the PCA score plot for AH for the four locations is shown in figures 36. It is observed from the plot that the two PCs was able to differentiate/classify the AMHPs sample AH from the four

locations. The PC plot for the rest of the AMHPs samples is shown in Appendix C.

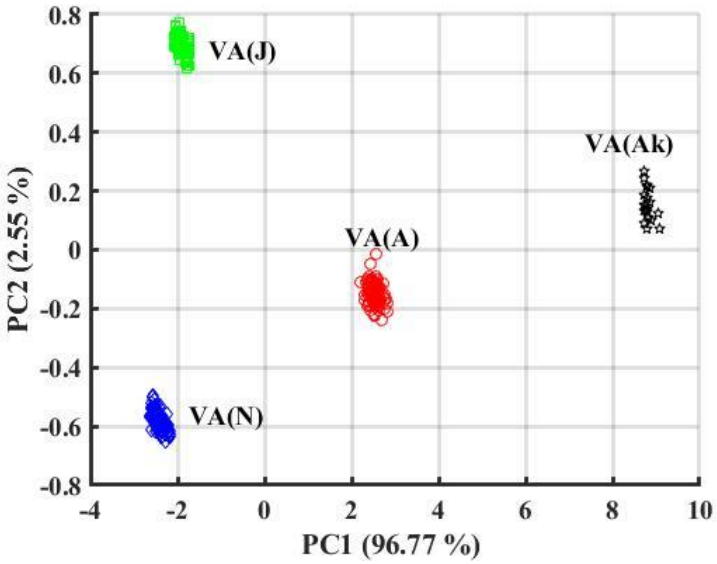

Figure 35: Score plot of VA from the four Locations

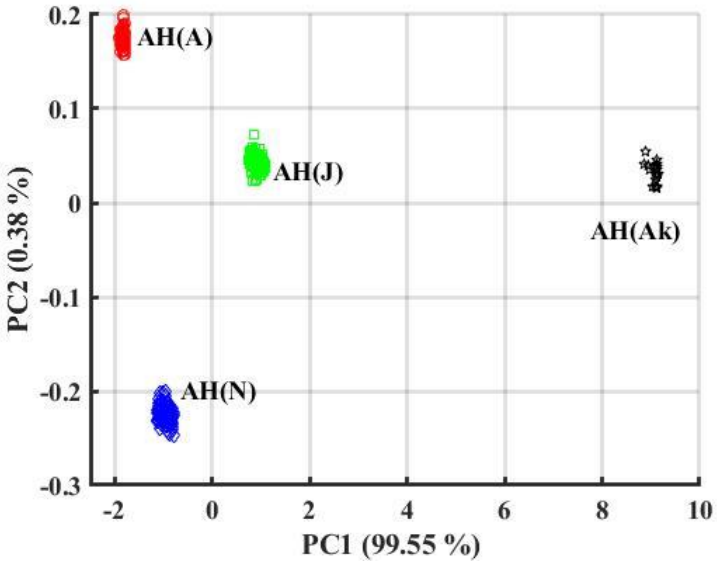

Figure 36: Score plot of AH from the four Locations

Table 6 summarises the AMHPs samples and its cumulative variabilities for two PCs used to differentiate/classify the AMHPs samples from the various locations.

Table 6: The AMHPs Sample and its Cumulative Percentage obtained from the Principal Component Analysis

AMHPs samples	PC1 (%)	PC2 (%)	Cumulative percentage (%)
AB	99.60	0.38	99.98
AI	99.70	0.23	99.93
CO	98.10	1.78	99.88
MI	84.72	13.41	98.13
ML	80.09	18.48	98.57
PP	97.57	1.84	99.41
RV	98.81	0.81	99.62
RC	99.08	0.50	99.58

A plot of all the ten AMHPs samples for the same locations (Figures 37-40) shows similar fluorescence spectra signatures. The fluorescence intensity spectra for Vernonia amygdalina (VA) was low while Alstonia boonei (AB) was high for all the AMHPs samples for all the locations. In figure 37, it was easier to differentiate AI(A) and ML(A) from the other AMHPs within the spectra range of 500-690 *nm.* Also, PP(A) can be differentiated within the $690-800\,nm$ spectra range. In figure 38, ML(J) in the spectra range $500-690\,nm$ could be differentiated, however, it was difficult to differentiate

the others. In figure 39, apart from AB(N) and VA(N), it was difficult to differentiate the other AMHPs samples, however, in figure 40, the AMHPs sample RV(Ak) had a distinct fluorescence spectrum and was easier to differentiate it from the others.

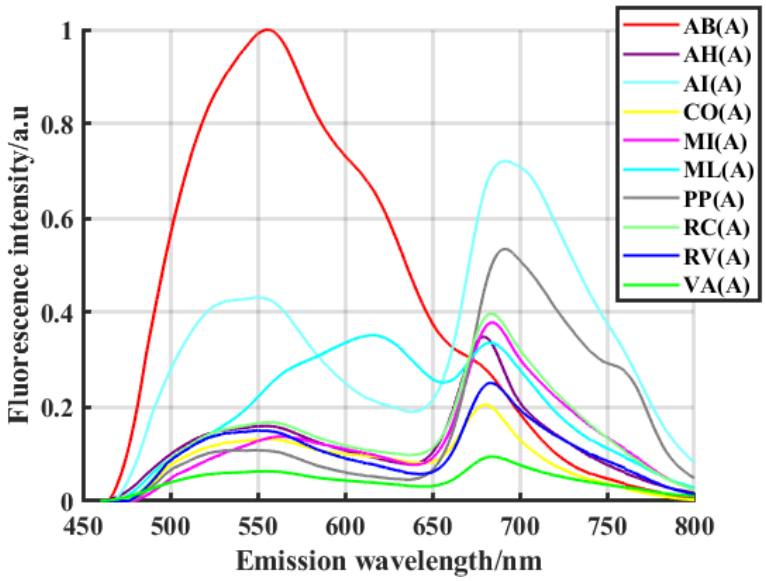

Figure 37: Normalized Average LIF Spectra for the AMHPs Sample obtained from Abrafo

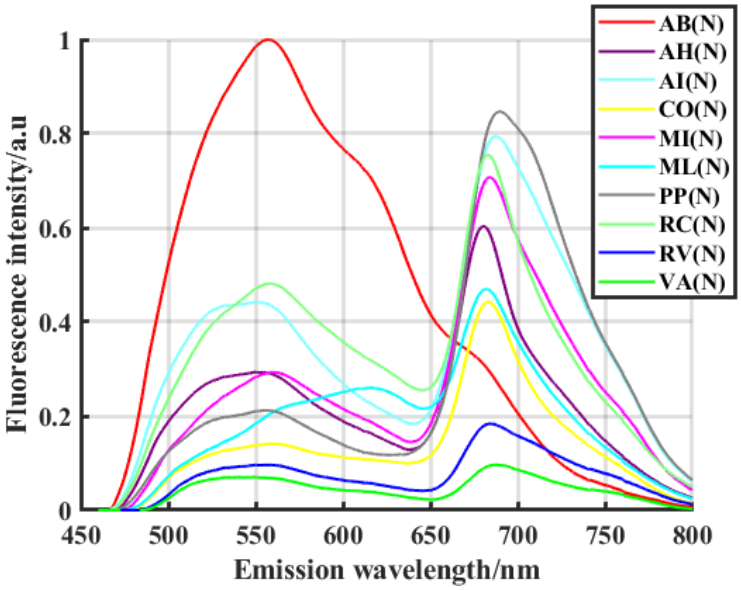

Figure 38: Normalized Average LIF Spectra for the AMHPs Sample obtained from Nfuom

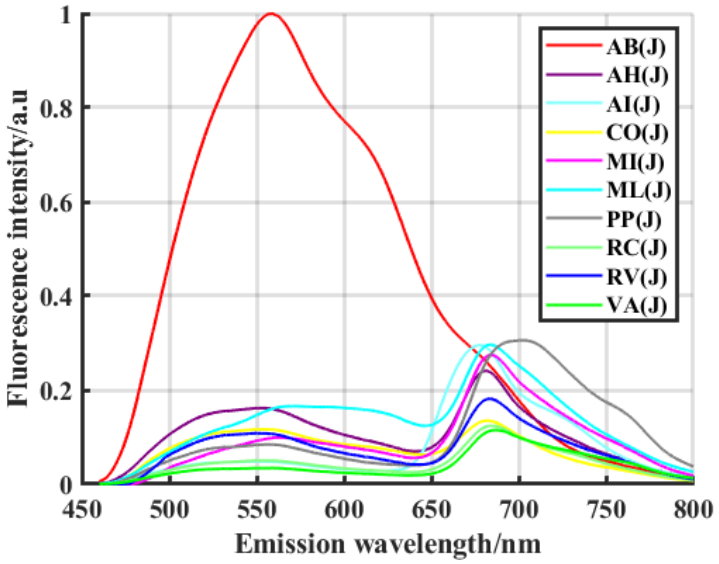

Figure 39: Normalized Average LIF Spectra for the AMHPs Sample obtained from Jukwa

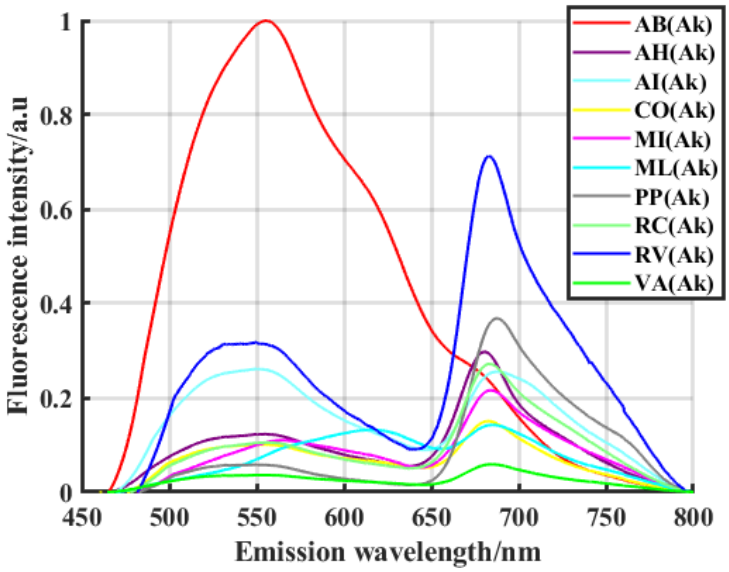

Figure 40: Normalized Average LIF Spectra for the AMHPs Sample obtained from Akotokyere

To determine again the biophysical differences or similarities between the ten AMHPs samples from the same location, PCA and Hierarchical clustering analysis (HCA) was performed. In this analysis, VA from each of the

respective locations were used as a standard against which all other AMHPs samples were assessed due to its safety, efficacy, and effectiveness (Challand & Willcox, 2009; Njan, 2012; Oyeyemi, Akinlabi, Adewumi, Aleshinloye, & Oyeyemi, 2017; Yeap et al., 2010). Figure 41 shows the loading plots for the ten AMHPs samples from Abrafo. PC1 was attributed to the green fluorescence characteristics and this is what is responsible for the anti-malarial properties for the AMHPs samples. PC2, mainly complemented the other fluorescence characteristics. Figure 42 shows the Eigenvalue/scree plot for the AMHPs samples from Abrafo. It can be seen that two PCs can be used to represents all the information present in the AMHPs samples.

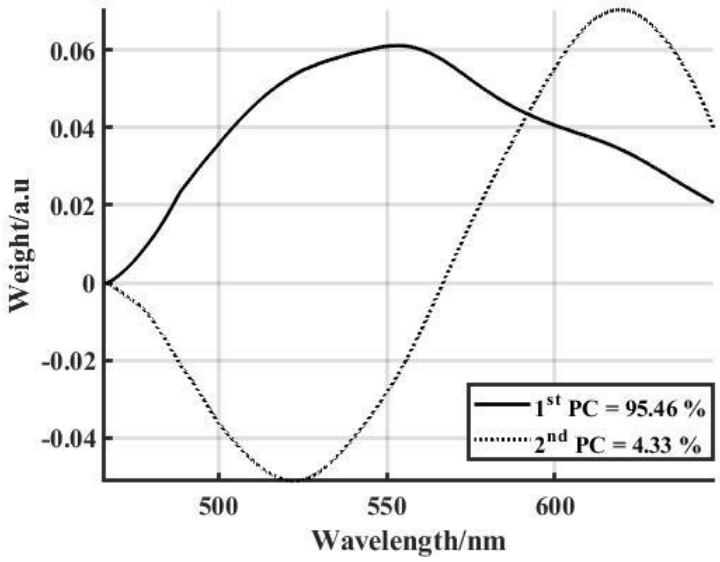

Figure 41: Loadings plot for the first two PCs obtained from PCA LIF Spectra of AMHPs Sample from Abrafo

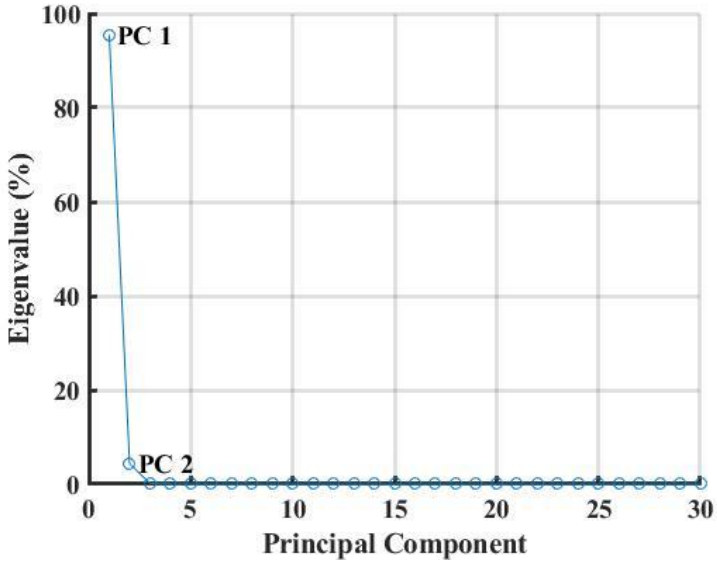

Figure 42: Eigenvalues (%) of the PCs which represent the Percentage Weight of each Principal Component

Figures 43 shows the score plots for PC1 and PC2 with cumulative variances of 99.78 %. Since VA serves as our standard, then any AMHPs samples that are close to it is considered to be biophysically similar in terms of its chemical constituents (Challand & Willcox, 2009; Njan, 2012; Oyeyemi et al., 2017; Yeap et al., 2010). VA(A) from figure 43 is closer to PP(A), RV(A), AH(A), CO(A), RC(A), MI(A), ML(A), than AI(A) and AB(A).

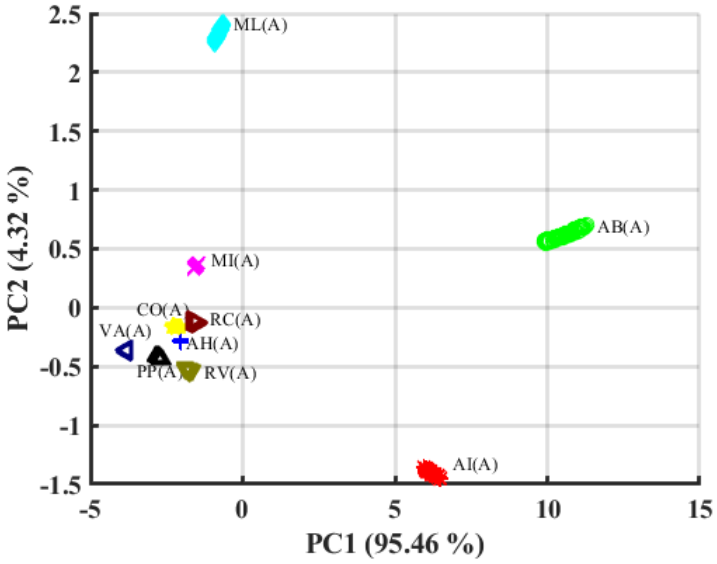

Figure 43: Score plot of the ten AMHPs Sample from Abrafo

Figures 44-46 shows the score plots for the first two PCs with cumulative variances of 99.98 %, 100.00 %, and 99.87 % for location Jukwa, Nfuom, and Akotokyere respectively. The loadings and the scree plots are similar to the one discussed for location Abrafo and therefore has been shown in Appendix D and E respectively. VA(J) was closer to MI(J), AI(J), RC(J), CO(J), PP(J), AH(J), ML(J), than AB(J) in figure 44. Again VA(N) was closer to RV(N), CO(N), PP(N), AH(N), RC(N), MI(N), ML(N), than AI(N) and AB(N) in figure 45. Finally, in figure 45, VA(Ak) was closer to AH(Ak), AI(Ak), RV(Ak), CO(Ak), RC(Ak), PP(Ak), MI(Ak), ML(Ak), than AB(Ak). The differences in the different pairings of the AMHPs samples in the score plots for the different location might be as a result of the inherent soil characteristics.

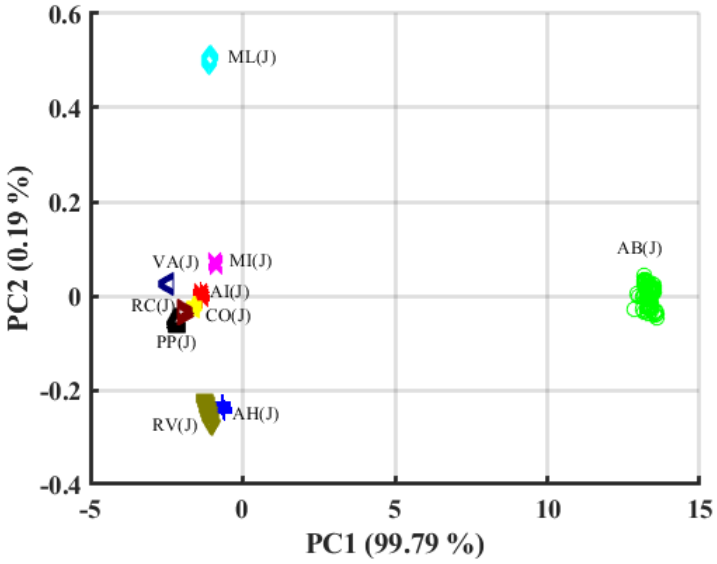

Figure 44: Score plot of the ten AMHPs Sample from Jukwa

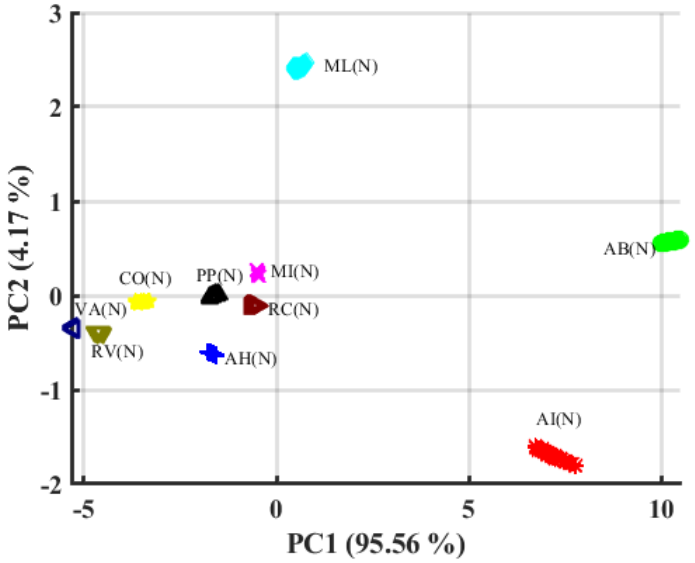

Figure 45: Score plot of the ten AMHPs Sample from Nfuom

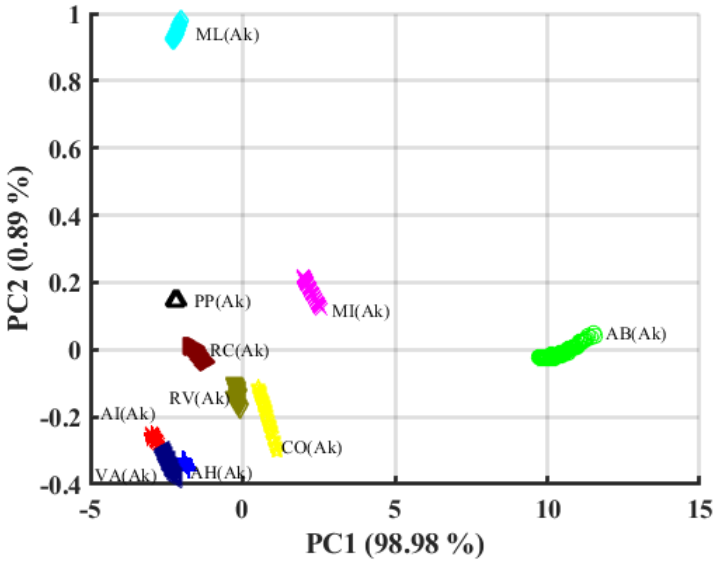

Figure 46: Score plot of the ten AMHPs Sample from Akotokyere

Since HCA is also an unsupervised pattern technique, the results obtained from the PCA is complimentary to HCA. Figures 47-50 shows the dendrogram for the AMHPs samples from the four locations. Selecting a distance threshold of 10 shows that there are two clusters. In figure 47, cluster I consists of AH(A), CO(A), RV(A), RC(A), MI(A), PP(A), VA(A), and ML(A) while cluster II consists of AI(A) and AB(A). In figure 48, cluster I consists of PP(J), RC(J), VA(J), AH(J), MI(J), RV(J), AI(J), CO(J), and ML(J) while cluster II is made up of only AB(J). Moreover, in figure 49, cluster I consists of MI(N), RC(N), AH(N), PP(N), ML(N), CO(N), RV(N), and VA(N) while cluster II consists of AB(N) and AI(N). Finally, in figure 50, cluster I consists of AH(Ak), RC(Ak), PP(Ak), AI(Ak), VA(Ak), ML(Ak), CO(Ak), RV(Ak), and MI(Ak) while cluster II is made up of only AB(J). From figures 47-50, the AMHPs samples shows a good fit revealing a significant cophenetic correlation coefficient of 0.9500, 0.9970, 0.9248, and 0.9498 for Abrafo, Jukwa, Nfuom,

and Akotokyere respectively. The cophenetic correlation coefficient gives a measure of the dissimilarities between the AMHPs samples.

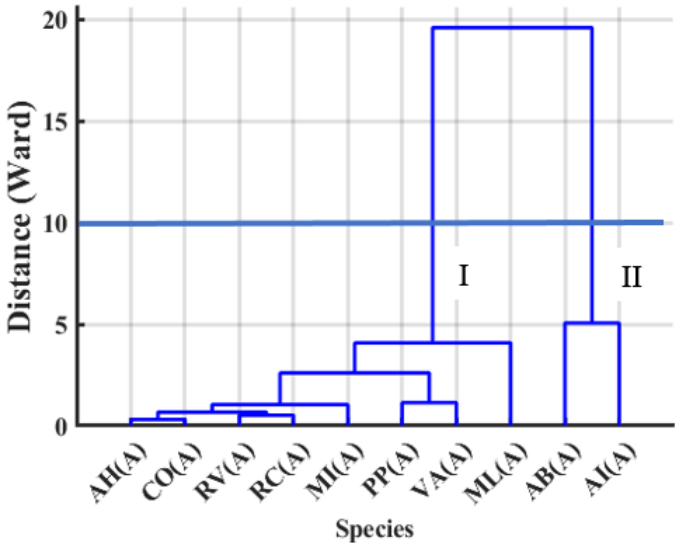

Figure 47: The Clustering Analysis of the Fluorescence Spectra for the ten AMHPs Sample from Abrafo

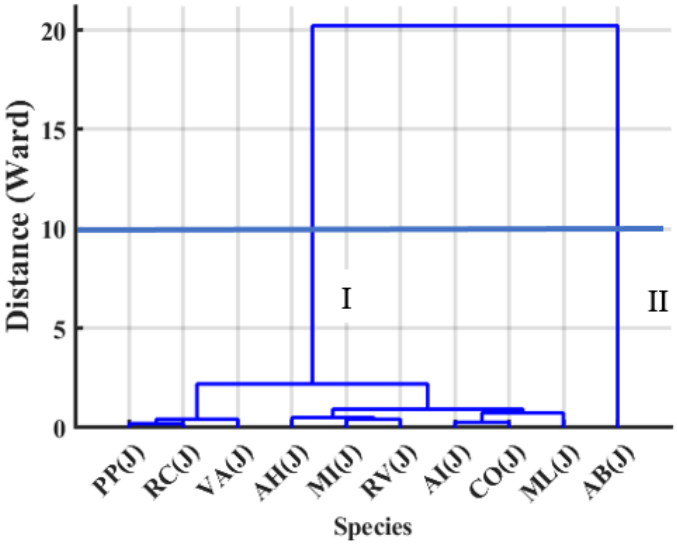

Figure 48: The Clustering Analysis of the Fluorescence Spectra for the ten AMHPs Sample from Jukwa

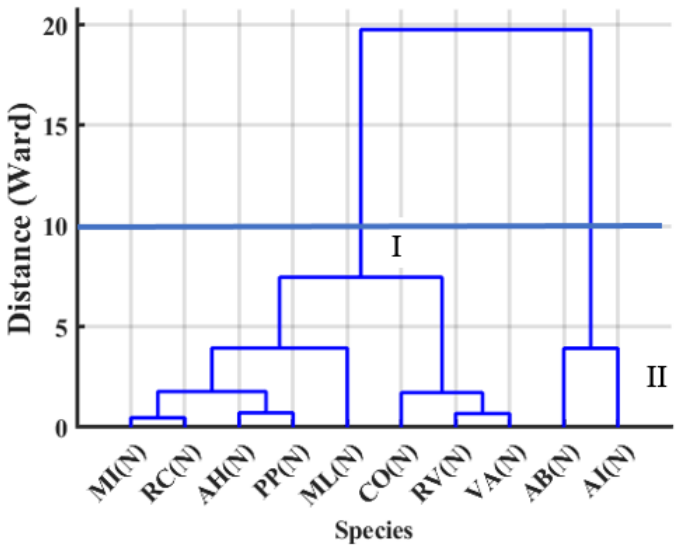

Figure 49: The Clustering Analysis of the Fluorescence Spectra for the ten AMHPs Sample from Nfuom

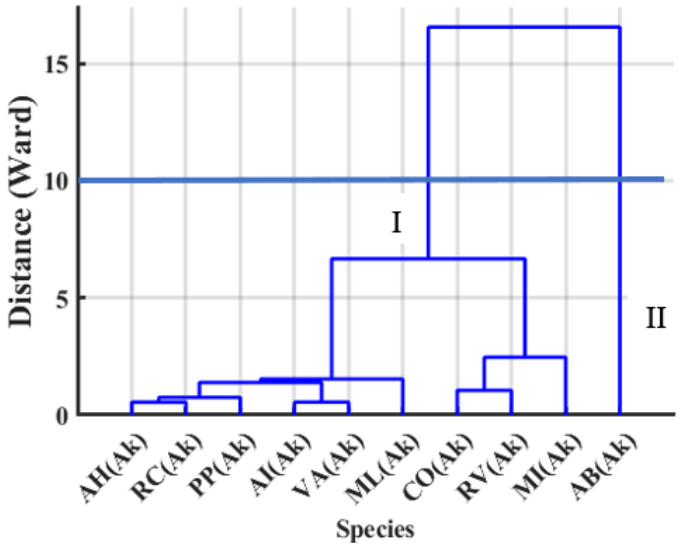

Figure 50: The Clustering Analysis of the Fluorescence Spectra for the ten AMHPs Sample from Akotokyere

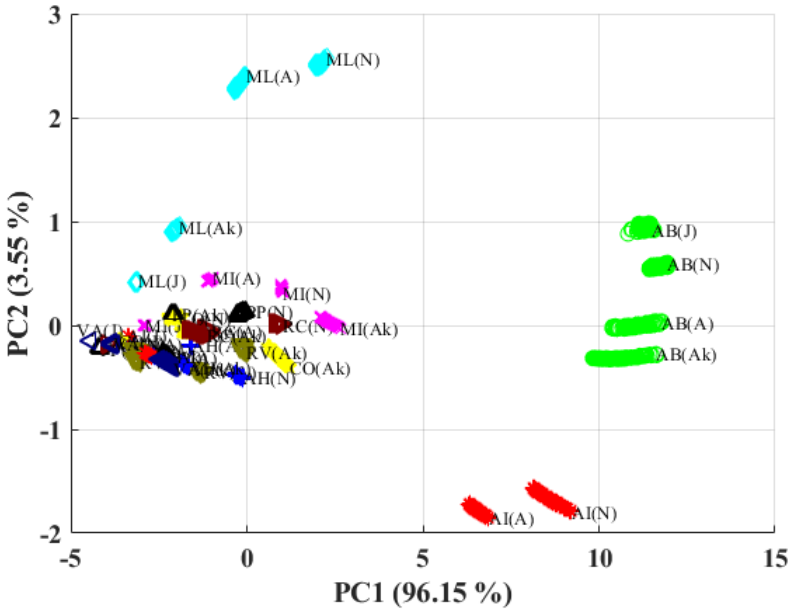

Figure 51: Score plot of the ten AMHPs Sample from the four Locations

A plot of the score plot for the ten AMHPs samples for the four locations is shown in figure 51. PC1 and PC2 contributed to 96.15 % and 3.55 % respectively to the variance in the LIF spectra. It can be observed from the plot that, AMHPs sample AB has a linear relationship with its location together with AMHPs sample ML. The same can be said of AMHPs sample AI. The AMHPs samples from the four locations also form a cluster around VA indicating a chemical similarity among the AMHPs samples.

Herborists (Herbal medicine marketers), receive their supply especially AMHPs samples from all over the country. These AMHPs samples always come in different forms (leaves, roots, bark, etc.). They are display on table tops in the market centres. The variability of the secondary metabolites of these AMHPs varies from factors such as the soil type, cultivating region, the climate (temperature, humidity, wind), pre-harvest time, post-harvest time. The differences can also be caused by the method of drying, washing, crushing, and

pulverizing AMHPs as well as storage (Alaerts et al., 2012; L.-w. Yang et al., 2005; Zou, Hong, & Koh, 2005). Effective identification of the AMHPs samples and their locations, as part of the quality control measures are vital for consumer's safety. There are no fast and easy standard methods for regulatory authorities to use in determining for instance the identity and locations where these AMHPs samples are obtained. Therefore, an attempt was made to determine the identity and locations of these AMHPs samples based on the four locations (Abrafo, Jukwa, Nfuom, and Akotokyere).

Since the AMHPs samples have similar biophysical property (Amuah, Eghan, Anderson, Adueming, & Opoku-Ansah, 2017), it was extremely difficult to determine the location of the AMHPs samples just by observing the fluorescence spectra. Therefore, supervised pattern recognition methods: Support Vector Machine (SVM), K-Nearest Neighbour (KNN), and Linear Discriminant Analysis (LDA), were employed to help in the identification of the AMHPs from the various locations.

PCA of the LIF spectra was used as input data to generate the models (Figure 52) for the identification. The first two PCs in figure 41 which explained more than 99 % of the total variance in the LIF spectra with the remaining accounting for just a little was employed for the identification of the AMHPs samples from the four different locations (Ian T Jolliffe, 1986).

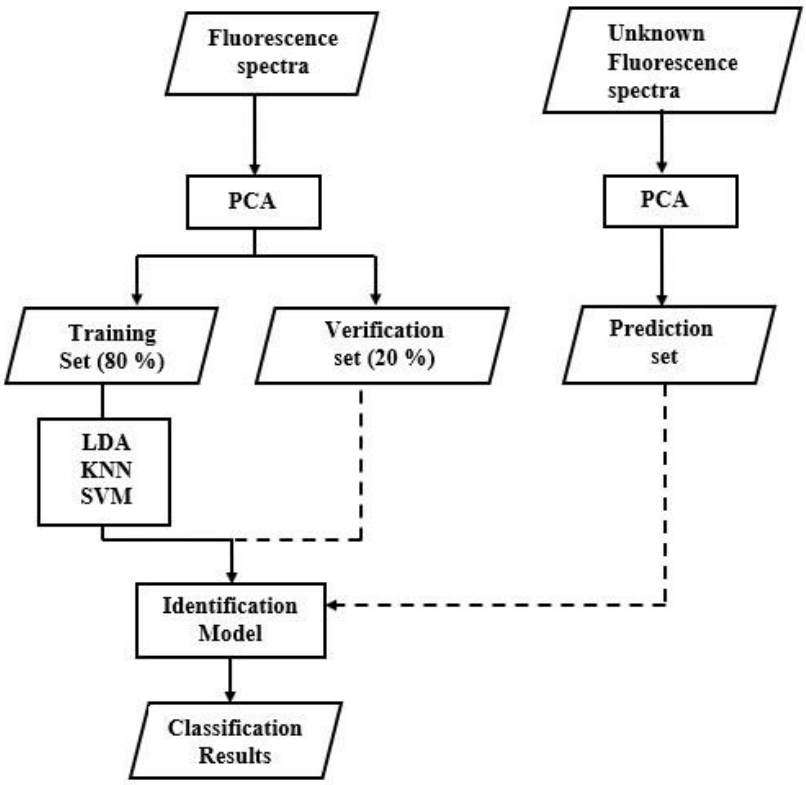

Figure 52: A Flow Chart for Processing the AMHPs Sample with the different Training, Verification, and Prediction sets

Table 7 details the classification results for LDA, SVM and KNN models for the training, verification and prediction sets. For the training set, 2,880 LIF spectra were collected from the ten AMHPs samples for the four locations representing 80 % of the LIF spectra data. 720 LIF spectra representing 20 % of the LIF spectra data was used for the verification sets. Finally, 4,000 LIF spectra data from the ten AMHPs samples from the four locations were later used as prediction sets. The classification results show that all the models used can be used to identify the AMHPs samples according to the four locations based on the LIF spectra collected. It can be observed from Table 7 that the classification results for the training sets was 100.00 % for SVM, 99.95 % for KNN, and 99.23 % for LDA. For the verification sets, SVM and KNN was

100.00 % while LDA was 98.23 %. Finally, for the prediction sets, the two models SVM and KNN obtained 100.00 % prediction while LDA obtained 99.31 % prediction.

Table 7: Classification Results (%) of SVM, KNN, and LDA, Models of the AMHPs Sample, using PCs obtained from the LIF Measurements as Input Variables

Method	Training set (2,880 spectra)	Verification set (720 spectra)	Prediction set (4,000 spectra)
SVM	100.00	100.00	100.00
KNN	99.95	100.00	100.00
LDA	99.23	99.23	99.31

Figure 53 and 54 shows the confusion matrix for only the prediction set using the SVM model for the AMHPs samples. The rows show the AMHPs samples with true class and the columns show the predicted class of the AMHPs samples. This shows that there was no misclassification of the AMHPs samples based on their locations. That is the ability of the SVM model to predict 100 % unknown AMHPs samples from the four locations. However, there were misclassification for the LDA model for the calibration, verification and prediction set for the AMHPs samples. Figure 55 and 56 shows only the prediction set for LDA. As shown in table 8, 0.69 % of the AMHPs samples were misclassified. For example, in figure 54, 2 samples of AH(Ak) was misclassified for VA(N), 3 samples of AI(N) was misclassified for RC(A), and 1 sample of ML(Ak) was misclassified for VA(A).

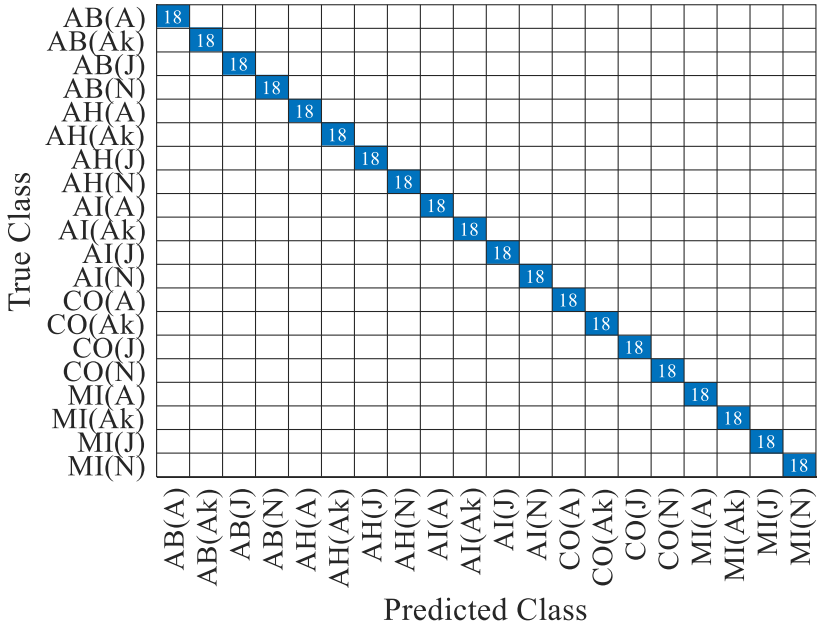

Figure 53: Confusion Matrix for the Prediction set of the AMHPs Sample for the SVM Model for five AMHPs Sample

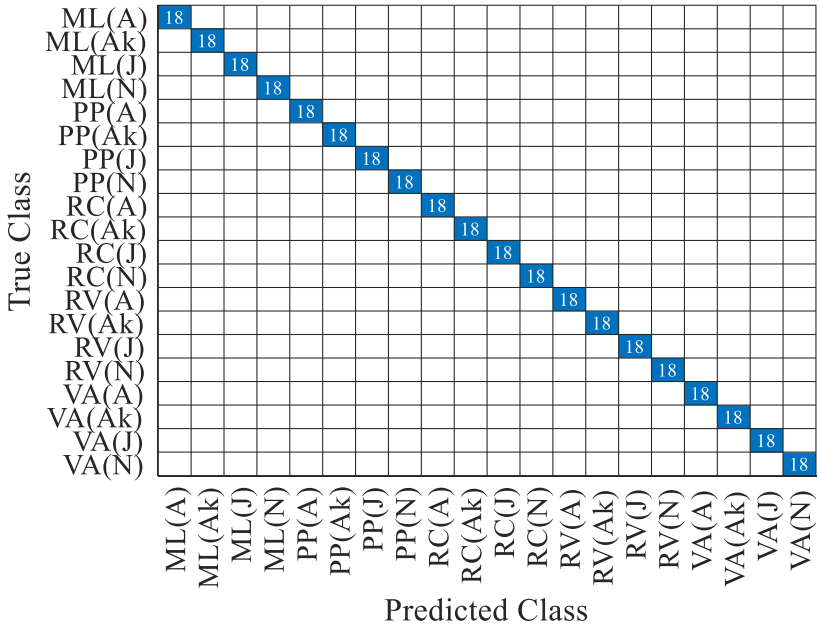

Figure 54: Confusion Matrix for the Prediction set of the AMHPs Sample for the SVM Model for the other five AMHPs Sample

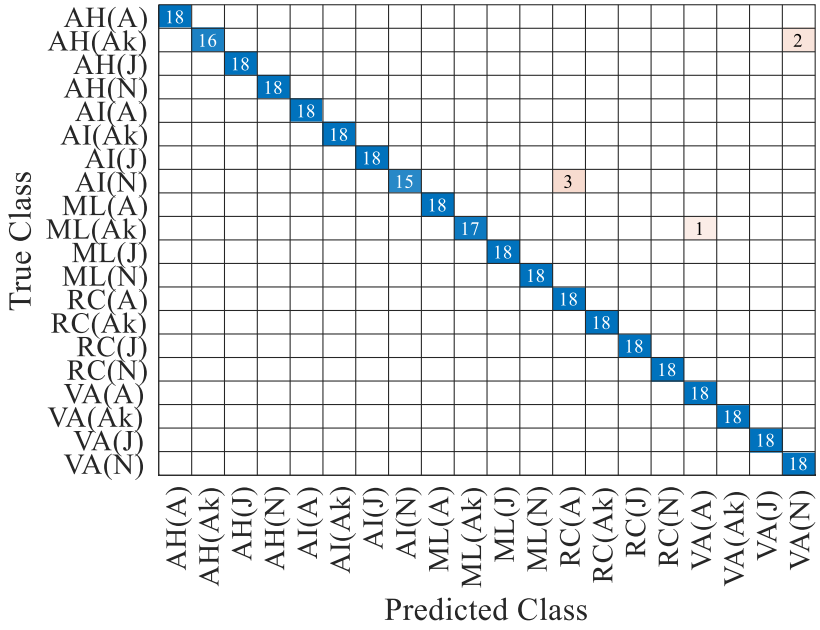

Figure 55: Confusion Matrix for the Prediction set of the AMHPs Sample for the LDA Model for five AMHPs Sample

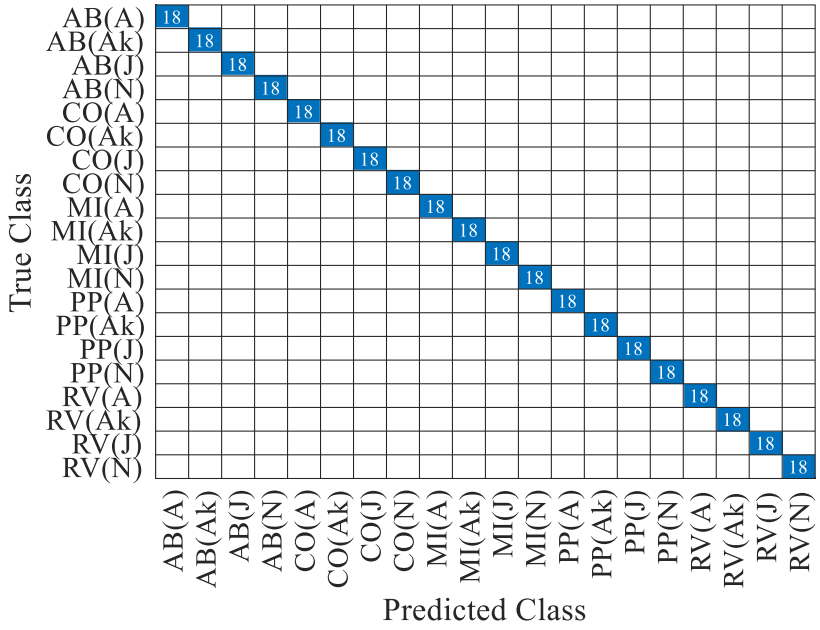

Figure 56: Confusion Matrix for the Prediction set of the AMHPs Sample for the LDA Model for the other five AMHPs Sample

Results from the Attenuated Total Reflection-Fourier Transform Infrared (ATR-FTIR) Measurements of the AMHPs Sample

The infrared (IR) spectra for six AMHPs samples from the four different locations obtained using the PerkinElmer spectrum two spectrometer equipped with an ATR accessory are shown in figure 57 to figure 62. The sharp peaks in this spectral region (4000-650 cm^{-1}), indicates that the AMHPs samples have a rich chemical composition. Table 8 and 9 shows the averaged peak assignment for the ten AMHPs samples compared with standard chart (Lin-Vien, Colthup, Fateley, & Grasselli, 1991; Long, 2004; Meier, 2003; Movasaghi, Rehman, & ur Rehman, 2008; Smith, 1998; Socrates, 2001; Stuart, 2005). The ATR-FTIR spectra for the other four AMHPs samples is shown in Appendix F. In figures 57-62, the O-H and N-H stretching vibrations from carbohydrates and proteins can be linked with the absorption band located around $3200\,cm^{-1}$ whilst the CH stretching vibrations are caused by lipids and carbohydrates absorbs around $3000\,cm^{-1}$.

The absorption peak around $1732\,cm^{-1}$ correspond to the carbonyl group (COOR). This can be attributed to the ester-containing compounds commonly found in membrane lipid and cell wall pectin. Bands raised by acids ($-COO^-$) were located around $1600\,cm^{-1}$. Bands around $1100\,cm^{-1}$ in the "fingerprint region" indicate several modes such as C-H bending or C-O or C-C stretching. Carbohydrates in the leaves, stem bark were the major constituents that contributed to these absorption bands.

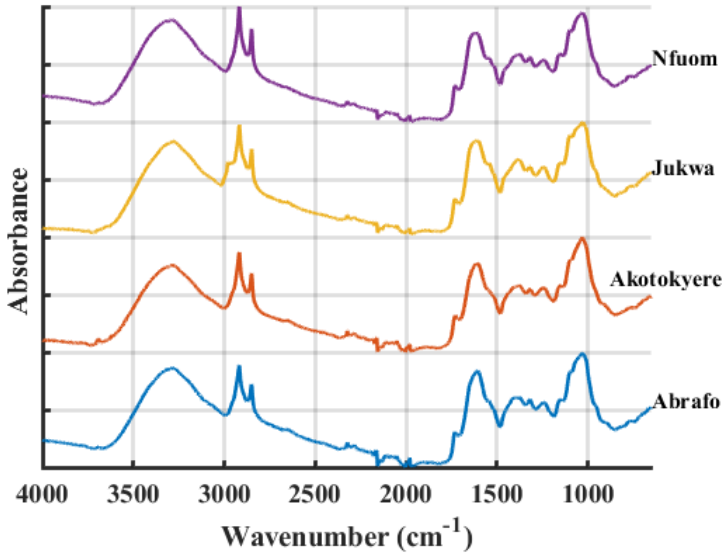

Figure 57: ATR-FTIR Spectra of Vernonia Amygdalina from the four Locations

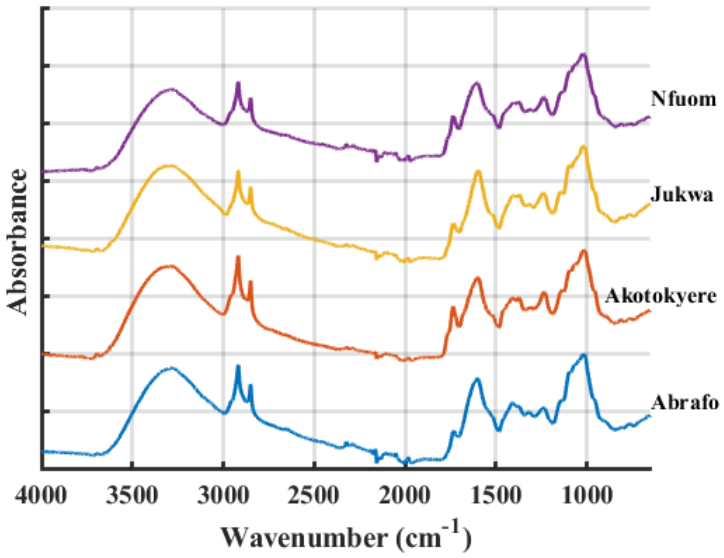

Figure 58: ATR-FTIR Spectra of Acanthospermum Hispidum from the four Locations

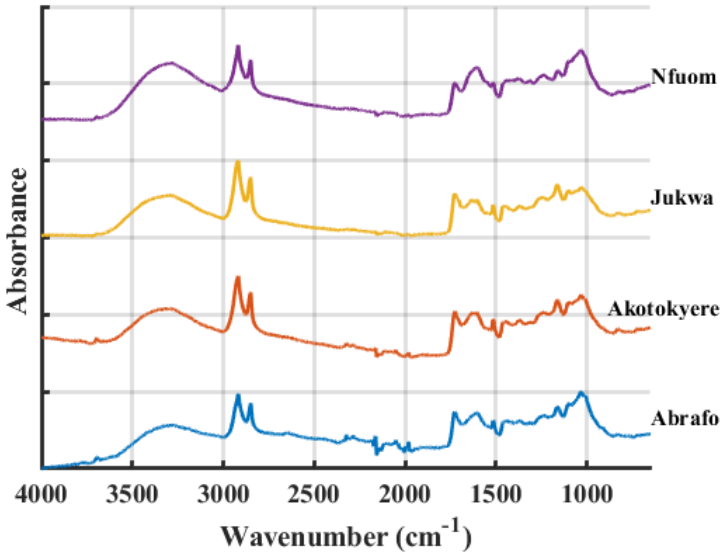

Figure 59: ATR-FTIR Spectra of Azadirachta indica from the four Locations

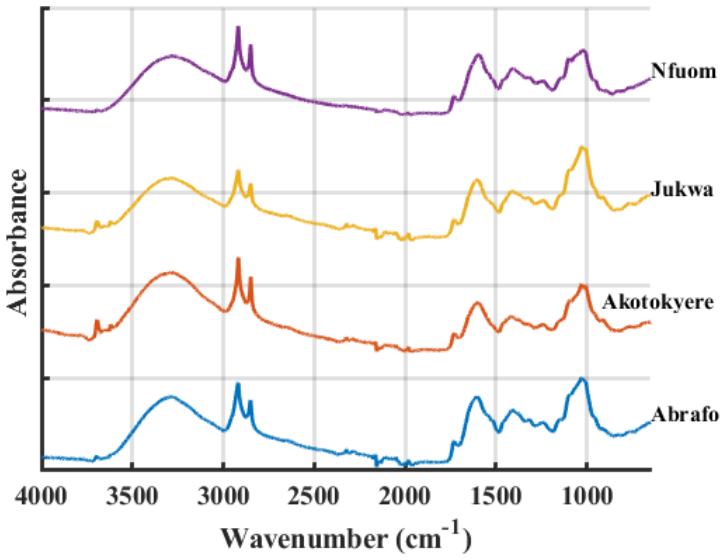

Figure 60: ATR-FTIR Spectra of Cassia Occidentalis from the four Locations

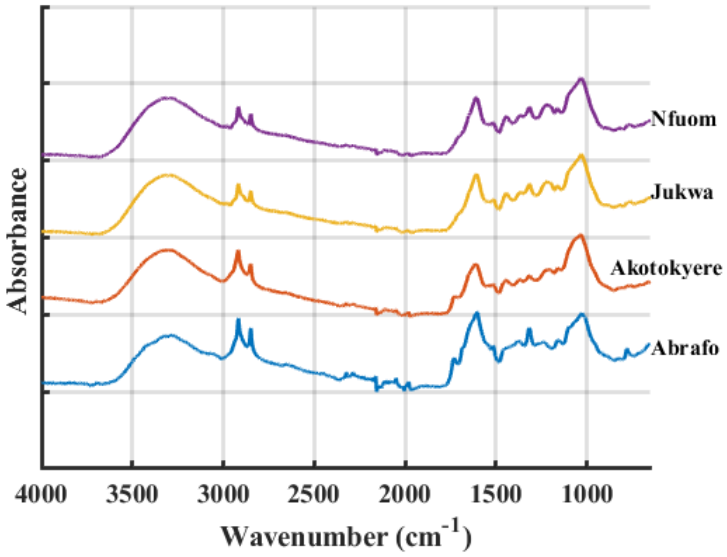

Figure 61: ATR-FTIR Spectra of Morinda Lucida from the four Locations

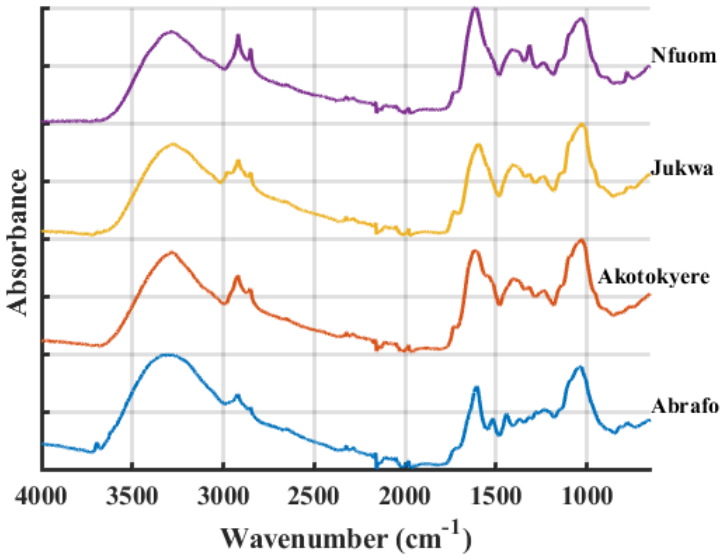

Figure 62: ATR-FTIR Spectra of Ricinus Communis from the four Locations

Table 8: Average ATR-FTIR Peak Assignments for five AMHPs Sample

Functional groups	VA	AB	AH	AI	CO
$-OH, -NH$					3693.0±0.0
	3279.8±3.0	3283.5±3.5	3282.5±3.4	3282.5±3.4	3274.8±10.8
$-CH$	2917.8±0.5	2917.5±0.7	2918.0±0.0	2918.0±0.0	2917.8±0.5
	2850.0±0.0	2850.0±0.0	2850.0±0.0	2850.0±0.0	2849.8±0.5
$-COOR$	1732.0±0.0	1731.0±0.0	1734.3±2.1	1734.3±2.1	1730.3±1.3
$-C=O, -NH, -COO^{-}$	1606.5±0.6	1607.0±0.0	1600.8±2.2	1600.8±2.2	1596.8±4.3
		1516.0±0.0			
$-CH, -C-N, -NH$	1376.3±2.5	1438.0±0.0	1374.0±1.4	1382.3±17.2	1409.3±7.5
	1318.0±0.0	1372.0±0.0	1316.0±0.0	1316.0±0.0	
	1240.5±1.0	1242.5±2.1	1236.3±1.3	1236.3±1.3	1237.8±0.5
$-CH, -C-C, -C-O-C$	1028.0±0.5	1033.5±0.7	1014.3±1.5	1014.3±1.5	1028.5±0.7
					1008.7±5.8
					912.0±0.0

Table 9: Average ATR-FTIR Peak Assignments for the other five AMHPs Sample

Functional groups	MI	ML	PP	RC	RV
$-OH, -NH$		3695.0±0.0		3692.0±0.0	3694.0±0.0
	3279.8±3.0	3280.0±2.8	3282.8±3.3	3280.0±0.8	3289.0±8.2
$-CH$	2917.8±0.5	2917.8±0.5	2917.5±0.6	2918.5±1.3	2919.8±0.5
	2850.0±0.0	2849.0±0.5	2850.0±0.0	2850.8±0.5	2849.8±0.5
$-COOR$	1729.0±0.0	1730.5±0.6	1731.5±0.6	1730.8±1.9	1730.8±0.5
$-C=O, -NH, -COO^{-}$	1606.3±1.0	1604.8±4.9	1609.0±1.4	1604.5±7.0	1622.8±11.4
		1516.5±0.7	1516.5±0.7		1516.3±0.6
$-CH, -C-N, -NH$	1376.5±2.4		1438.0±0.0	1404.5±2.4	1438.5±0.7
	1318.3±0.5	1375.0±1.0	1374.0±1.0	1317.0±1.4	1369.8±2.4
	1240.7±1.2	1317.0±1.0	1241.8±1.5	1236.3±1.5	1236.8±0.5
		1239.0±3.4			
		1159.0±1.4			1153.8±5.3
$-CH, -C-C, -C-O-C$	1029.0±0.8	1031.0±4.7	1033.3±1.7	1029.0±0.8	1099.0±0.0
			1008.0±0.0		1026.0±3.0
		913.0±0.0			
		781.0±0.0	764.0±0.0	780.0±0.0	

Similarities of AMHPs Samples using Correlation Coefficient and Congruence coefficient

The similarity analysis of the AMHPs samples used were determined using the correlation and congruence coefficient (Wang et al., 2012; Xu, Liang, Chau, & Vander Heyden, 2006; Yudthavorasit, Wongravee, & Leepipatpiboon, 2014; Zhu et al., 2010). The similarity analysis was employed as a mathematical quantity to identify the statistical relationship among data objects. If there is no relationship between pair-wise samples, the correlation and congruence coefficient is 0 or very low. On the other hand, a perfect similarity gives a coefficient of 1 (Liu et al., 2011; Wang et al., 2012; Zhu et al., 2010) indicates higher degree of similarity among samples. The mean ATR-FTIR spectra within the range of $2000-650\,cm^{-1}$ was used as a representative of the AMHPs samples in the calculation. To determine the similarities between AMHPs samples from the different locations, the correlation and congruence coefficient of the AMHPs samples were evaluated. As shown in figures 57-62, all the AMHPs samples have high similarities in their spectra profile. Table 10 shows the correlation and congruence coefficient of the ATR-FTIR spectra for six AMHPs samples from the four locations. The correlation and congruence coefficients of VA(A) as compared with VA(J), VA(N), and VA(Ak) are close to 1. This shows that the AMHPs sample VA are closely similar to each other irrespective of the location. This was observed for all the AMHPs samples from the various locations.

Table 10: Similarity Analysis of ATR-FTIR of AMHPs Sample from the different Locations

Species and locations	Correlation coefficient	Congruence coefficient
VA(A)	1.0000 ± 0.0000	1.0000 ± 0.0000
VA(J)	0.9983 ± 0.0000	0.9996 ± 0.0000
VA(N)	0.9984 ± 0.0000	0.9996 ± 0.0000
VA(Ak)	0.9916 ± 0.0001	0.9994 ± 0.0000
AH(A)	1.0000 ± 0.0000	1.0000 ± 0.0000
AH(J)	0.9940 ± 0.0002	0.9984 ± 0.0000
AH(H)	0.9886 ± 0.0003	0.9962 ± 0.0001
AH(Ak)	0.9860 ± 0.0004	0.9967 ± 0.0001
AI(A)	1.0000 ± 0.0000	1.0000 ± 0.0000
AI(J)	0.9659 ± 0.0009	0.9753 ± 0.0007
AI(H)	0.9731 ± 0.0007	0.9826 ± 0.0005
AI(Ak)	0.9814 ± 0.0005	0.9788 ± 0.0006
CO(A)	1.0000 ± 0.0000	1.0000 ± 0.0000
CO(J)	0.9674 ± 0.0009	0.9925 ± 0.0002
CO(N)	0.9909 ± 0.0002	0.9974 ± 0.0001
CO(Ak)	0.9706 ± 0.0008	0.9919 ± 0.0002
ML(A)	1.0000 ± 0.0000	1.0000 ± 0.0000
ML(J)	0.9587 ± 0.0011	0.9906 ± 0.0003
ML(H)	0.9886 ± 0.0003	0.9886 ± 0.0003
ML(Ak)	0.9859 ± 0.0004	0.9961 ± 0.0001
RC(A)	1.0000 ± 0.0000	1.0000 ± 0.0000
RC(J)	0.9844 ± 0.0004	0.9944 ± 0.0002
RC(H)	0.9898 ± 0.0003	0.9978 ± 0.0001
RC(Ak)	0.9980 ± 0.0001	0.9971 ± 0.0001

In determining the correlation and congruence coefficient of the AMHPs samples from the same location based on the chemical constituents present in them, Vernonia amygdalina (VA) was selected as the standard (Challand &

Willcox, 2009; Njan, 2012; Oyeyemi et al., 2017; Teng, Kiat, Suwanarusk, & Koh, 2016; Yeap et al., 2010). Table 12-15 respectively show the correlation and congruence coefficient of the ATR-FTIR spectra of the AMHPs samples from Abrafo, Jukwa, Nfuom, and Akotokyere. In Table 11, all the AMHPs samples had correlation and congruence coefficients close to 1. The same can be said of the AMHPs samples from different locations as observed in Tables 12-14. The similarities of the AMHPs samples may be as a result of the rich chemical composition of the AMHPs samples as illustrated in figures 57-62.

Table 11: Similarity Analysis of ATR-FTIR Spectra of AMHPs

Sample from the same Location (Abrafo)

AMHP	Correlation coefficient	Congruence coefficient
VA(A)	1.0000 ± 0.0000	1.0000 ± 0.0000
AH(A)	0.9845 ± 0.0004	0.9960 ± 0.0001
CO(A)	0.9925 ± 0.0002	0.9982 ± 0.0000
MI(A)	0.9489 ± 0.0012	0.9877 ± 0.0001
ML(A)	0.9856 ± 0.0039	0.9958 ± 0.0001
PP(A)	0.9630 ± 0.0010	0.9906 ± 0.0003
RC(A)	0.9904 ± 0.0003	0.9963 ± 0.0001
RV(A)	0.9836 ± 0.0004	0.9961 ± 0.0001
AB(A)	0.9205 ± 0.0002	0.9712 ± 0.0008
AI(A)	0.9162 ± 0.0023	0.9633 ± 0.0009

Table 12: Similarity Analysis of ATR-FTIR Spectra of AMHPs

Sample from the same Location (Jukwa)

AMHP	Correlation coefficient	Congruence coefficient
VA(J)	1.0000 ± 0.0000	1.0000 ± 0.0000
AH(J)	0.9760 ± 0.0007	0.9943 ± 0.0001
CO(J)	0.9614 ± 0.0105	0.9904 ± 0.0003
MI(J)	0.9498 ± 0.0013	0.9875 ± 0.0003
ML(J)	0.9822 ± 0.0005	0.9958 ± 0.0001
PP(J)	0.9567 ± 0.0012	0.9892 ± 0.0029
RC(J)	0.9880 ± 0.0003	0.9971 ± 0.0000
RV(J)	0.9171 ± 0.0023	0.9801 ± 0.0005
AB(J)	0.9255 ± 0.0202	0.9788 ± 0.0006
AI(J)	0.8762 ± 0.0033	0.9713 ± 0.0008

Table 13: Similarity Analysis of ATR-FTIR Spectra of AMHPs

Sample from the same Location (Nfuom)

AMHP	Correlation coefficient	Congruence coefficient
VA(N)	1.0000 ± 0.0000	1.0000 ± 0.0000
AH(N)	0.9736 ± 0.0008	0.9908 ± 0.0003
CO(N)	0.9782 ± 0.0006	0.9944 ± 0.0002
MI(N)	0.9615 ± 0.0010	0.9902 ± 0.0002
ML(N)	0.9901 ± 0.0001	0.9986 ± 0.0001
PP(N)	0.9662 ± 0.0009	0.9917 ± 0.0002
RC(N)	0.9702 ± 0.0008	0.9928 ± 0.0001
RV(N)	0.9965 ± 0.0000	0.9988 ± 0.0000
AB(N)	0.9335 ± 0.0018	0.9813 ± 0.0005
AI(N)	0.9803 ± 0.0005	0.9944 ± 0.0002

Table 14: Similarity Analysis of ATR-FTIR Spectra of AMHPs

Sample from the same Location (Akotokyere)

AMHP	Correlation coefficient	Congruence coefficient
VA(Ak)	1.0000 ± 0.0000	1.0000 ± 0.0000
AH(Ak)	0.9769 ± 0.0001	0.9946 ± 0.0001
CO(Ak)	0.9606 ± 0.0011	0.9895 ± 0.0028
MI(Ak)	0.9725 ± 0.0010	0.9852 ± 0.0002
ML(Ak)	0.9951 ± 0.0001	0.9987 ± 0.0000
PP(Ak)	0.9834 ± 0.0004	0.9957 ± 0.0001
RC(Ak)	0.9861 ± 0.0004	0.9965 ± 0.0000
RV(Ak)	0.9839 ± 0.0004	0.9962 ± 0.0001
AB(Ak)	0.9468 ± 0.0014	0.9645 ± 0.0010
AI(Ak)	0.9258 ± 0.0020	0.9831 ± 0.0005

Soil Texture Analysis

The availability of nutrients in a soil is primarily determined by the soil texture and potential of hydrogen (pH). Soil texture relates to the relative proportion of sand, silt, and clay present within the soil. It is an important parameter that determines the surface area of solids per unit volume or mass of soil. The soil texture also influences the pore distribution in the soil. Figure 63 shows the soil texture for the top soil for the four locations. Soil texture affects the ability of the soil to retain water and nutrients. Soil with large amounts of clay tend to hold nutrients more efficiently than sandy soils, however, they tend to become waterlogged. Sand does not hold nutrients very tightly, as water drains through the sandy soil, it tends to carry nutrients along with it. It can be seen from figure 63 that the soil texture for Ak-TS, A-TS, and N-TS had a textural class of Sandy Clay Loam while J-TS had a Sandy Loam textural class. In figure 64 the textural class for the soil samples for the Sub Soil from the four locations were all Sandy Clay Loam. This suggests that, the nutrients found in these soil types may be similar as well as plants grown within this type of soil.

The differences in the PCA results in figures 43-46 cannot be attributed to the soil texture analysis from the different locations. This is evident in the fact that, for each location, the soil texture was Sandy Clay Loam for both the Top Soil and the Sub Soil except for the top soil from Jukwa which had a textural class of Sandy Loam.

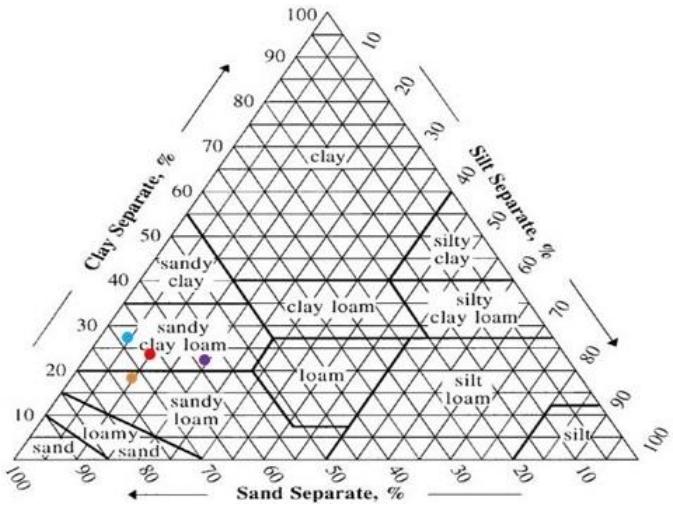

Figure 63: Soil Textural Triangle for the Top Soil of the four Locations (Akotokyere-Red, Jukwa-Orange, Abrafo-Light blue, and Nfuom-Purple)

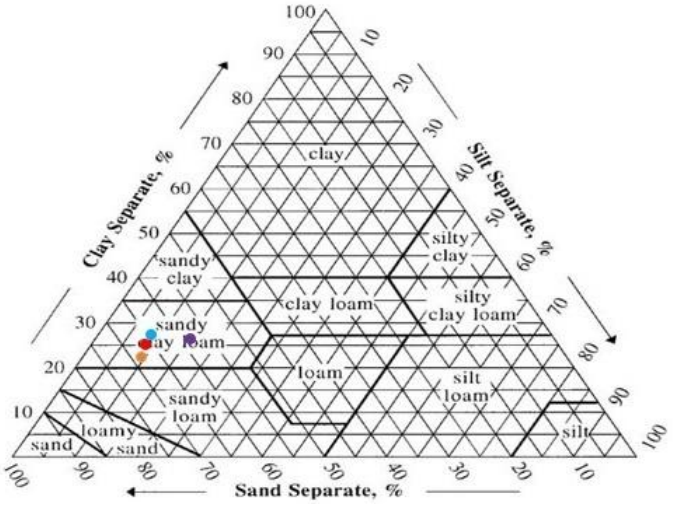

Figure 64: Soil Textural Triangle for the Sub Soil of the four Locations (Akotokyere-Red, Jukwa-Orange, Abrafo-Light blue, and Nfuom-Purple)

Potential of Hydrogen (pH) of the Soil

The fertility of soils is determined by the potential of hydrogen (pH). It is also an indicator of the availability of essential nutrients present within the soil (Landon, 2014; Thomas, 1996). Soil pH is important because it affects the availability of nutrients to plants. Table 15, reveals that the soil nutrients within the four locations on the average are optimum for plant growth. This is because, the pH range for optimum plant's growth is between 5.5 to 7.0 (Landon, 2014; Nutrition, n.d.). Most plants nutrients become available in this pH range. However, Akotokyere and Jukwa Sub Soil had pH values of 5.09 and 5.01 respectively showing a strongly acidic soil. The pH of the soil from the various locations indicate that these are available nutrients will be available for plants growth.

The differences perhaps in the PCA results (figures 43-46) might be as a result of the minuet difference in the pH of soils for the different locations. It was observed from figures 43 and 45 that there were two major clusters. Cluster I consisted of AH(A), CO(A), RV(A), RC(A), MI(A), PP(A), VA(A), and ML(A) and cluster II consisted of AB(A) and AI(A) for location Abrafo. For location Nfuom, cluster I consisted of MI(N), RC(N), AH(N), PP(N), ML(N), CO(N), RV(N), and VA(N) and cluster II consisted of AB(N) and AI(N). In figures 44 and 46 however, the AMHPs sample AI for both locations Jukwa and Akotokyere was observed to cluster with cluster I as described for locations Abrafo and Nfuom.

Table 15: pH of both the Top Soil and Sub Soil for the four Locations

Locations	pH	
	Top Soil	Sub Soil
Akotokyere	5.05	5.09
Jukwa	5.57	5.01
Abrafo	6.16	6.36
Nfuom	5.74	5.64

Primary Macronutrients of the Soil Samples

Macronutrients are those needed by plants in relatively large amounts for their proper growth. Macronutrients are divided into two groups namely primary and secondary macronutrients. Primary macronutrients (Nitrogen *N*, Phosphorus *P*, and Potassium *K*) are required in large proportions for basic plant growth and development (Banuelos & Ajwa, 1999; Kabata-Pendias, 2010; Marschner, 2012; Robb, 1983). Table 16 shows the primary macronutrients of the soil samples for the four locations. Total nitrogen (*N*) was within the recommended medium concentration as reported by Bruce and Rayment (1982), Hazelton and Murphy (2016) and Jones Jr (2001). Nitrogen (*N*) is essential to plants because it is one of the building blocks for the formation of amino acids, proteins and enzymes. It also promotes plants strength and maintains plants health. Lack of nitrogen (*N*) in plants turns their leaves light green and also slow their growth.

Table 16: Concentration (ppm) of Primary Macronutrients of the Soil Samples from Soil Locations

Location	Primary macronutrients (Concentrations (ppm))					
	nitrogen (*N*)		phosphorus (*P*)		potassium (*K*)	
	Top Soil	Sub Soil	Top Soil	Sub Soil	Top Soil	Sub Soil
Akotokyere	1451.50	782.05	10.03	4.99	116.94	64.65
Jukwa	881.93	503.70	30.29	19.04	125.65	58.30
Abrafo	1271.10	1461.50	69.95	65.65	192.00	206.20
Nfuom	1053.10	1170.50	11.68	5.08	80.90	33.16

According to Jones Jr (2001), concentration of phosphorus *P* less than 20 *ppm* is considered to be low, between 20-40 *ppm* is considered to be medium and between $40-100$ *ppm* is considered to be high. The concentration of phosphorus *P* was low in all the soil locations except Abrafo which had a concentration of 69.95 *ppm* and 65.65 *ppm* for both the Top Soil and Sub Soil. Low phosphorus (*P*) in soil results in purplish colouration to leaves and also there is stunted growth in plants. However, adequate phosphorus (*P*) in soils is an important component of photosynthesis and the development of enzymes and proteins. It also plays an important role in cell division and the creation and transport of sugars and starches. Also, according to Jones Jr (2001), a potassium (*K*) concentration within the range of $0-50$ *ppm* is considered to be low, a range of $51-100$ *ppm* is considered to be marginal and concentrations greater than 100 *ppm* is considered to be adequate. The concentration of potassium (*K*) for the top soil was adequate for Akotokyere, Jukwa, and Abrafo but was marginal for Nfuom. The concentration for potassium (*K*) for the sub soil was

adequate for Abrafo, marginal for Akotokyere and Jukwa but low for Nfuom. Inadequate potassium (*K*) in the soil results in the yellowing and death to tissue at the tips. Adequate supply of potassium (*K*) in soils is an important component of plant cells. It also influences the uptake of water by the roots and plays a role in both respiration and photosynthesis.

Secondary Macronutrients in the Soil Samples

Secondary macronutrients (Magnesium *Mg* and Calcium *Ca*) are required in moderate amounts for plant growth and development (Banuelos & Ajwa, 1999; Kabata-Pendias, 2010; Marschner, 2012; Robb, 1983). Table 17, shows the secondary macronutrients of the soil samples for the various locations.

Table 17: Concentration (ppm) of Secondary Macronutrients of the Soil Samples from Soil Locations

Locations	Secondary macronutrients (Concentrations (ppm))			
	magnesium (*Mg*)		calcium (*Ca*)	
	Top Soil	Sub Soil	Top Soil	Sub Soil
Akotokyere	228.66	191.62	665.58	345.83
Jukwa	208.93	118.49	676.30	437.06
Abrafo	89.24	115.62	5114.50	4961.60
Nfuom	211.57	96.37	4445.30	534.45

Magnesium (*Mg*) is an essential part of chlorophyll. It aids in the formation of sugars, oils, and fats. *Mg* deficiency usually appears in older leaves first. The leaf tissue between the veins turn yellow while the veins remain green. Adequate calcium (*Ca*) concentrations in the soil provides a vital component of cell wall and is involved in the metabolism and formation of the nucleus. Calcium pectate in the cell wall is responsible for the physical barrier to disease entry. Calcium (*Ca*) deficiency may result to the death of plant, and may also cause the blossoms and buds to drop prematurely. The secondary macronutrients for all the soil from all the locations were very high based on literature (Landon, 2014).

Micronutrients of the Soil Samples

Micronutrients (Iron *Fe*, Copper *Cu*, and Zinc *Zn*) are essential elements needed by plants to grow. However, they are required in small quantities (Banuelos & Ajwa, 1999; Kabata-Pendias, 2010; Marschner, 2012; Robb, 1983). For instance, *Fe* is associated with enzymes in chlorophyll formation. *Zn* helps improve root development, flowering, and fruit production whilst *Cu* is associated with protein synthesis. The absence of these micronutrients can cause deficiency syndromes in plants. For example, *Fe* deficiency are mainly manifested by yellow leaves due to low levels of chlorophyll. *Zn* is associated with delayed maturity, whilst *Cu* deficiency is associated with stunted growth, yellowing of leaves, and pale green leaves that wither easily. Table 18 shows the micronutrients obtained from the various locations for both the Top Soil and Sub Soils. The iron (*Fe*) concentrations for these locations were within the recommended range for soils (Haby & Sims, 1979; Landon, 2014). Also, the *Cu* and *Zn* concentrations were within the recommended range for soils (Haby &

Sims, 1979; Landon, 2014). All the AMHPs samples had their roots beyond the Top Soil and therefore appropriate nutrients required by the plants for their proper growth was likely to be obtained.

Table 18: Concentration (ppm) of Micronutrients of the Soil Samples from Soil Locations

Location	Micronutrient (Concentration (ppm))					
	iron (*Fe*)		copper (*Cu*)		zinc (*Zn*)	
	Top Soil	Sub Soil	Top Soil	Sub Soil	Top Soil	Sub Soil
Akotokyere	2.52	1.59	10.70	9.58	177.79	98.91
Jukwa	2.41	1.11	3.87	5.40	47.29	78.13
Abrafo	11.70	11.65	6.13	10.65	30.49	37.02
Nfuom	1.48	1.40	5.69	9.11	39.77	30.00

It was observed that the primary macronutrients and micronutrients for the soil samples for all the various locations were adequate and provided the necessary nutrients required by the AMHPs samples. However, the results for the secondary macronutrients compared with literature were very high for all, and this could have had effect on the medicinal properties of the AMHPs samples. The results obtained from the soil analysis for the various locations confirm the results obtained from both the LIF and ATR-FTIR analysis. However, more work is required in this area.

Chapter Summary

In this chapter, two spectroscopic techniques (Laser-Induced Fluorescence (LIF) and the Attenuated Total Reflectance-Fourier Transform Infrared (ATR-FTIR)) have been applied to study Anti-Malarial Herbal Plants (AMHPs) samples collected from four different locations: Abrafo, Jukwa, Nfuom and Akotokyere in Cape Coast metropolis. The results from the two techniques have been presented and discussed. Furthermore, the soil pH, soil texture analysis, the primary, secondary macro-nutrients and micro-nutrients of the soil samples from their locations have been measured and discussed.

CHAPTER FIVE

SUMMARY, CONCLUSIONS AND RECOMMENDATIONS

Overview

This chapter presents the summary of the thesis, conclusions drawn, and suggested recommendations for future work.

Summary

In summary, ten selected Anti-Malarial Herbal Plants (AMHPs) samples collected from four locations (Abrafo, Jukwa, Nfuom, and Akotokyere) in the Cape Coast metropolis has been studied using two optical spectroscopic techniques: Laser-Induced Fluorescence (LIF) and Attenuated Total Reflectance-Fourier Transform Infrared (ATR-FTIR) combined with multivariate data analysis. Soil collected from the same four locations were also studied to determine its pH, soil texture, primary and secondary macronutrients and finally its micronutrients.

Conclusions

In this work, two spectroscopic techniques were used to determine the differences/dissimilarities and to identify Anti-Malarial Herbal Plants (AMHPs) samples obtained from four locations (Abrafo, Jukwa, Nfuom, and Akotokyere) in the Cape Coast metropolis. Laser-Induced Fluorescence (LIF) and Attenuated Total Reflectance-Fourier Transform Infrared (ATR-FTIR) were the two spectroscopic techniques used. The LIF spectra for the AMHPs samples exhibited two major peak bands. Peak 1 was within the spectra range of 450 – 650 *nm* and peak 2 within the spectra range of 650 – 800 *nm*. Peak 1 was

characterised by the green (490 – 575 *nm*) and yellow (575 – 650 *nm*) fluorescence, while Peak 2 was characterised by the red to far-red (680 – 800 *nm*) fluorescence.

The LIF spectra of the AMHPs samples showed several compounds present. The compounds berberine, quercetin, flavanols, and flavins were attributed to the green fluorescence (490 – 575 *nm*). Berberine and quercetin in combination with certain compounds (pyrimethamine, chlorine) are known to be effective in malaria treatment. The other compounds that were attributed to the red fluorescence of the AMHPs samples were allophycocyanin, phycobiliproteins, anthocyanins, and azulenes. The far-red fluorescence peak could not be identified with any compounds.

Two unsupervised pattern recognition methods: Principal Component Analysis (PCA) and Hierarchical Clustering Analysis (HCA) were employed to determine the similarities/dissimilarities of the AMHPs samples based on their locations. In the PCA analysis, Vernonia amygdalina (VA) was used as a standard against which all other AMHPs samples were assessed due to its safety, efficacy, and effectiveness. In the PCA and HCA, all the AMHPs samples were observed to be similar among themselves. For locations Abrafo and Nfuom, the PCA and HCA revealed two clusters. For location Abrafo, cluster I consisted of AH(A), CO(A), RV(A), MI(A), PP(A), VA(A) and ML(A) while cluster II consisted of AB(A) and AI(A). For location Nfuom, cluster I consisted of MI(N), RC(N), AH(N), PP(N), ML(N), CO(N), RV(N), and VA(N) and cluster II consisted of AB(N) and AI(N). For location Jukwa and Akotokyere, however, cluster I, consisted respectively of PP(J), RC(J), VA(J), AH(J), MI(J), RV(J), CO(J), ML(J) and AH(Ak), RC(Ak), PP(Ak), AI(Ak), VA(Ak), ML(Ak),

CO(Ak), RV(Ak), MI(Ak). For cluster II, for both locations, it was only AB. Also, PCA was able to classify or discriminate the AMHPs samples based on their locations. LIF method was used for the identification of AMHPs from the four locations. PCA models were generated from the LIF spectra of the ten AMHPs samples from the four locations. The classification results showed that all the models used could be used to identify the AMHPs samples according to the four locations based on the LIF spectra collected. The classification results for the training sets were 100.00 % for SVM, 99.95 % for KNN, and 99.23 % for LDA. For the verification sets, SVM and KNN were 100.00 % each, while LDA was 98.23 %. Finally, for the prediction sets, the two models SVM and KNN obtained 100.00 % prediction while LDA obtained 99.38 % prediction.

The ATR-FTIR spectra for the AMHPs samples showed several chemical compositions within the spectra region 4000 – 650 cm^{-1}. Carbohydrates and proteins were characterised by the $O – H$ and $N - H$ stretching vibrations which occurred around 3200 cm^{1}, while $C – H$ stretching vibrations was as a result of lipids and carbohydrates occurring around 3000 cm^{-1}. Ester-containing compounds which is commonly found in lipid membranes and cell wall pectin had absorption peak around 1732 cm^{-1}. Several modes such as $C – H$ bending or $C – O$ or $C – C$ stretching occurred in the fingerprint region (1500 – 650 cm^{-1}). Carbohydrates in leaves, stem bark were the major constituents that contributed to the absorption bands. Similarity analysis from the ATR-FTIR spectra showed similarities irrespective of the locations, the AMHPs samples were similar with a correlation and congruence coefficient close to 1. The two spectroscopic results could be effectively be used to check the quality control of the AMHPs samples.

In the soil analysis, the pH of the soil for the various locations was optimum for plant growth (5.5 – 7.0). The textural class for the soil samples from the various locations was Sandy Clay Loam except that of Jukwa Top Soil which had a textural class of Sandy Loam. This confirms the similarity of soil nutrients found in these soils textural class. The primary macronutrients (Nitrogen (*N*), Phosphorus (*P*), and Potassium (*K*)) were adequate, and essential to the development of plant growth. Magnesium (*Mg*) and calcium (*Ca*) concentrations were very high from all the four locations. However, the micronutrients (iron (*Fe*), copper (*Cu*), zinc (*Zn*)) for the soil samples from the four locations were also adequate and within the recommended range for soils. The soil analysis for the four locations however confirmed the results obtained from the LIF and ATR-FTIR analysis.

Recommendations

It is recommended that the LIF and ATR-FTIR techniques applied to AMHPs samples to create a database in the country for quality assurance purposes. This can be extended to other medicinal plants in the country and even beyond Ghana. The Food and Drugs Authority can adopt these techniques to check for, identity, locations, adulteration of medicinal plants in the country.

REFERENCES

Abdi, H., & Williams, L. J. (2010). Principal component analysis. *Wiley interdisciplinary reviews: computational statistics, 2*(4), 433-459.

Adebayo, J., & Krettli, A. (2011). Potential antimalarials from Nigerian plants: a review. *Journal of ethnopharmacology, 133*(2), 289-302.

Al-Salhi, M., Masilamani, V., Vijmasi, T., Al-Nachawati, H., & VijayaRaghavan, A. (2011). Lung cancer detection by native fluorescence spectra of body fluids—a preliminary study. *Journal of fluorescence, 21*(2), 637-645.

Alaerts, G., Van Erps, J., Pieters, S., Dumarey, M., Van Nederkassel, A. M., Goodarzi, M., . . . Vander Heyden, Y. (2012). Similarity analyses of chromatographic fingerprints as tools for identification and quality control of green tea. *910*, 61-70.

Albani, J. R. (2007). *Principles and applications of fluorescence spectroscopy* (Vol. 8): Wiley Online Library.

Allen, S. E., Grimshaw, H. M., Parkinson, J. A., & Quarmby, C. (1974). *Chemical analysis of ecological materials*. Oxford,United Kingdom: Blackwell Scientific Publications.

Amuah, C. L. Y., Eghan, J. M., Anderson, B., Adueming, P. O.-W., & Opoku-Ansah, J. (2017). *Laser Induced Fluorescence in combination with Multivariate analysis classifies anti-malarial herbal plants.* Paper presented at the Frontiers in Optics 2017, Washington, D.C.

Anderson, B., Buah-Bassuah, P. K., & Tetteh, J. P. (2004). Using violet laser-induced chlorophyll fluorescence emission spectra for crop yield

assessment of cowpea (Vigna unguiculata (L) Walp) varieties. *Measurement Science and Technology, 15*(7), 1255.

Asase, A., Akwetey, G. A., & Achel, D. G. (2010). Ethnopharmacological use of herbal remedies for the treatment of malaria in the Dangme West District of Ghana. *Journal of ethnopharmacology, 129*(3), 367-376.

Asase, A., Hesse, D. N., & Simmonds, M. S. (2012). Uses of multiple plants prescriptions for treatment of malaria by some communities in southern Ghana. *Journal of ethnopharmacology, 144*(2), 448-452.

Asase, A., Oteng-Yeboah, A. A., Odamtten, G. T., & Simmonds, M. S. (2005). Ethnobotanical study of some Ghanaian anti-malarial plants. *Journal of ethnopharmacology, 99*(2), 273-279.

Avery, B., & Bascomb, C. (1974). Soil survey laboratory methods, Soil Survey Tech. In: Monogr.

Banuelos, G., & Ajwa, H. (1999). Trace elements in soils and plants: an overview. *Journal of Environmental Science & Health Part A, 34*(4), 951-974.

Banwell, C. N., & McCash, E. M. (1994). *Fundamentals of molecular spectroscopy* (Vol. 851): McGraw-Hill New York.

Barócsi, A., Kocsányi, L., Várkonyi, S., Richter, P., Csintalan, Z., & Szente, K. (2000). Two-wavelength, multipurpose, truly portable chlorophyll fluorometer and its application in field monitoring of phytoremediation. *Measurement Science and Technology, 11*(6), 717.

Bashkatov, A. N., Genina, E. A., & Tuchin, V. V. (2011). Optical properties of skin, subcutaneous, and muscle tissues: a review. *Journal of Innovative Optical Health Sciences, 4*(01), 9-38.

Bazracharza, A., Rana, M., Roy, B., Tiwari, A., & Tripathi, A. (2015). Optical Characterization of Medicinal Plants' Extracts Used for the Treatment of Diabetes. *Journal of herbs, spices & medicinal plants, 21*(1), 86-101.

Bernath, P. F. (2015). *Spectra of atoms and molecules*: Oxford university press.

Berrueta, L. A., Alonso-Salces, R. M., & Héberger, K. (2007). Supervised pattern recognition in food analysis. *Journal of Chromatography A, 1158*(1-2), 196-214.

Bertuccio, G., & Casiraghi, R. (2003). Study of silicon carbide for X-ray detection and spectroscopy. *IEEE Transactions on Nuclear Science, 50*(1), 175-185.

Brahmachari, U. (1944). Berberine in Malaria. A Preliminary Note. *The Indian Medical Gazette, 79*(6), 259.

Brahmkshatriya, P. P., & Brahmkshatriya, P. S. (2013). Terpenes: Chemistry, biological role, and therapeutic applications. *Natural products: phytochemistry, botany and metabolism of alkaloids, phenolics and terpenes*, 2665-2691.

Brereton, R. G. (2003). *Chemometrics: data analysis for the laboratory and chemical plant*. Chichester: John Wiley & Sons.

Bruce, R. C., & Rayment, G. (1982). *Analytical methods and interpretations used by the Agricultural Chemistry Branch for soil and land use surveys*: Queensland Department of Primary Industries.

Bruneton, J. (1995). *Pharmacognosy, phytochemistry, medicinal plants*: Lavoisier publishing.

Brydegaard, M., Haj-Hosseini, N., Wardell, K., & Andersson-Engels, S. (2011). Photobleaching-insensitive fluorescence diagnostics in skin and brain tissue. *IEEE Photonics Journal, 3*(3), 407-421.

Challand, S., & Willcox, M. (2009). A clinical trial of the traditional medicine Vernonia amygdalina in the treatment of uncomplicated malaria. *The Journal of Alternative and Complementary Medicine, 15*(11), 1231-1237.

Chalmers, J., & Griffiths, P. (2002). *Handbook of Vibrational Spectroscopy, 5 volumes set*. Chichester: Wiley.

Chen, Q., Cai, J., Wan, X., & Zhao, J. (2011). Application of linear/non-linear classification algorithms in discrimination of pork storage time using Fourier transform near infrared (FT-NIR) spectroscopy. *LWT-Food Science and Technology, 44*(10), 2053-2058.

Colthup, N. (2012). *Introduction to infrared and Raman spectroscopy*: Elsevier.

Coomans, D., Jonckheer, M., Massart, D. L., Broeckaert, I., & Blockx, P. (1978). The application of linear discriminant analysis in the diagnosis of thyroid diseases. *Analytica chimica acta, 103*(4), 409-415.

Coomans, D., & Massart, D. (1982). Alternative k-nearest neighbour rules in supervised pattern recognition: Part 2. Probabilistic classification on the basis of the kNN method modified for direct density estimation. *Analytica chimica acta, 138*, 153-165.

Coomans, D., & Massart, D. L. (1982). Alternative k-nearest neighbour rules in supervised pattern recognition: Part 1. k-Nearest neighbour

classification by using alternative voting rules. *Analytica chimica acta, 136*, 15-27.

de Oliveira Silva, F. R., Bellini, M. H., Tristão, V. R., Schor, N., Vieira, N. D., & Courrol, L. C. (2010). Intrinsic fluorescence of protoporphyrin IX from blood samples can yield information on the growth of prostate tumours. *Journal of fluorescence, 20*(6), 1159-1165.

Dean, J. R. (2010). *Extraction techniques in analytical sciences* (Vol. 34). Chichester: John Wiley & Sons.

Demtröder, W. (2013). *Laser spectroscopy: basic concepts and instrumentation*. Berlin: Springer Science & Business Media.

Dkhil, M. A., Al-Quraishy, S., Al-Shamrany, A., Alazzouni, A. S., Lubbad, M. Y., Al-Shaebi, E. M., & Taib, N. T. (2015). Protective effect of berberine chloride on Plasmodium chabaudi-induced hepatic tissue injury in mice. *Saudi journal of biological sciences, 22*(5), 551-555.

Dokosi, O. B. (1998). *Herbs of Ghana*. Accra,Ghana: Ghana Universities Press.

Edner, H., Johansson, J., Svanberg, S., Wallinder, E., Bazzani, M., Breschi, B., . . . Raimondi, V. (1992). Laser-induced fluorescence monitoring of vegetation in Tuscany. *EARSeL Advances in Remote Sensing, 1*(2), 119-130.

Gauglitz, G., Moore, D. S., & Vo-Dinh, T. (2014). *Handbook of spectroscopy*: Wiley-VCH Weinheim, Germany.

Gouveia-Neto, A. S., da Silva-Jr, E. A., Cunha, P. c. C., Oliveira-Filho, R. A., Silva, L. M., da Costa, E. B., . . . Willadino, L. G. (2011). Abiotic stress diagnosis via laser induced chlorophyll fluorescence analysis in plants for biofuel. In *Biofuel Production-Recent Developments and Prospects*: IntechOpen.

Gregorich, E. G., & Carter, M. R. (2007). *Soil sampling and methods of analysis*. Boca Raton: CRC Press.

Gustafsson, U., Somesfalean, G., Alnis, J., & Svanberg, S. (2000). Frequency-modulation spectroscopy with blue diode lasers. *Applied optics, 39*(21), 3774-3780.

Haby, V. A., & Sims, J. R. (1979). Availability of micronutrient cations in Montana soils. *Bulletin-Montana Agricultural Experiment Station (USA). no. 706.*

Hazelton, P., & Murphy, B. (2016). *Interpreting soil test results: What do all the numbers mean?* Australia: CSIRO publishing.

Hofmann, S. (2012). *Auger-and X-ray photoelectron spectroscopy in materials science: a user-oriented guide* (Vol. 49): Springer Science & Business Media.

Hotelling, H. (1933). Analysis of a complex of statistical variables into principal components. *Journal of educational psychology, 24*(6), 417.

Irvine, F. R. (1961). *Woody plants of Ghana*. Oxford,United Kingdom: Oxford University Press.

Iwu, M. M. (2014). *Handbook of African medicinal plants* (2nd ed.). Boca Raton, FL: CRC press.

Jackson, J. E. (1981). Principal components and factor analysis: part II—additional topics related to principal components. *Journal of Quality Technology*, *13*(1), 46-58.

Jacques, S. L., & Pogue, B. W. (2008). Tutorial on diffuse light transport. *Journal of Biomedical Optics*, *13*(4), 041302.

Jolliffe, I. (2011). *Principal component analysis*: Springer.

Jolliffe, I. T. (1986). Principal Component Analysis and Factor Analysis. In *Principal component analysis* (pp. 115-128). New York: Springer.

Jolliffe, I. T. (2002). Choosing a subset of principal components or variables. *Principal component analysis*, 111-149.

Jones Jr, J. B. (2001). *Laboratory guide for conducting soil tests and plant analysis*. Boca Raton: CRC press.

Kabata-Pendias, A. (2010). *Trace elements in soils and plants*. Boca Raton: CRC press.

Kalnina, I., Kurjane, N., Kirilova, E., Klimkane, L., Kirilov, G., & Zvagule, T. (2010). Correlation of altered blood albumin characteristics and lymphocyte populations to tumor stage in gastrointestinal cancer patients. *Cancer biomarkers*, *7*(2), 91-99.

Kayano, A. C. A., Lopes, S. C., Bueno, F. G., Cabral, E. C., Souza-Neiras, W. C., Yamauchi, L. M., . . . Costa, F. T. (2011). In vitro and in vivo assessment of the anti-malarial activity of Caesalpinia pluviosa. *Malaria journal*, *10*(1), 112.

Khare, C. P. (2008). *Indian medicinal plants: an illustrated dictionary*. Berlin: Springer Science & Business Media.

Komlaga, G., Agyare, C., Dickson, R. A., Mensah, M. L. K., Annan, K., Loiseau, P. M., & Champy, P. (2015). Medicinal plants and finished marketed herbal products used in the treatment of malaria in the Ashanti region, Ghana. *Journal of ethnopharmacology*, *172*, 333-346.

Lakowicz, J. R. (1992). *Topics in fluorescence spectroscopy: principles* (Vol. 2). New York: Springer Science & Business Media.

Lakowicz, J. R. (2013). *Principles of fluorescence spectroscopy*. New York: Springer Science & Business Media.

Lakowicz, J. R., & Masters, B. R. (2008). Principles of fluorescence spectroscopy. *Journal of Biomedical Optics*, *13*(2), 029901.

Landon, J. R. (2014). *Booker tropical soil manual: a handbook for soil survey and agricultural land evaluation in the tropics and subtropics*. New York: Routledge.

Lang, M., Lichtenthaler, H., Sowinska, M., Heisel, F., Miehe, J., Summ, P., & Tomasini, F. (1995). *Application of laser-induced fluorescence imaging in the detectionof plant stress.* Paper presented at the International Symposium and Exhibition on Environmental Contamination in Central and Eastern Europe 2.

Lang, M., Stober, F., & Lichtenthaler, H. K. (1991). Fluorescence emission spectra of plant leaves and plant constituents. *Radiation and Environmental Biophysics*, *30*(4), 333-347.

Lewis, I. R., & Edwards, H. (2001). *Handbook of Raman spectroscopy: from the research laboratory to the process line*. New York: CRC Press.

Lichtenthaler, H. K. (1987). Chlorophyll fluorescence signatures of leaves during the autumnal chlorophyll breakdown. *Journal of plant physiology, 131*(1-2), 101-110.

Lichtenthaler, H. K., & Buschmann, C. (1987). Chlorophyll fluorescence spectra of green bean leaves. *Journal of plant physiology, 129*(1-2), 137-147.

Lichtenthaler, H. K., Stober, F., & Lang, M. (1992). The nature of the different laser-induced fluorescence signatures of plants. *EARSeL Advances in Remote Sensing, 1*(2), 20-32.

Lin-Vien, D., Colthup, N. B., Fateley, W. G., & Grasselli, J. G. (1991). *The handbook of infrared and Raman characteristic frequencies of organic molecules*. New York: Elsevier.

Liu, X.-J., Hu, J., Li, Z.-Y., Qin, X.-M., Zhang, L.-Z., & Guo, X.-Q. (2011). Species classification and quality assessment of Chaihu (Radix Bupleuri) based on high-performance liquid chromatographic fingerprint and combined chemometrics methods. *34*(6), 961-969.

Long, D. A. (2004). Infrared and Raman characteristic group frequencies. Tables and charts George Socrates John Wiley and Sons, Ltd, Chichester, 2001. In: Wiley Online Library.

Lord, R. C. (1965). Introduction to Infrared and Raman Spectroscopy. *Journal of the American Chemical Society, 87*(5), 1155-1156.

Makkar, H. P., Siddhuraju, P., & Becker, K. (2007). *Plant secondary metabolites*. New Jersey: Humana Press.

Marschner, P. (2012). *Marschner's Mineral Nutrition of Higher Plants* (3rd ed.): Elsevier/Academic Press.

Masilamani, V., Devanesan, S., Ravikumar, M., Perinbam, K., AlSalhi, M. S., Prasad, S., . . . Alsaeed, A. H. (2014). Fluorescence spectral diagnosis of malaria–a preliminary study. *Diagnostic pathology, 9*(1), 182.

McCreery, R. L. (2005). *Raman spectroscopy for chemical analysis*. New York: John Wiley & Sons.

Meier, R. (2003). Handbook of Vibrational Spectroscopy: John Chalmers, Peter R. Griffiths (Eds.), Chichester: John Wiley & Sons Ltd.(2002), 5-volume set, cloth, US $1795.00; ISBN 0-471-98847-2. In: Elsevier.

Moody, C., & Harwood, L. (1989). *Experimental organic chemistry: principles and practice*: Blackwell Scientific, Oxford.

Movasaghi, Z., Rehman, S., & ur Rehman, D. I. (2008). Fourier transform infrared (FTIR) spectroscopy of biological tissues. *Applied Spectroscopy Reviews, 43*(2), 134-179.

Mshana, N. R. (2000). *Traditional medicine and pharmacopoeia: contribution to the revision of ethnobotanical and floristic studies in Ghana*: Organization of African Unity/Scientific, Technical & Research Commission.

Nakamoto, K. (2006). Infrared and R aman Spectra of Inorganic and Coordination Compounds. *Handbook of Vibrational Spectroscopy*.

Nguta, J., Mbaria, J., Gakuya, D., Gathumbi, P., & Kiama, S. (2010). Antimalarial herbal remedies of Msambweni, Kenya. *Journal of ethnopharmacology, 128*(2), 424-432.

Njan, A. A. (2012). Herbal medicine in the treatment of malaria: Vernonia amygdalina: an overview of evidence and pharmacology. In *Toxicity and Drug Testing*: InTech.

Nutrition, C. (n.d.). Soil pH. Retrieved from http://www.cropnutrition.com/efu-soil-ph

Oyeyemi, I. T., Akinlabi, A. A., Adewumi, A., Aleshinloye, A. O., & Oyeyemi, O. T. (2017). Vernonia amygdalina: A folkloric herb with anthelminthic properties. *Beni-Suef University Journal of Basic and Applied Sciences*.

Ozaki, Y., McClure, W. F., & Christy, A. A. (2006). *Near-infrared spectroscopy in food science and technology*. New York: John Wiley & Sons.

Pandey, A., & Tripathi, S. (2014). Concept of standardization, extraction and pre phytochemical screening strategies for herbal drug. *2*(5).

Papageorgiou, G. C., & Govindee. (2007). *Chlorophyll a fluorescence: a signature of photosynthesis* (Vol. 19): Springer Science & Business Media.

Pavia, D. L., Lampman, G. M., Kriz, G. S., & Vyvyan, J. A. (2014). *Introduction to spectroscopy*: Cengage Learning.

Pengelly, A. (2004). *The constituents of medicinal plants: an introduction to the chemistry and therapeutics of herbal medicine*: CABI Pub.

Phaladiganon, P., Kim, S. B., Chen, V. C., & Jiang, W. (2013). Principal component analysis-based control charts for multivariate nonnormal distributions. *Expert Systems with Applications, 40*(8), 3044-3054.

Platt, U., & Stutz, J. (2008). Differential absorption spectroscopy. In *Differential Optical Absorption Spectroscopy* (pp. 135-174): Springer.

Raman, C. V., & Krishnan, K. S. (1928). A new type of secondary radiation. *Nature, 121*(3048), 501.

Ramsey, E. (2012). *Analytical supercritical fluid extraction techniques*: Springer Science & Business Media.

Rios, J., & Recio, M. (2005). Medicinal plants and antimicrobial activity. *Journal of ethnopharmacology, 100*(1-2), 80-84.

Robb, D. A. (1983). *Metals and micronutrients: Uptake and utilization by plants*: Academic Press.

Roggo, Y., Chalus, P., Maurer, L., Lema-Martinez, C., Edmond, A., & Jent, N. (2007). A review of near infrared spectroscopy and chemometrics in pharmaceutical technologies. *Journal of pharmaceutical and biomedical analysis, 44*(3), 683-700.

Roshchina, V. V. (2008). Fluorescing world of plant secreting cells.

Roshchina, V. V. (2012). Vital autofluorescence: application to the study of plant living cells. *International Journal of Spectroscopy, 2012*.

Ross, I. A. (2001). *Medicinal Plants of the World Vol. 2*. New York, NY: Springer.

Ross, I. A. (2003). *Medicinal Plants of the World Vol. 1* (2nd ed.). New York, NY: Springer.

Sauer, M., Hofkens, J., & Enderlein, J. (2010). *Handbook of fluorescence spectroscopy and imaging: from ensemble to single molecules*: John Wiley & Sons.

Seppälä, J. (2009). *Fluorescence properties of Baltic Sea phytoplankton.* (Doctorial Thesis), University of Helsinki, Retrieved from https://helda.helsinki.fi/handle/10138/22270

Sheng, W. D., Jiddawi, M., Hong, X., & Abdulla, S. (1997). Treatment of chloroquine-resistant malaria using pyrimethamine in combination with berberine, tetracycline or cotrimoxazole. *East African medical journal, 74*(5), 283-284.

Shlens, J. (2014). A tutorial on principal component analysis. *arXiv preprint arXiv:1404.1100*.

Sjöholm, M., Somesfalean, G., Alnis, J., Andersson-Engels, S., & Svanberg, S. (2001). Analysis of gas dispersed in scattering media. *Optics letters, 26*(1), 16-18.

Smith, B. C. (1998). *Infrared spectral interpretation: a systematic approach*: CRC press.

Smith, B. C. (2011). *Fundamentals of Fourier transform infrared spectroscopy*: CRC press.

Socrates, G. (2001). *Infrared and Raman characteristic group frequencies: tables and charts*: John Wiley & Sons.

Somesfalean, G., Sjöholm, M., Alnis, J., af Klinteberg, C., Andersson-Engels, S., & Svanberg, S. (2002). Concentration measurement of gas embedded in scattering media by employing absorption and time-resolved laser spectroscopy. *Applied optics, 41*(18), 3538-3544.

Sozer, O., Komenda, J., Ughy, B., Domonkos, I., Laczkó-Dobos, H., Malec, P., . . . Kis, M. (2010). Involvement of carotenoids in the synthesis and assembly of protein subunits of photosynthetic reaction centers of Synechocystis sp. PCC 6803. *Plant and cell physiology, 51*(5), 823-835.

Stewart, C. N., Millwood, R. J., Halfhill, M. D., Ayalew, M., Cardoza, V., Kooshki, M., . . . McCrum, G. (2005). Laser-induced fluorescence imaging and spectroscopy of GFP transgenic plants. *Journal of fluorescence, 15*(5), 697.

Stuart, B. (2005). *Infrared spectroscopy*: Wiley Online Library.

Svanberg, S. (1990). Environmental monitoring using optical techniques. In *Applied Laser Spectroscopy* (pp. 417-434): Springer.

Svanberg, S. (2003). *Environmental monitoring using optical techniques.* Paper presented at the 12th International School on Quantum Electronics: Laser Physics and Applications.

Svanberg, S. (2012). *Atomic and molecular spectroscopy: basic aspects and practical applications* (Vol. 6): Springer Science & Business Media.

Teng, W.-C., Kiat, H. H., Suwanarusk, R., & Koh, H.-L. (2016). *Medicinal Plants and Malaria: Applications, Trends, and Prospects* (Vol. 16): CRC Press.

Thissen, U., Pepers, M., Üstün, B., Melssen, W., & Buydens, L. (2004). Comparing support vector machines to PLS for spectral regression applications. *Chemometrics and intelligent laboratory systems, 73*(2), 169-179.

Thomas, G. (1996). Soil pH and soil acidity. *Methods of Soil Analysis Part 3—Chemical Methods*(methods of soil analysis 3), 475-490.

Townes, C. H., & Schawlow, A. L. (2013). *Microwave spectroscopy*: Courier Corporation.

Tuchin, V. V., & Tuchin, V. (2007). Tissue optics: light scattering methods and instruments for medical diagnosis.

Van Grieken, R., & Markowicz, A. (2001). *Handbook of X-ray Spectrometry*: CRC press.

Vapnik, V., & Vapnik, V. (1998). Statistical learning theory Wiley. *New York*, 156-160.

Vapnik, V. N. (1999). An overview of statistical learning theory. *IEEE transactions on neural networks*, *10*(5), 988-999.

Wang, P., Li, L., Yang, H., Cheng, S., Zeng, Y., Nie, L., & Zang, H. (2012). Chromatographic fingerprinting and quantitative analysis for the quality evaluation of Xinkeshu tablet. *Journal of Pharmaceutical Analysis*, *2*(6), 422-430.

Winefordner, J. D. (1994). *Air monitoring by spectroscopic techniques* (Vol. 175): John Wiley & Sons.

Wold, S., Esbensen, K., & Geladi, P. (1987). Principal component analysis. *Chemometrics and intelligent laboratory systems*, *2*(1-3), 37-52.

Xu, C.-J., Liang, Y.-Z., Chau, F.-T., & Vander Heyden, Y. (2006). Pretreatments of chromatographic fingerprints for quality control of herbal medicines. *Journal of Chromatography A*, *1134*(1-2), 253-259.

Yang, J., Gong, W., Shi, S., Du, L., Sun, J., & Song, S.-l. (2016). Laser-induced fluorescence characteristics of vegetation by a new excitation wavelength. *Spectroscopy letters*, *49*(4), 263-267.

Yang, L.-w., Wu, D.-h., Tang, X., Peng, W., Wang, X.-r., Ma, Y., & Su, W.-w. J. J. o. C. A. (2005). Fingerprint quality control of Tianjihuang by high-performance liquid chromatography–photodiode array detection. *1070*(1-2), 35-42.

Yeap, S. K., Ho, W. Y., Beh, B. K., San Liang, W., Ky, H., Yousr, A. H. N., & Alitheen, N. B. (2010). Vernonia amygdalina, an ethnoveterinary and ethnomedical used green vegetable with multiple bio-activities. *Journal of medicinal plants research, 4*(25), 2787-2812.

Yeomans, K. A., & Golder, P. A. (1982). The Guttman-Kaiser criterion as a predictor of the number of common factors. *The Statistician*, 221-229.

Yudthavorasit, S., Wongravee, K., & Leepipatpiboon, N. (2014). Characteristic fingerprint based on gingerol derivative analysis for discrimination of ginger (Zingiber officinale) according to geographical origin using HPLC-DAD combined with chemometrics. *Food chemistry, 158*, 101-111.

Zhu, H., Wang, Y., Liang, H., Chen, Q., Zhao, P., & Tao, J. (2010). Identification of Portulaca oleracea L. from different sources using GC–MS and FT-IR spectroscopy. *Talanta, 81*(1-2), 129-135.

Zirihi, G. N., Mambu, L., Guédé-Guina, F., Bodo, B., & Grellier, P. (2005). In vitro antiplasmodial activity and cytotoxicity of 33 West African plants used for treatment of malaria. *Journal of ethnopharmacology, 98*(3), 281-285.

Zou, P., Hong, Y., & Koh, H. (2005). Chemical fingerprinting of Isatis indigotica root by RP-HPLC and hierarchical clustering analysis. *38*(3), 514-520.

APPENDICES

APPENDIX A: PLOT PROFILE OF AMHPS SAMPLE BASED ON LOCATIONS

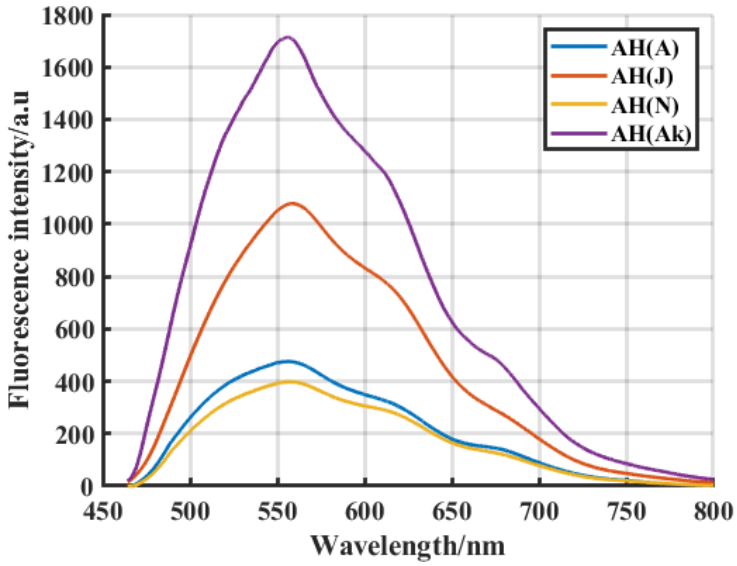

Figure 65: Average LIF Spectra for Pulverised Alstonia Boonei (AB) from four Locations: Abrafo (A), Jukwa (J), Nfuom (M), and Akotokyere (Ak)

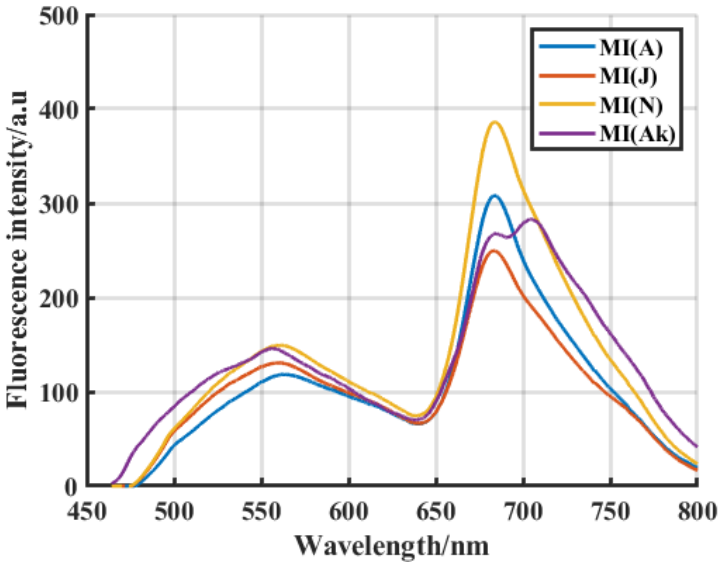

Figure 66: Average LIF Spectra for pulverised Mangifera Indica (MI) from four Locations: Abrafo (A), Jukwa (J), Nfuom (M), and Akotokyere (Ak)

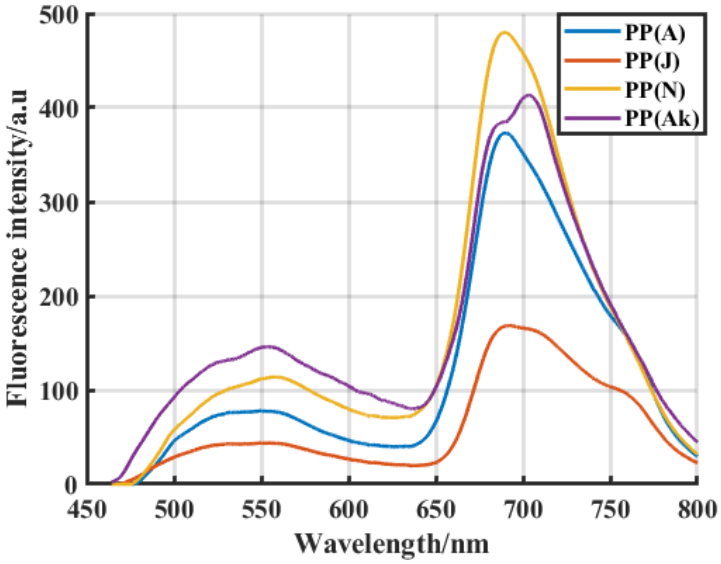

Figure 67: Average LIF Spectra for pulverised Paullinia Pinnata (PP) from four Locations: Abrafo (A), Jukwa (J), Nfuom (M), and Akotokyere (Ak)

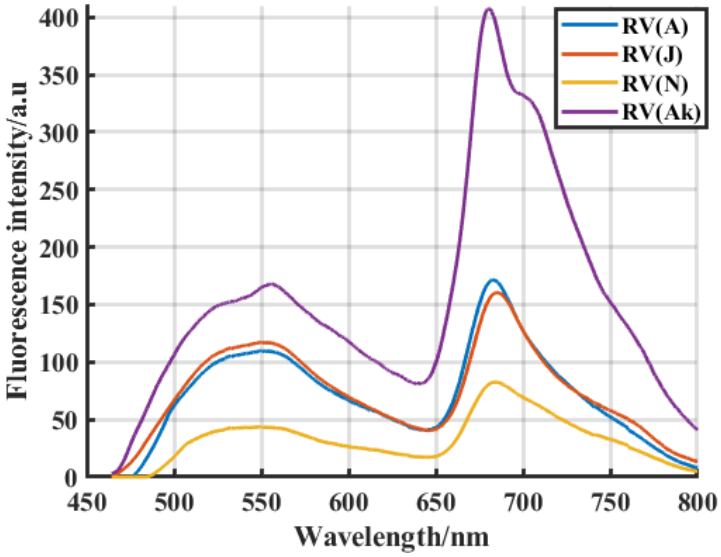

Figure 68: Average LIF Spectra for pulverised Rauvolfia Vomitoria (RV) from four Locations: Abrafo (A), Jukwa (J), Nfuom (M), and Akotokyere (Ak)

APPENDIX B: DECONVOLUTED PEAKS OF AMHPS SAMPLE BASED ON LOCATIONS

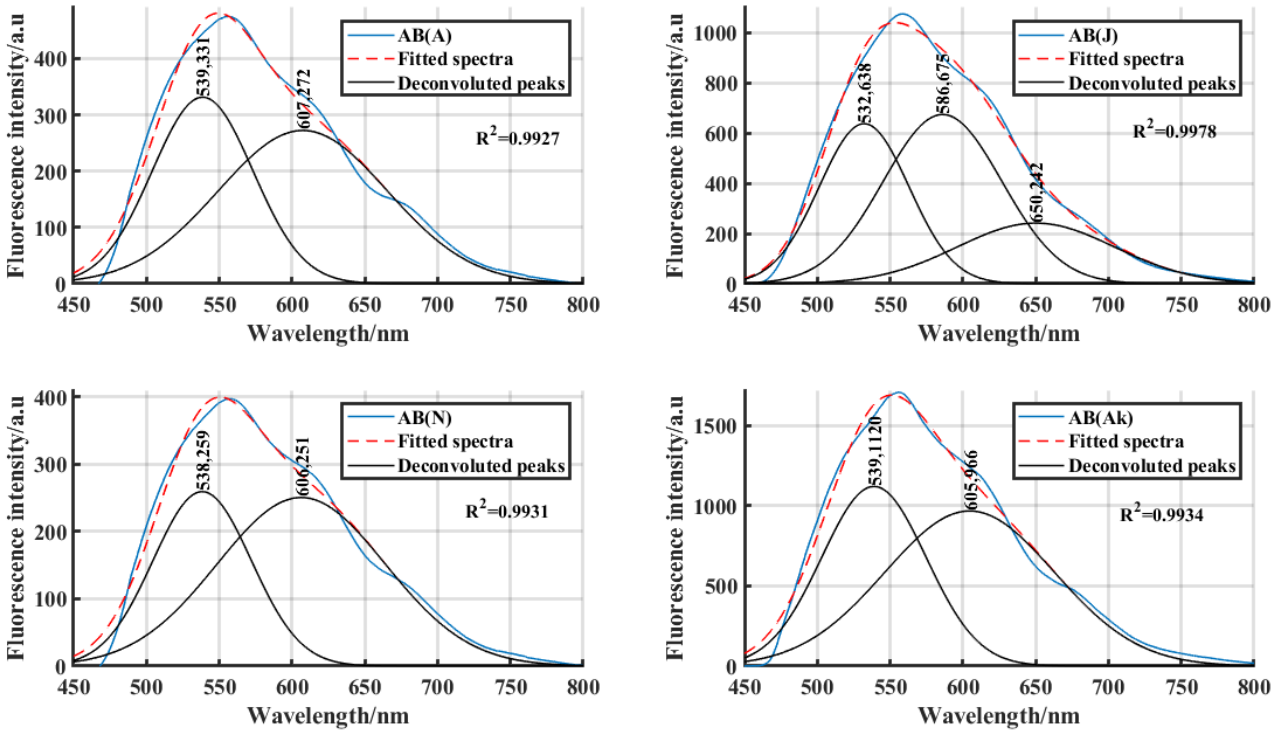

Figure 69: Deconvoluted Average LIF Spectra of pulverised form of Alstonia Boonei (AB) from (a) Abrafo (A) (b) Jukwa (J) (c) Nfuom (N) (d) Akotokyere (Ak) Excited with a 445 *nm* Diode Laser

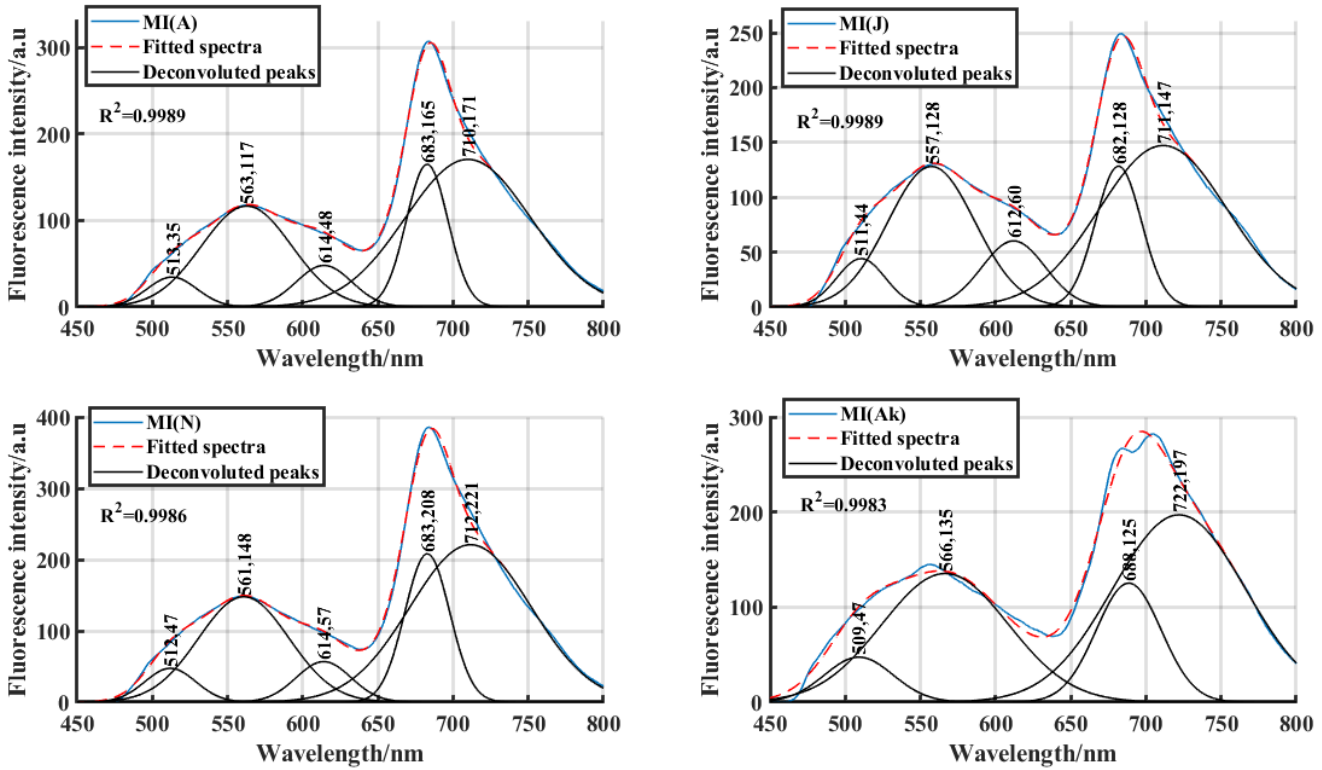

Figure 70: Deconvoluted Average LIF Spectra of Pulverised form of Mangifera Indica (MI) from (a) Abrafo (A) (b) Jukwa (J) (c) Nfuom (N) (d) Akotokyere (Ak) Excited with a $445\ nm$ Diode Laser

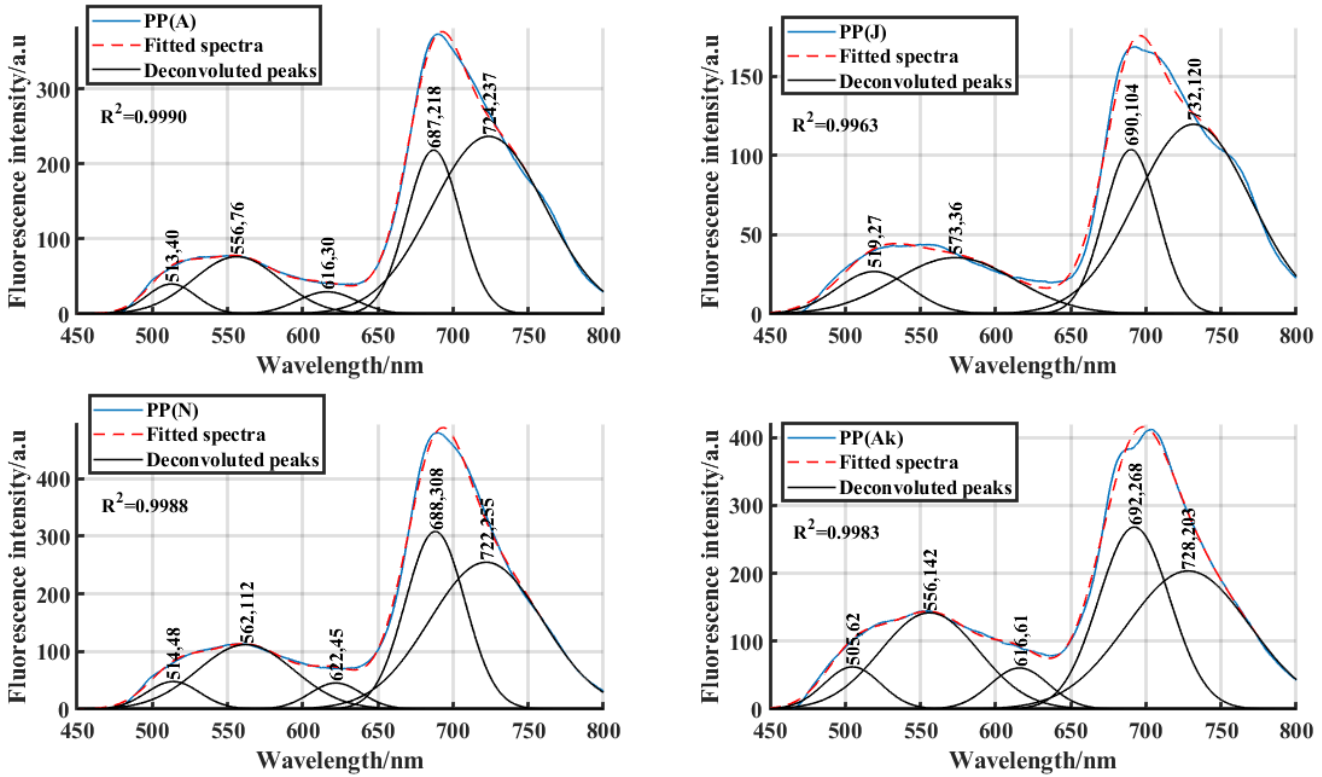

Figure 71: Deconvoluted Average LIF Spectra of Pulverised form of Paullinia Pinnata (PP) from (a) Abrafo (A) (b) Jukwa (J) (c) Nfuom (N) (d) Akotokyere (Ak) Excited with a $445\ nm$ Diode Laser

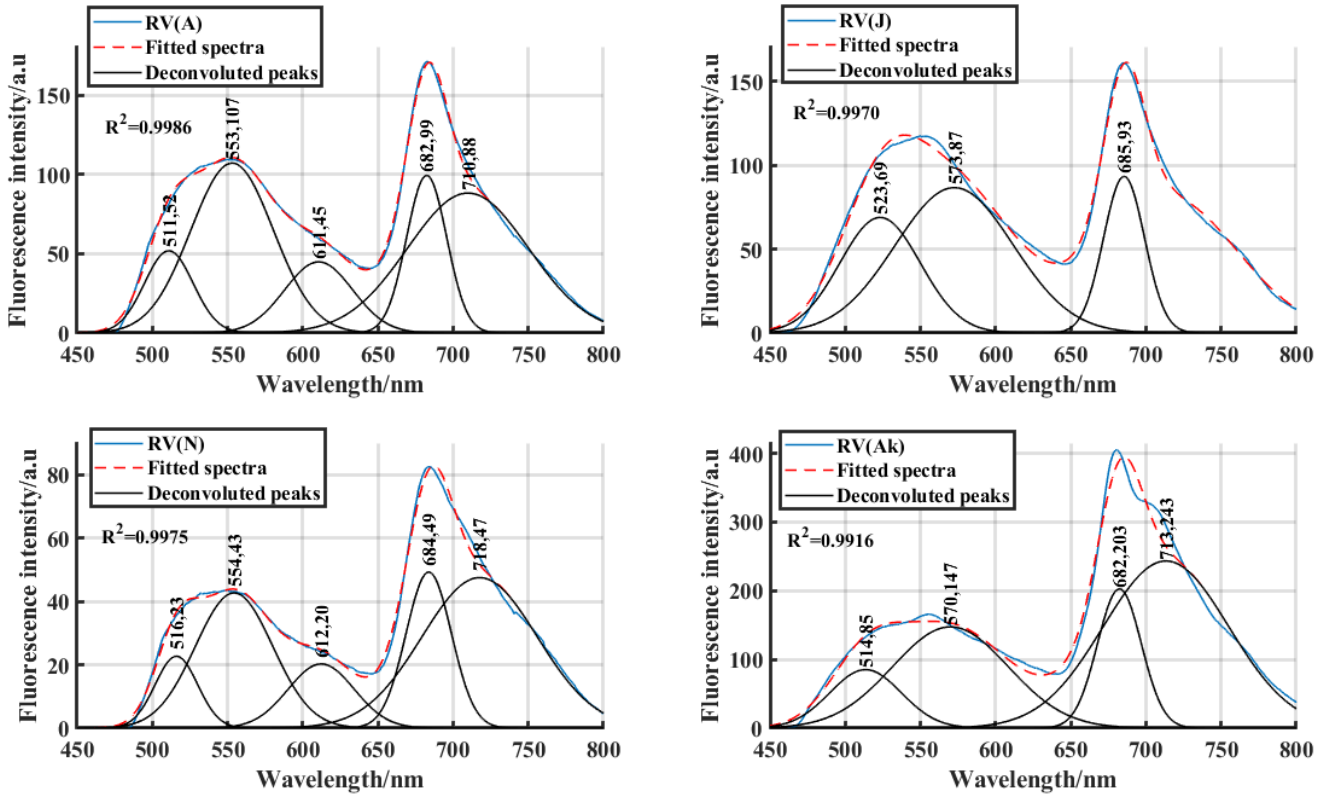

Figure 72: Deconvoluted Average LIF Spectra of Pulverised form of Rauvolfia Vomitoria (RV) from (a) Abrafo (A) (b) Jukwa (J) (c) Nfuom (N) (d) Akotokyere (Ak) Excited with a $445\ nm$ Diode Laser

APPENDIX C: SCORE PLOTS OF AMHPS SAMPLE

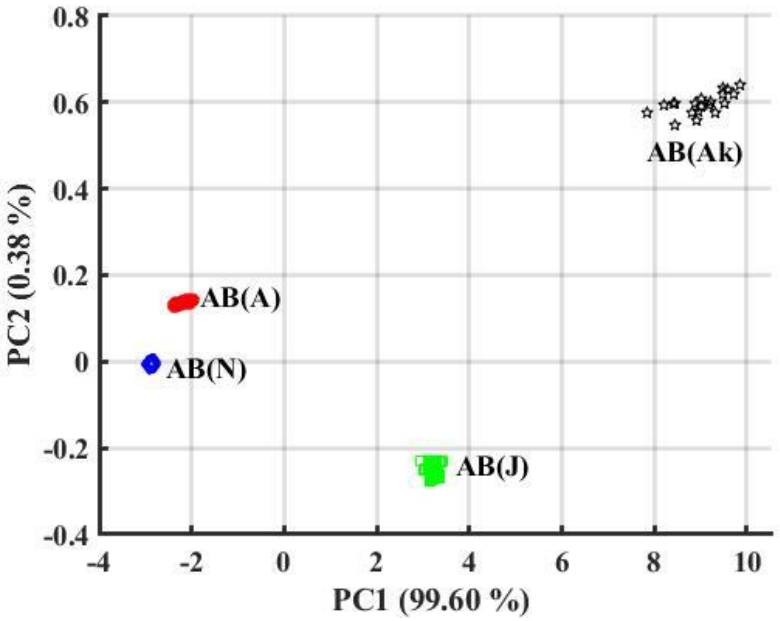

Figure 73: Score plot of AB from the four Locations

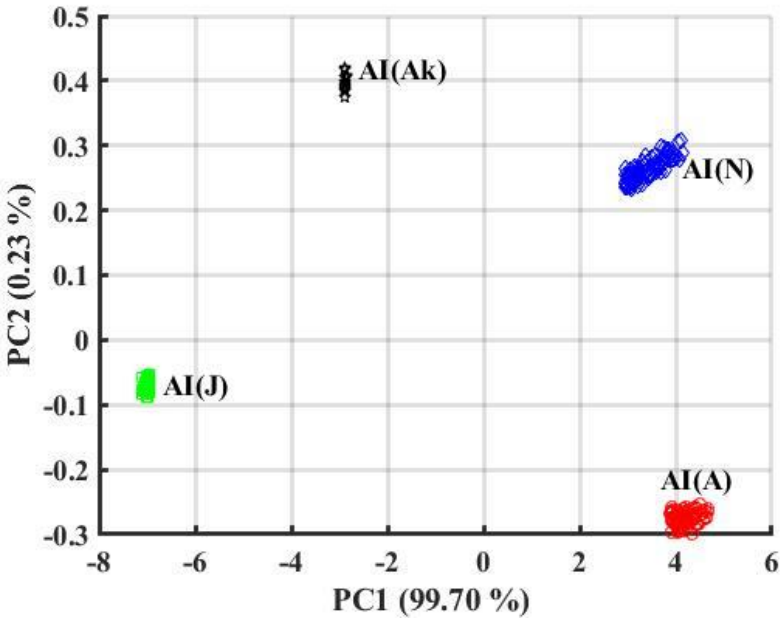

Figure 74: Score plot of AI from the four Locations

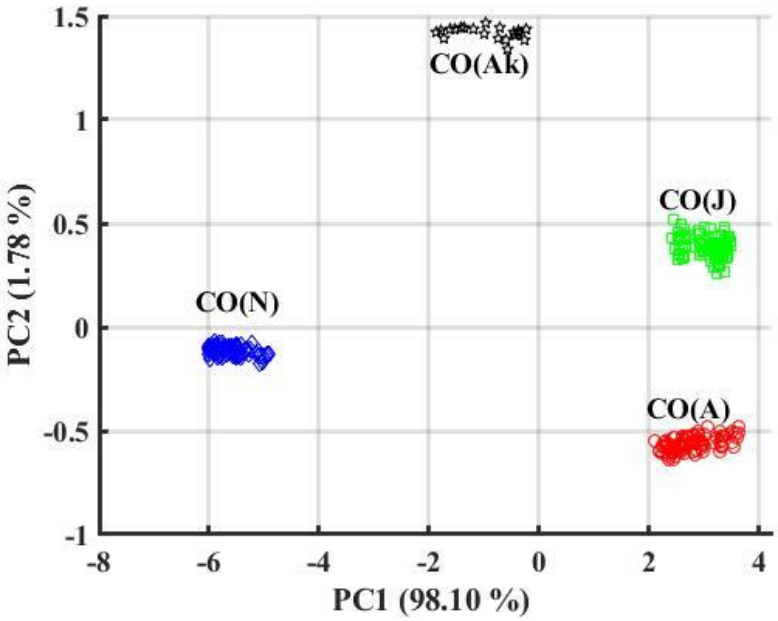

Figure 75: Score plot of CO from the four Locations

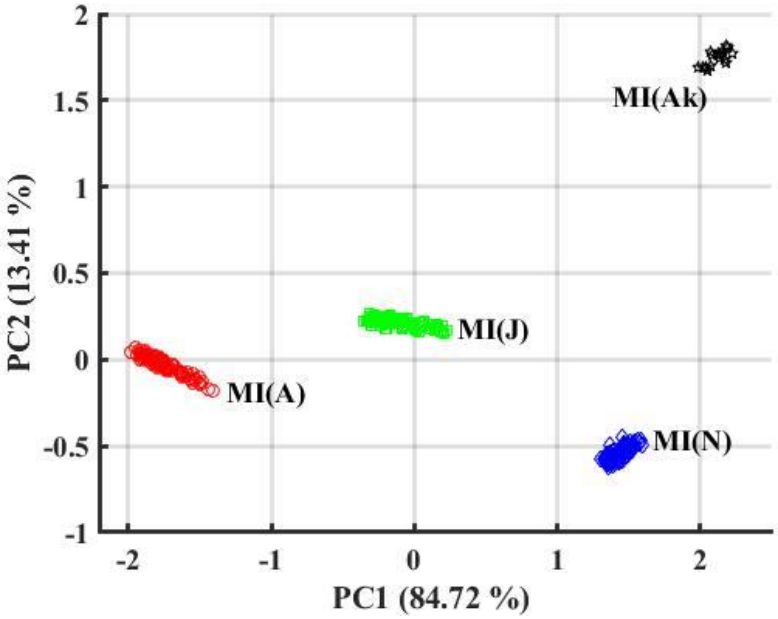

Figure 76: Score plot of MI from the four locations

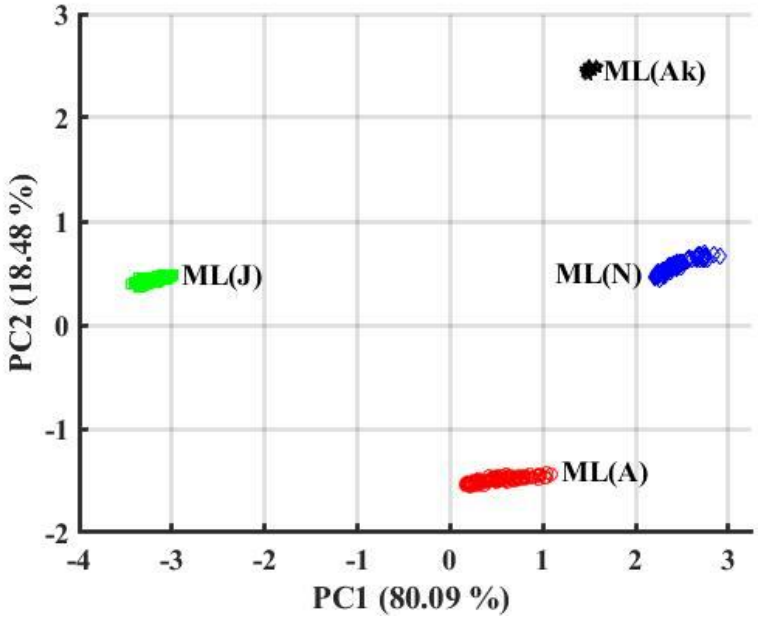

Figure 77: Score plot of ML from the four Locations

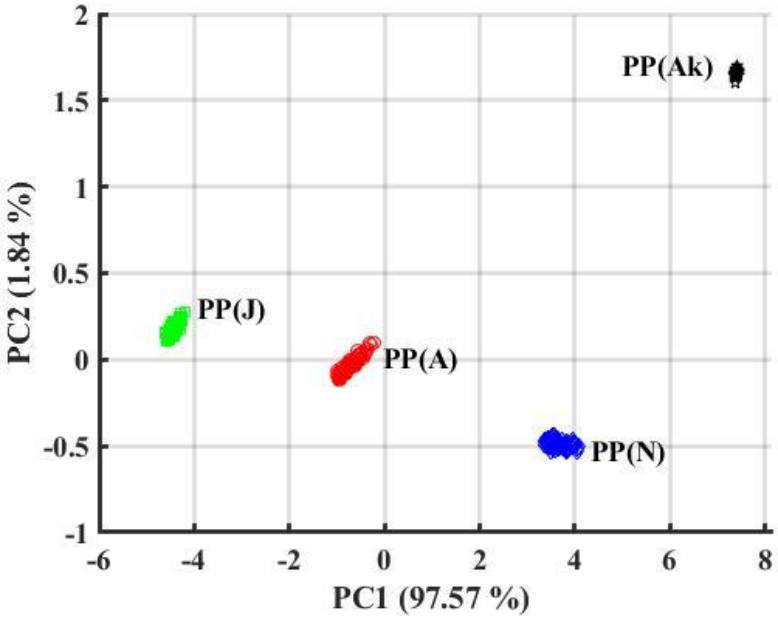

Figure 78: Score plot of PP from the four Locations

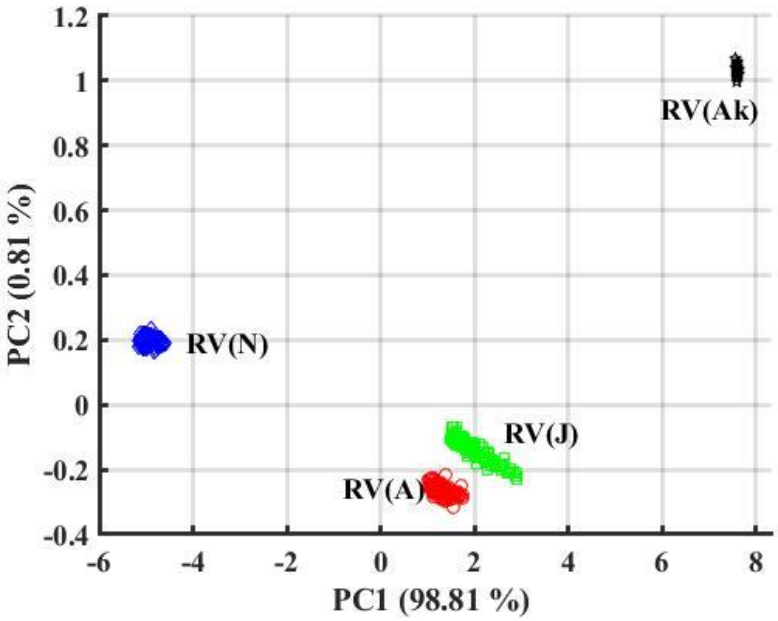

Figure 79: Score plot of RV from the four Locations

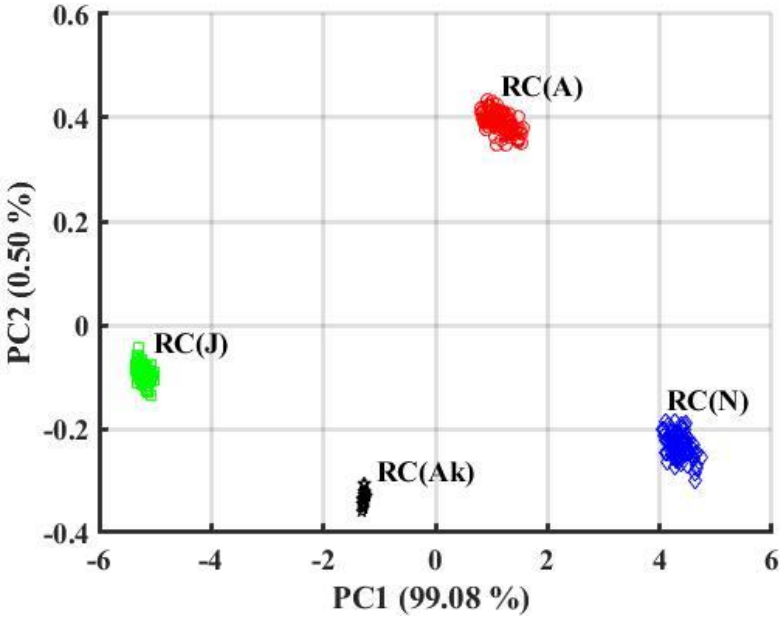

Figure 80: Score plot of RC from the four Locations

APPENDIX D: LOADING PLOTS OF AMHPS SAMPLE

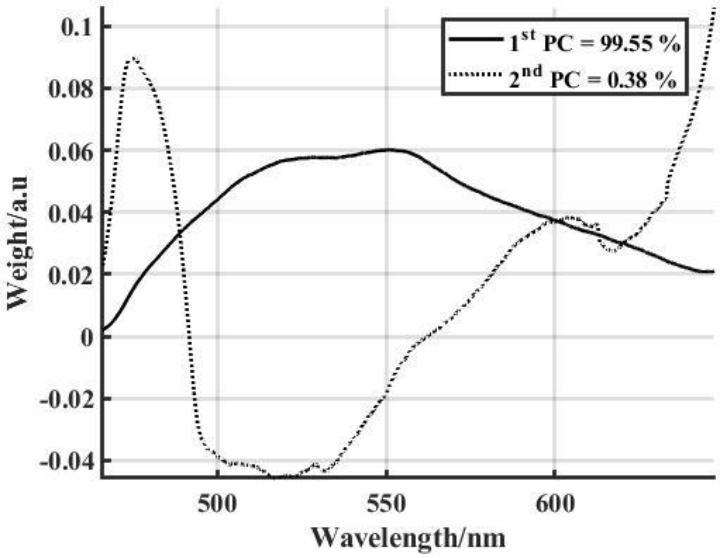

Figure 81: Loadings plot for the first two PCs obtained from the PCA of the LIF Spectra of AH from the four Locations

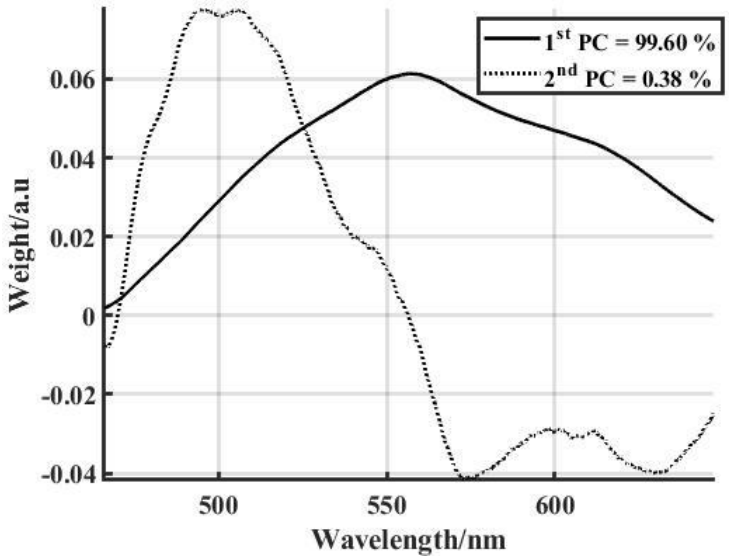

Figure 82: Loadings plot for the first two PCs obtained from the PCA of the LIF Spectra of AB from the four Locations

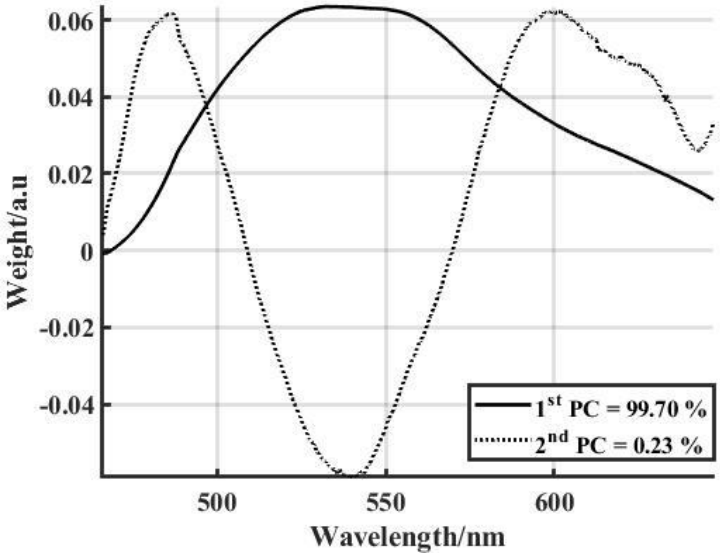

Figure 83: Loadings plot for the first two PCs obtained from the PCA of the LIF Spectra of AI from the four Locations

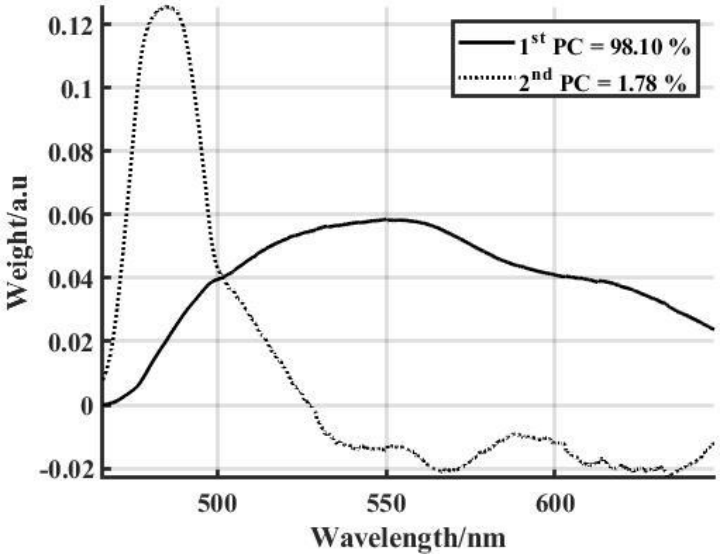

Figure 84: Loadings plot for the first two PCs obtained from the PCA of the LIF Spectra of CO from the four Locations

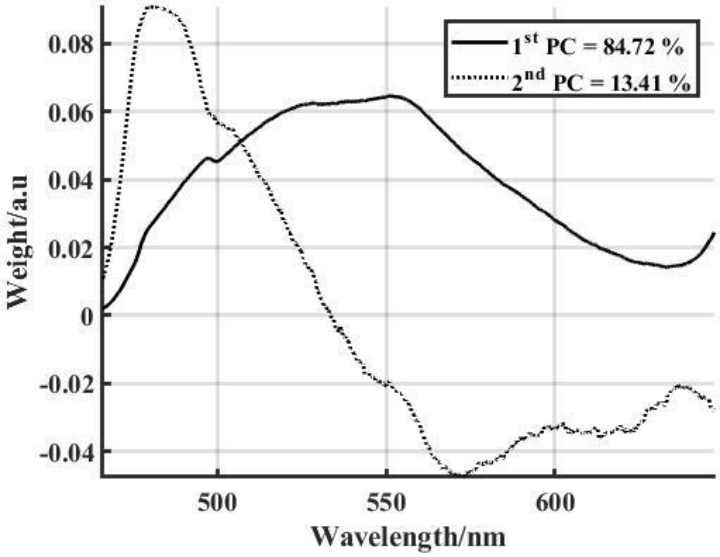

Figure 85: Loadings plot for the first two PCs obtained from the PCA of the LIF Spectra of MI from the four Locations

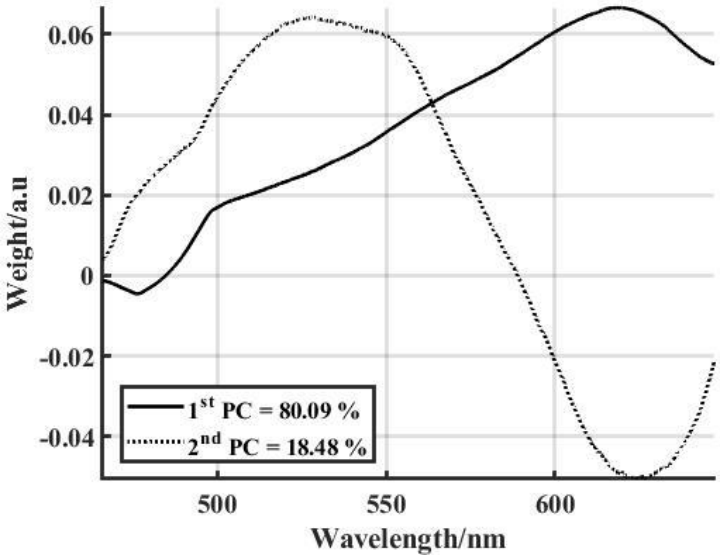

Figure 86: Loadings plot for the first two PCs obtained from the PCA of the LIF Spectra of ML from the four Locations

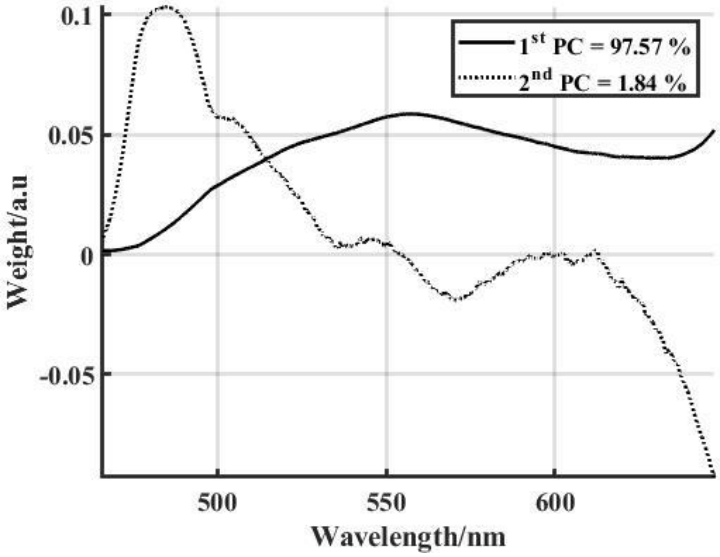

Figure 87: Loadings plot for the first two PCs obtained from the PCA of the LIF Spectra of PP from the four Locations

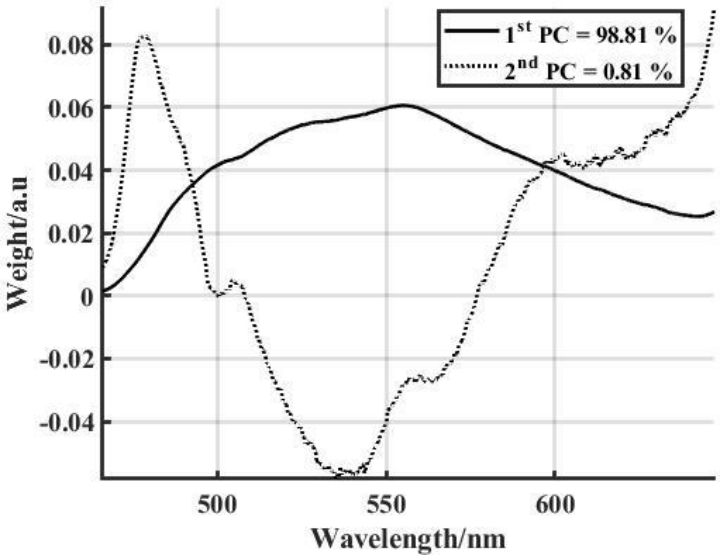

Figure 88: Loadings plot for the first two PCs obtained from the PCA of the LIF Spectra of RV from the four Locations

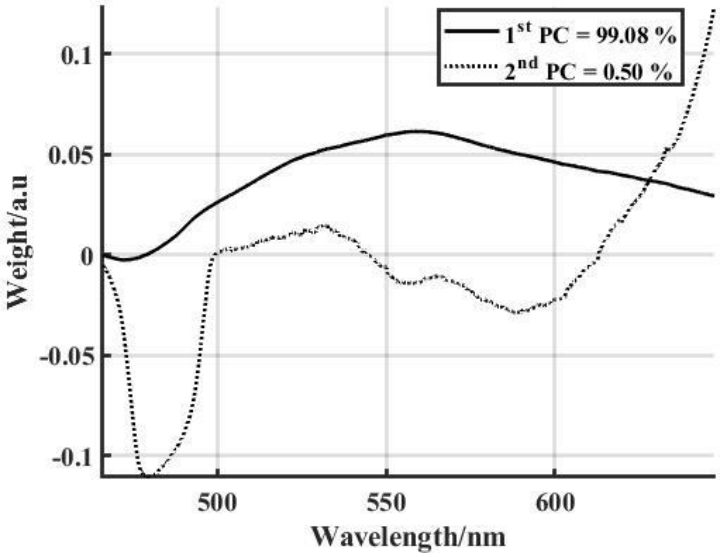

Figure 89: Loadings plot for the first two PCs obtained from the PCA of the LIF Spectra of RC from the four Locations

APPENDIX E: EIGENVALUE PLOTS OF AMHPS SAMPLE

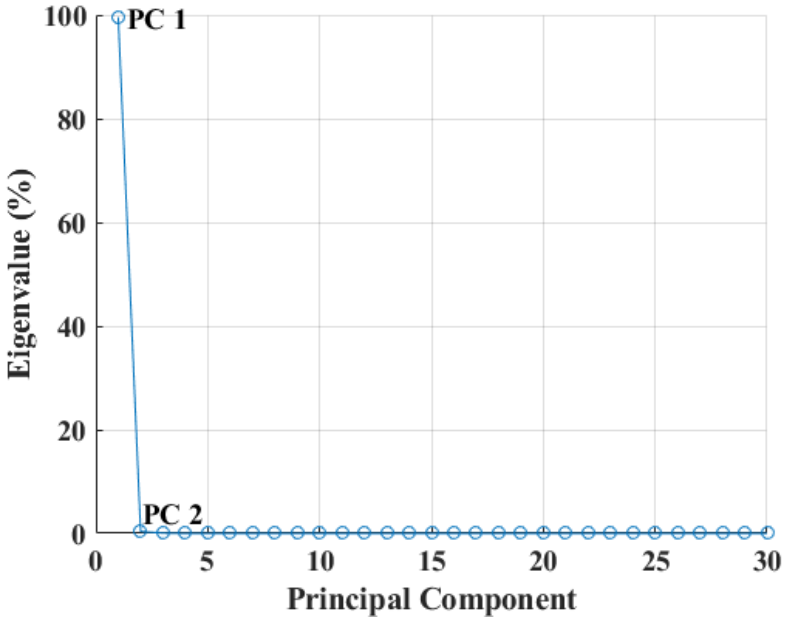

Figure 90: Eigenvalues (%) of the PCs which represent the Percentage Weight of each Principal Component for Acanthospermum Hispidum

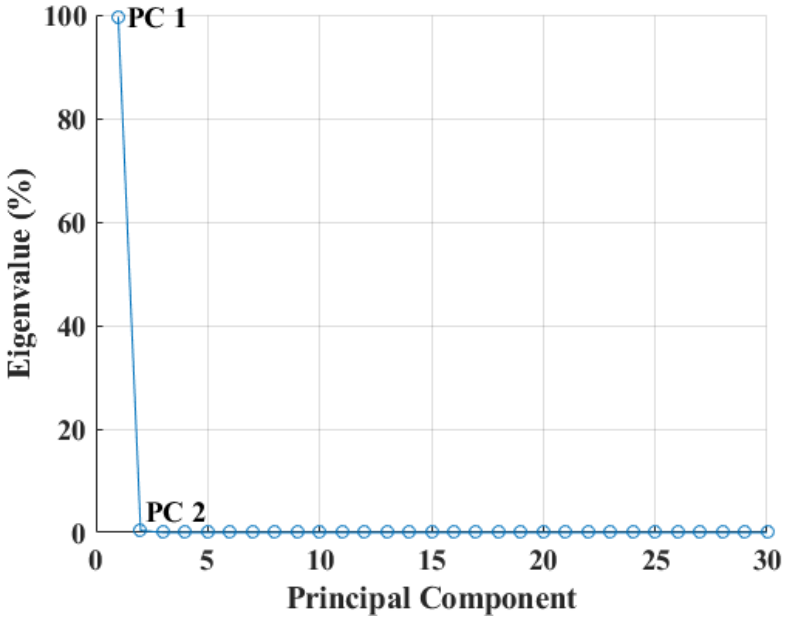

Figure 91: Eigenvalues (%) of the PCs which represent the Percentage Weight of each Principal Component Alstonia Boonei

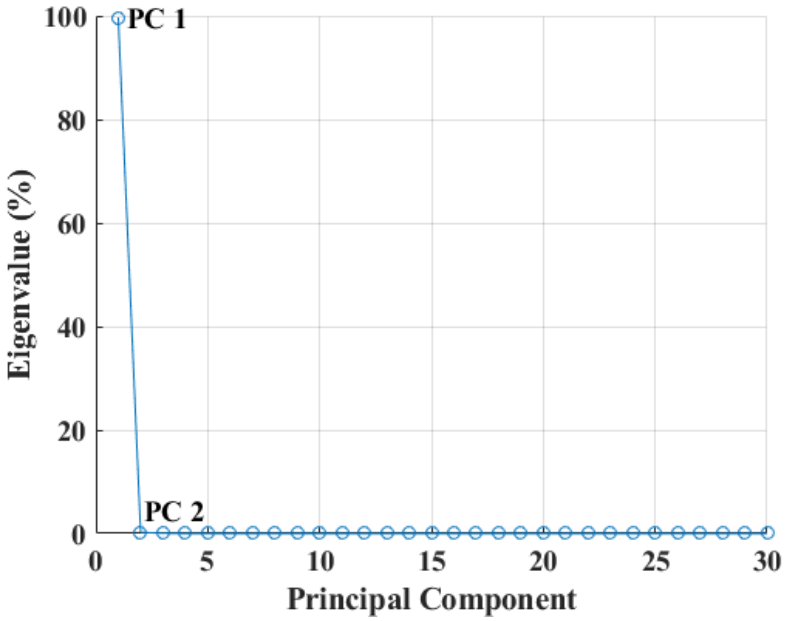

Figure 92: Eigenvalues (%) of the PCs which represent the Percentage Weight of each Principal Component Cassia Occidentalis

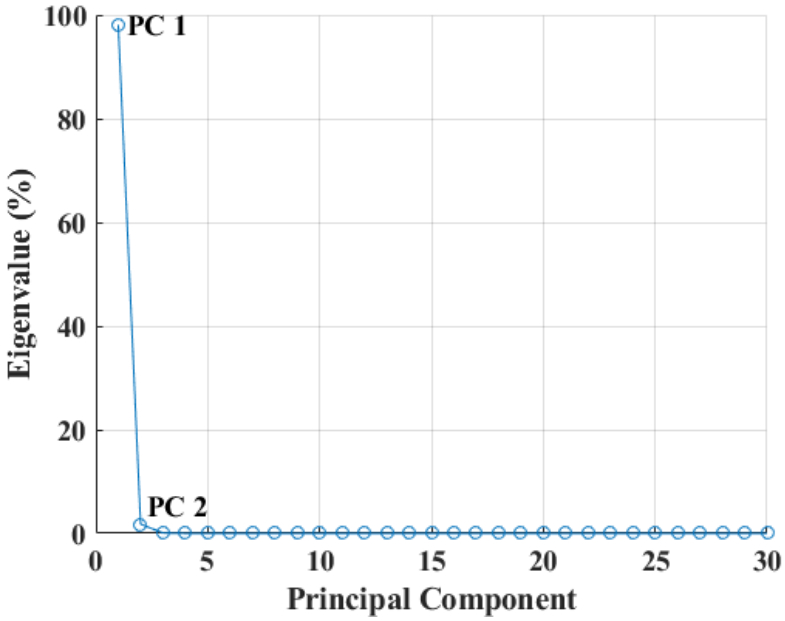

Figure 93: Eigenvalues (%) of the PCs which represent the Percentage Weight of each Principal Component Azadirachta Indica

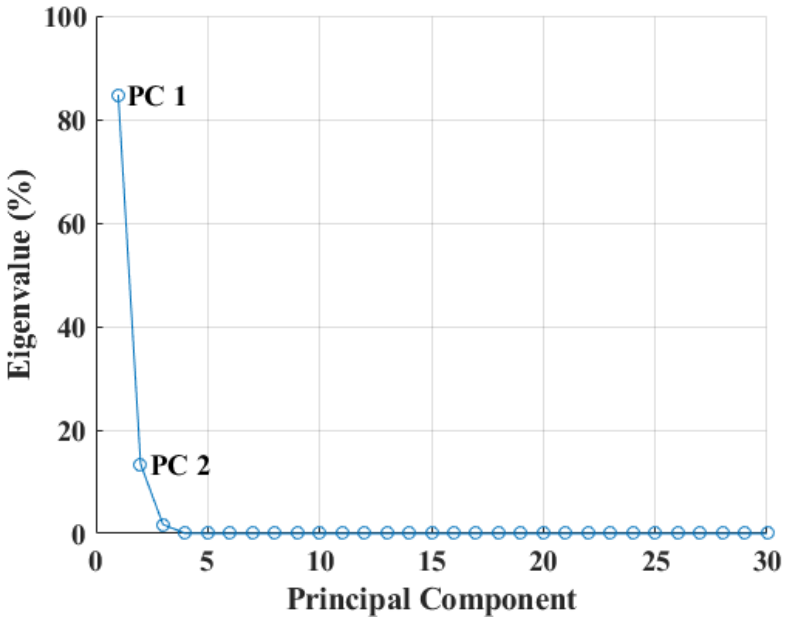

Figure 94: Eigenvalues (%) of the PCs which represent the Percentage Weight of each Principal Component Mangifera Indica

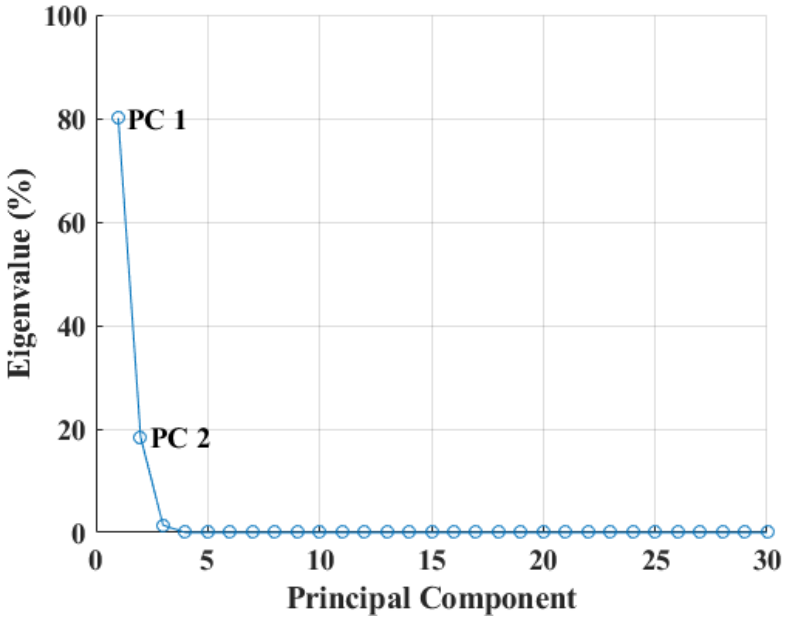

Figure 95: Eigenvalues (%) of the PCs which represent the Percentage Weight of each Principal Component Morinda Lucida

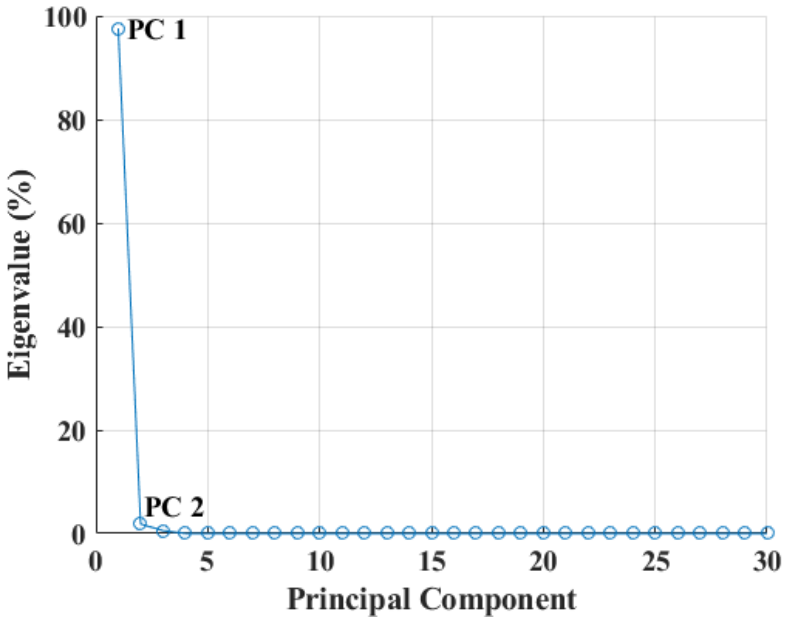

Figure 96: Eigenvalues (%) of the PCs which represent the Percentage Weight of each Principal Component Paullinia Pinnata

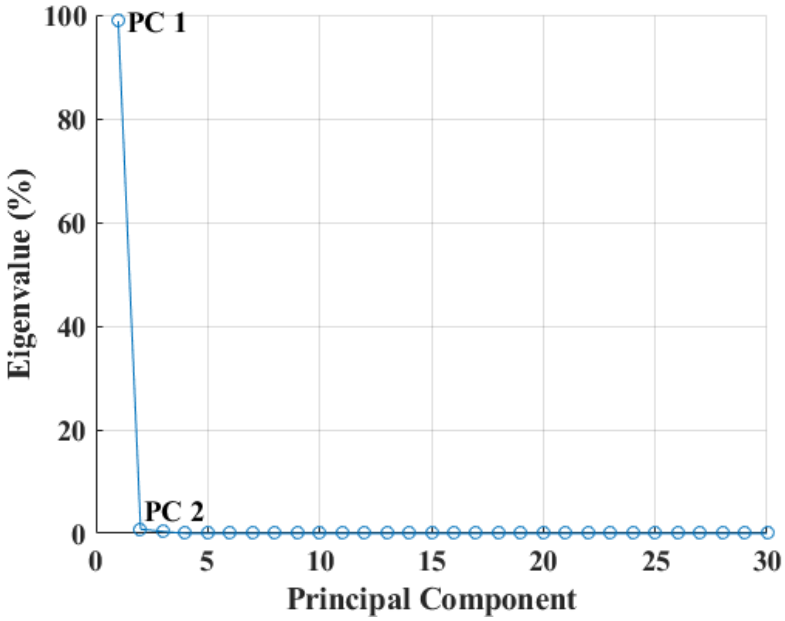

Figure 97: Eigenvalues (%) of the PCs which represent the Percentage Weight of each Principal Component Ricinus Communis

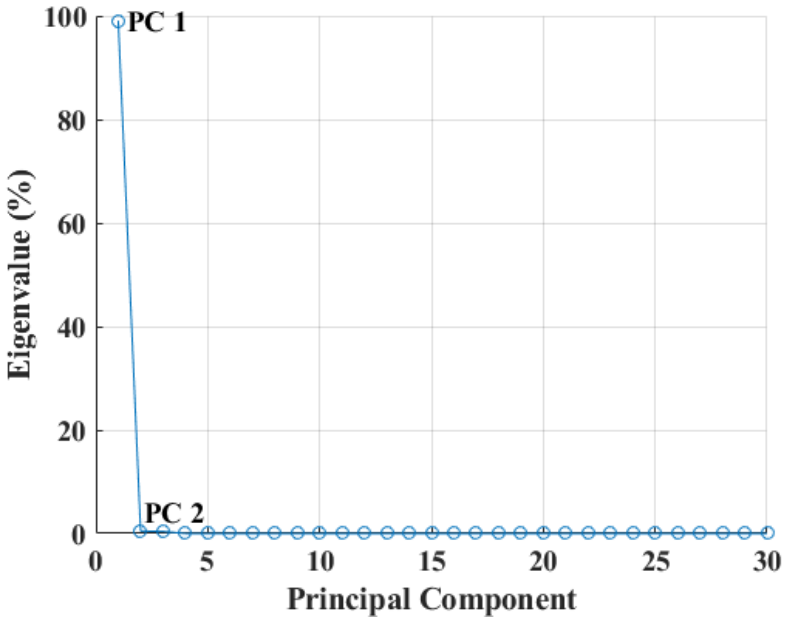

Figure 98: Eigenvalues (%) of the PCs which represent the Percentage Weight of each Principal Component Rauvolfia Vomitoria

APPENDIX F: ATR-FTIR PLOTS OF AMHPS SAMPLE

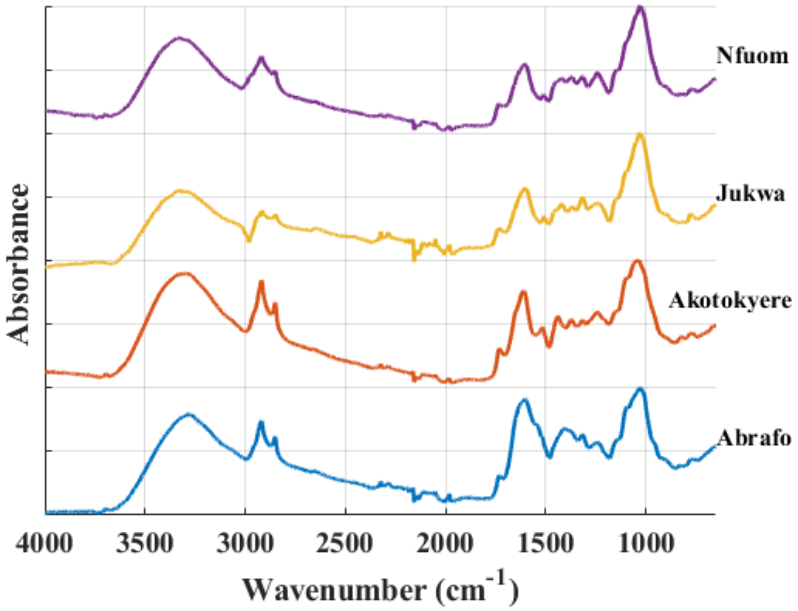

Figure 99: ATR-FTIR Spectra of Alstonia Boonei from the four Locations

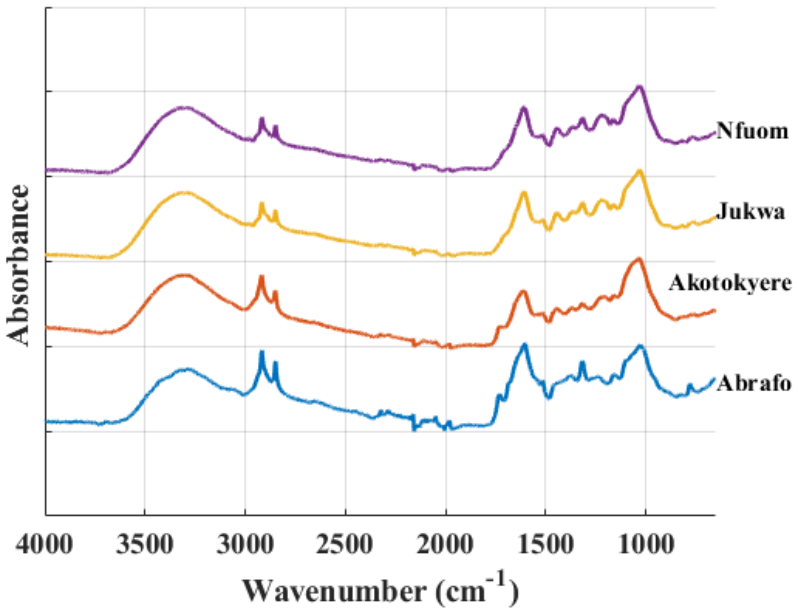

Figure 100: ATR-FTIR Spectra of Mangifera Indica from the four Locations

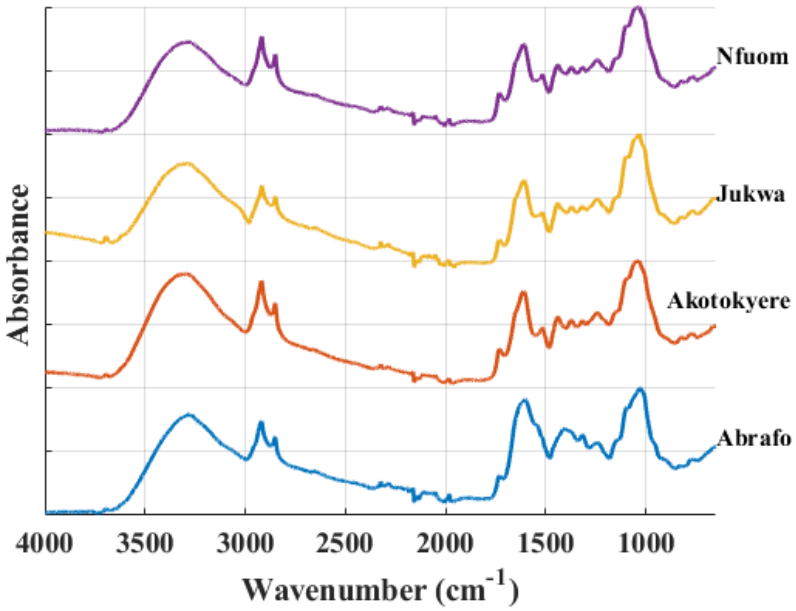

Figure 101: ATR-FTIR Spectra of Paullinia Pinnata from the four Locations

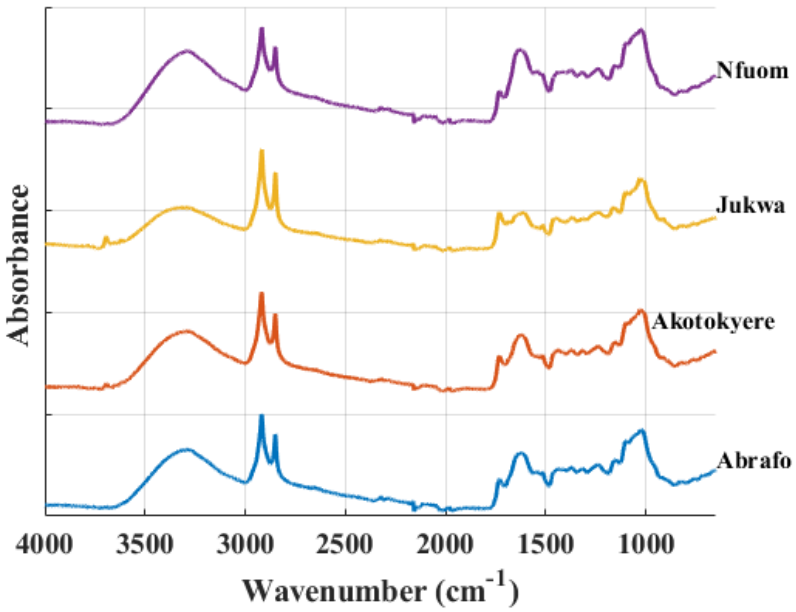

Figure 102: ATR-FTIR Spectra of Rauvolfia Vomitoria from the four Locations

PUBLICATION

Amuah, C. L. Y., Eghan, J. M., Anderson, B., Adueming, P. O. W., & Opoku-Ansah, J. (2017, September). Laser Induced Fluorescence in combination with Multivariate analysis classifies anti-malarial herbal plants. In *Frontiers in Optics* (pp. JTu2A-71). Optical Society of America.